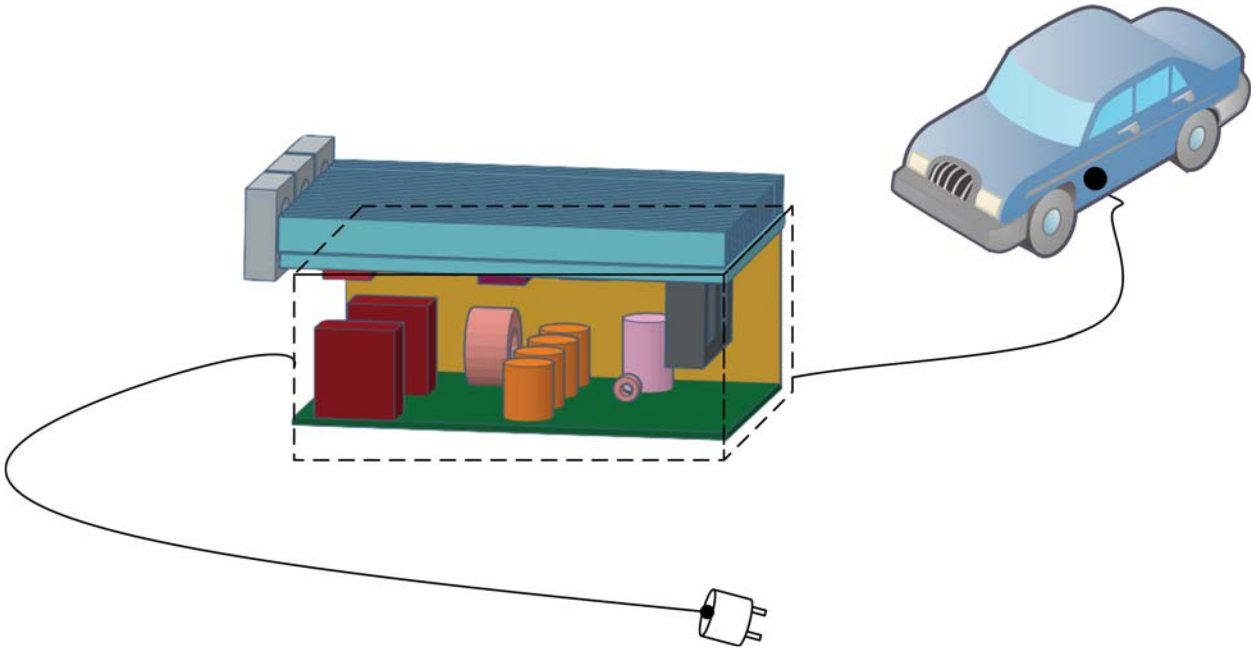

Compact AC/DC-module for Electric Vehicle Charging

Dissemble, Evaluation and Design Development of a Portable Battery Charger

Master's Thesis in Electric Power Engineering

MARTIN ALERMAN
THERESE STENBERG

Department of Electrical Engineering
CHALMERS UNIVERSITY OF TECHNOLOGY
Gothenburg, Sweden 2018

Master's thesis 2018

Compact AC/DC-module for Electric Vehicle Charging

Dissemble, Evaluation and Design Development of a Portable Battery Charger

MARTIN ALERMAN
THERESE STENBERG

Department of Electrical Engineering
Division of Electric Power Engineering
Chalmers University of Technology
Gothenburg, Sweden 2018

Compact AC/DC-module for Electric Vehicle Charging
Dissemble, Evaluation and Design Development of a Portable Battery Charger
MARTIN ALERMAN
THERESE STENBERG

Supervisor: Erik Ahlqvist, at CEVT
Examiner: Prof. Yujing Liu, at the department of Electrical Engineering

Master's Thesis 2018
Department of Electrical Engineering
Division of Electric Power Engineering
Chalmers University of Technology
SE-412 96 Gothenburg
Telephone +46 31 772 1000

Cover: The proposed off-board charger for electric vehicles, created in Tinkercad and Visio.

Typeset in LaTeX
Printed by Chalmers Reproservice
Gothenburg, Sweden 2018

Compact AC/DC for Electric Vehicle Charging
MARTIN ALERMAN
THERESE STENBERG
Department of Electrical Engineering
Division of Electric Power Engineering
Chalmers University of Technology

Abstract

At present, the automotive industry has equipped their electric vehicles with the on-board charger, where it converts the power in order to charge the high voltage battery. However, there is a demand to remove the on-board charger from the vehicle since it requires large space and weight. Therefore it is desirable to investigate if it is feasible to relocate and redesign the on-board charger to an external portable charger. Since this charger is suppose to be portable, it is essential that the design is lightweight and compact.

This research completed an analysis of a dissembled on-board charger, topologies review of converters, components selection, loss calculations, electric circuits simulation and thermal simulation studies.

In this study it was demonstrated that it was feasible to design an off-board charger for electric vehicles. The charger was design for a current level of 4 A, which has a size of 1024 cm^3, a weight of 2.8 kg and an efficiency of 94.42 %. Comparing only the module itself with the OBC, there was a weight reduction of 71 %. Forced cooling has been implemented, to prevent overheating of the power electronic components.

Keywords: On-board charger, Off-board charger, AC/DC converter, DC/DC converter, PHEV, Boost, Totem-pole, Full-bridge, Half-bridge and Cooling system.

Acknowledgements

First of all, thanks to you who found and will read this master thesis. A special thanks to our examiner Prof. Yujing Liu at Chalmers University of Technology for all his help and suggestions. We would also like to thank Erik Ahlqvist, including the entire power conversion team at CEVT for their guidance and support during this project. Thanks to the people at the Electric Power Engineering division at Chalmers for their technical support. With special thanks to Daniel Pehrman for his contribution to the dissembling process and consultation. Also thanks to Alessandro Acquaviva for his guidance through the initiation phase of this project. Last but not least, we are thankful for the endless support from our families and friends during this time.

Martin Alerman and Therese Stenberg, Gothenburg, June, 2018

Abbreviations

CAN	Controller area network
CCS	Combined charging system
CEVT	China Euro Vehicle Technology
CCM	Continuous conduction mode
CM	Common mode
CP	Control pilot
CrM	Critical conduction mode
DSP	Digital signal processor
DCM	Discontinuous conduction mode
EV	Electric vehicle
EVI	Electric vehicle inlet
EMI	Electromagnetic interference
ESR	Equivalent series resistance
GaN	Gallium nitrate
G2V	Grid-to-vehicle
HV	High voltage
IEC	International electrotechnical commission
IGBT	Insulated gate bipolar transistor
IP	International protection marking
LV	Low voltage
MOSFET	Metal oxide semiconductor field effect transistor
MCU	Microcontroller unit
OBC	On-board charger
PCB	Printed circuit board
PHEV	Plug-in hybrid electric vehicle
PFC	Power factor correction
PP	Proximity pilot
PWM	Pulse width modulation
SiC	Silicon carbide
TIM	Thermal interface material
THD	Total harmonic distortion
ZVS	Zero voltage switching
V2G	Vehicle-to-grid
VDDM	Vehicle dynamics domain master

Contents

List of Figures

List of Tables

1
Introduction

1.1 Background

With the automotive industry moving towards electrification, the number of electric vehicles (EVs) has increased in the market in recent years [1]. Therefore, it is vital to have a sufficient and accessible charging infrastructure in the society for EVs, in order to recharge the batteries in the vehicle and mitigate the driver's range anxiety. Simultaneously, the batteries have become larger to extend distance range further, which has led to an increase in weight of the vehicle [2].

A feasible solution for this could be to relocate the on-board charger (OBC) from the vehicle to a charging cable to reduce weight in the vehicle, and to provide customers with an applicable charging alternative. This cable is for household applications, where utility power is being used, which allows the driver to bring the charger with them to charge at other locations equipped with standard wall sockets.

The Propulsion unit at CEVT (China Euro Vehicle Technology) is responsible for the development of future energy transmissions for Geely Group as well as the development of electric propulsion systems including all high voltage components. At this unit, the power conversion department is interested in investigating and finding a portable off-board charger solution for plug-in hybrid electric vehicles (PHEVs) directed toward households.

The assignment is to redesign the existing on-board charger and relocate it in the charging cable as an off-board charger. Simultaneously, the AC/DC-module should be designed to be more compact by reducing size and number of the power electronic components and also adding a minimized cooling system. The AC/DC-module in the OBC includes an AC/DC-converter and DC/DC-converter. The aim of this project is to make design improvements regarding efficiency, losses, size, and weight.

One issue with having an OBC-system inside the vehicle is that it requires a lot of space, which can be used for other things, i.e. control system, larger battery or cooling system. By having more space for a larger battery, it would lead to less stress on the battery's system and longer travel distance range.

1.2 Aim

The aim of this project is to develop a compact mechanical design of an AC/DC-converter module, including thermal and electrical sizing, for an off-board charging cable for PHEVs. The device choice shall be based on various factors such as efficiency, volume, and losses.

1.3 Objectives

In order to design a compact AC/DC-module charger, the following main objectives will be investigated:

- A literature study of different topologies will be examined to find one that applies for this project.

- The electrical performance of the converter shall be taken into consideration. The power electronic components are selected to achieve high power factor (PF), high efficiency, and low THD (total harmonic distortion). These performance parameters are obtained by the simulation software LTspice and calculations procedure.

- Within the thermal aspect, the selected components will be hand calculated regarding the losses in order to evaluate if it is feasible to design an off-board charger for low-power charging application. Furthermore, a cooling system is suggested to reduce the thermal losses and will be simulated in an application software for thermal analysis.

- The components and cooling system selection will decide the final size of the off-board charger, regarding weight and volume that will be estimated.

- An investigation regarding the safety and sustainability aspects of charger module for PHEVs will be conducted.

1.4 Problem

The purpose of investigating an off-board charger for PHEVs, with design modifications regarding efficiency and size, is to create more compartment capacity within the PHEV that can be utilized for larger batteries in the first place.

In order to design an effective and compact converter for the off-board charger, diverse topologies of power electronic circuits will be analyzed. These topologies are created to find an appropriate circuit that can be used for external portable charging. By studying these topologies, a comparison in requirements can be made in regard to the type of converter, efficiency, level of power application and low number of power electronic components (capacitors and inductors). These requirements also include how the cooling implementation for the converter will be executed, where it is expected to be large in size, since liquid cooling from the vehicle is not used. Thus, it is vital to select material and components that are sufficient to meet the demands within the project. Since the focus is mainly on weight and size, existing integrated circuit (IC) PFC will be utilized.

In relation to the size of the converter and the make the module portable, the size and number of components needs to be reduced and the cooling system minimized. Having a portable module allows the driver to bring the off-board charger and charge the PHEV at locations where wall-sockets exist. Simultaneously, there must be a balance between delivering sufficient charging power to the vehicle and having the charger light weighted. Low weighted is desired since the potential customer should be able to lift the charger without much effort. The components temperature depends on the thermal design and the loading conditions. These components will be required to handle temperatures preferably below 150 °C, when the conversion process occurs inside the module.

Regarding the losses, it is favorable to find a converter that can perform sinusoidal current consumption, where a unitary power factor is achieved [3]. The issue in using an AC/DC converter is that it contains non-linear loads, in forms of rectifiers. These loads will provide undesirable frequency to the current and thereby increase THD. This leads to that a lower power quality will be delivered to the load [5]. To avoid this, linear loads (capacitors and inductors) are needed to compensate this, where a higher power factor can be obtained to achieve lower THD [3].

To reduce the size of the components, the switching frequency can be increased [4]. However, a higher switching frequency leads to higher losses caused by the switching elements turning on and off in a high-speed releasing transition energy per second [6]. If a conventional DC/DC converter will be used, it is favorable to implementing a galvanic insulation in the transformer of the converter, to provide safety measures [38]. Since AC/DC-conversion creates high frequency electronic noise, there is a need for control or reduction in the electromagnetic interference (EMI), using filters.

1.5 Scope

Since this project is about to design a portable battery charger exclusively for PHEVs, other types of EVs will not be acknowledged. For PHEVs, the most commonly design specification for OBC that is existing today, is designed for 230 V, 50 Hz, 16 A rates, giving an output power of 3.4-3.6 kW, 92-94 % in efficiency and a PF of > 0.99. Additionally, a standard OBC weights approximately 4 kg with a switching frequency of 98.3 kHz both for the power factor correction (PFC) and DC/DC converter. The charging optimization is considered not as important as to ensure that the AC/DC-converter module operates in the charging range, which is the main focus of this project.

After consultation with CEVT, reference values were settled to proceed from. Since the off-board charger will be operating within low power range, it is more reasonable to follow international standards. The efficiency is expected to be at least 90 % with a minimum PF of 0.9, according to international standards [7]. The power density is assumed to be approximately 1 kW/kg. Moreover, the overall weight of the module should be minimized from 4 kg, with aiming to reach a higher switching frequency than 100 kHz for both the AC/DC- and DC/DC converter since it is desirable to reduce the components size.

Since that the charger is for household applications, single-phase system is used. Other systems, such as 2-or 3-phase system will not be investigated. These households are assumed to have European standard shucko-wall sockets, limited with 16 A and 3.68 kW [8]. However, since EVs usually draw a maximum current of 10 A when connected to a wall socket, the input current level is assumed to be maximum 10 A [9]. The calculations will be based from a current level of approximately 4 A since low-power charging is desired.

The charger should also have a unidirectional flow configuration, which implies that the power from the grid is transferred one way to the battery, also known as grid-to-vehicle (G2V) [10]. The charging time is a non-issue, considering that the charger will be operating with normal charging, where it takes approximately 6-8 h to fully charge an uncharged battery [11],[12]. The high voltage (HV) battery inside the PHEV have a voltage charging range between 320-380 V. The duty cycle for the pulse sequence is assumed to be fixed.

Since the project aims towards designing an off-board charger, a thermal management system for the power electronic components inside the charger is essential to study. This is since it cannot have used the cooling system inside the vehicle. The cooling system will most probably be a heatsink, installed and mounted on the AC/DC-converter module. The module itself will assumed to have international protection marking IP67 standard [93]. In this project, robustness and impact resistance are excluded and not prioritized, due to that it is more related to material design. A construction of a prototype model and measurements are not included in this project.

The calculations will give an estimated power loss and heat values, since computing a proposed solution involves a lot of work with many choices to be assumed and motivated. Regarding the transformer in the DC/DC converter, some simplifications will be conducted. A first size of a transformer core will be selected to proceed calculations from.

A heatsink suggestion will be presented to illustrate an example of what can be used. No comparison between different heatsinks will be made, due to the thermal simulation software offer is limited. Additionally, other cooling implementation will not be taken into consideration.

Since LTspice offer a limited range of components, it will be difficult to find same components from datasheets. Therefore, the selection of components will give an approximately result. Additionally, the datasheets that are lacking information will be complemented with values from similar datasheets. The selection of specific manufactures of the components will not be considered. Conventional hard-switching technique will be used instead for soft-switching, ZVS (zero voltage switching), since it simplifies the LTspice simulation.

For the OBC, a controller area network-bus (CAN-bus) communication is required to start the OBC. Then it is possible to do voltage- and current measurements. However, this bus communication is not available since there is no laboratory set up, which means that the OBC cannot be up-started. Thus, no measurements will be conducted.

Considering the size, the data communication system is assumed to fit the size of future compact off-board charger. Therefore, a narrow investigation will be carried out to understand what data communication is required for the charger. Depending on what communication channel is needed, for an example control pilot (CP), proximity pilot (PP), CAN-bus or power line communication (PLC) will decide how the pin configuration on the DC nozzle interface will look like.

The electromagnetic-interference (EMI) will not be considered. However, the size of the input and output filters should be taken into consideration as they may have an impact on the weight and volume. Other circuits that are not a main part of the converters are neglected. The economic aspect will neither be a priority during this project. The project will be conducted over a period of five months, thus restrictions within this project are essential to pursue.

2
Method

A literature review of converter topologies were carried out, and necessary information and data were collected from related work as well. Furthermore, CEVT provided this project with an experimental OBC and a charging cable for disassembling and examination of its components and design.

An examination of the OBC was be conducted to obtain weight and size of the power electronic components. This aided to make an easier comparison between the components of the OBC and the selected components for the off-board charger. The module of the charging cable was a reference size to aim for for the off-board charger.

Since LTspice was not able to measure real power for reactive components and measure reasonable power dissipation data, calculations were carried out regarding efficiency and power losses. Simulation models in LTspice were created to verify that these values are reasonable and to obtain data about PF and THD. The switching frequency was according to standards regulations. The power density was estimated from the final charger. Additionally, to reduce the size of the components in the circuit, different topologies of power electronic designs models were investigated. These topologies were analyzed for various current levels. The first sizing of the components was done with calculations and later verified with simulation. The most applicable topology was selected to advance with for further analysis. A comparison regarding electrical performance, thermal aspects and size was made between the off-board charger and the OBC.

Decision matrix were utilized to make an informed choice by listing performance objectives, showing which factors are most important for this project and adding a weight number. The summation of the weight number and the point system together, gave the total points for the different subject and could be compared with each other. The lowest value of the total points is the selected alternative.

In order to obtain the heat and power losses, following steps procedure were conducted:

- Step 1, is to select a general solution and with reasonable components. Calculations will be based on current level variant 4 A. This will not be included in the report.
- Step 2, means that more variants are calculated based on formulas and details from step 1. In this step, power losses and heat calculations will be made.

These calculations and results are an important part of how a configuration is chosen.
- Step 3, is to sum up the calculations and values that result from the selected configuration. Choosing suitable cooling can be suggested and calculated for the chosen configuration. Finally, a reasonable design can be displayed.

A method of how to design a transformer is shown in Figure 2.1.

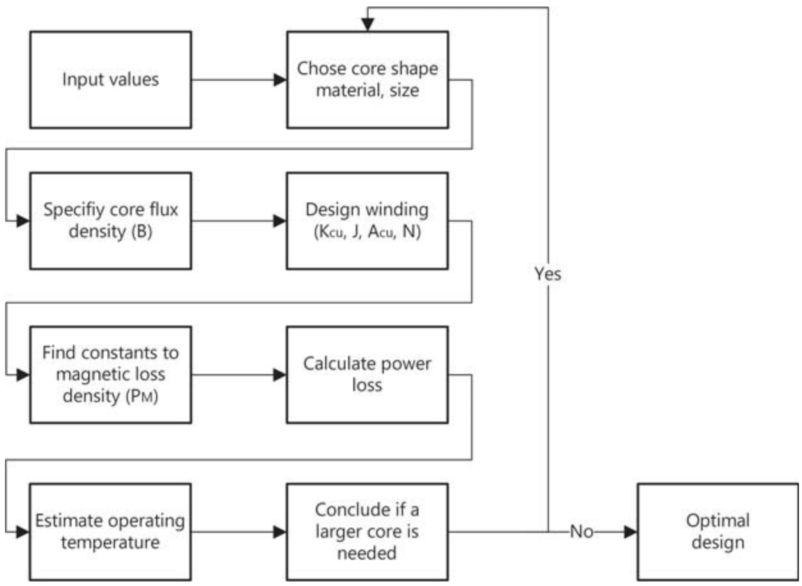

Figure 2.1: Transformer design flowchart.

Based on the selected components, the cooling system could be designed. A heatsink was designed by hand calculations to obtain the physical size. To analyze if the heatsink was sufficient enough to reduce the high-temperature levels, a simulation model was created in Heatsinkcalculator software to observe thermal radiation and critical temperatures.

By considering the choice of topology, components, size of the cooling system, including connectors, enclosures etc. the finalized size and weight of the module can be estimated. The collected information and results were recorded in a thesis report and was presented at both the company and the university.

3
Safety and Sustainability

3.1 Safety

In the recent years, the increase in sales of EVs and various charging methods has made it easier to charge the EVs in the comfort of people's own home [14]. Statistically, home charging tends to be popular, especially since it is time-saving and comfortable. Although, some caution is required when using a charging cable that comes with when buying the EV, since it might draw more current from the wall-plug (around 16 A) than the outlet is designed for. This could be due to lack of educational level on home charging, since a charging cable is included in the deal of buying an electric vehicle the customer assumes this cable can be safely utilized. Another reason why the customer chooses to use the charging cable that includes with the vehicle can be that buying a wall-box is too expensive to invest in [15]. These factors point out that the home-charging is not simple enough to use and can lead to hazard consequences for the user and others.

Since February 2018, the Swedish government decided to fund home charging installation of wall boxes (mode 3) by giving cost contribution for each household. The reason for this is to encourage more people to switch to electric vehicles. Another reason why people tend to utilize home charging could be simply that it is more convenient, where schuko outlets are having a vast distribution geographically [16].

However, considering charging for household's applications, where the customers directly connect the charger to a wall-socket, entails the possibility for cable fires to occur, which could lead to fatal outcome. This happens due to that the cables are not dimension for high power charging during a longer amount of time [14],[15]. To avoid this hazard, people are encouraged to ensure that they have a valid European standard wall-box installed in their households. Insurance companies have pointed out that the household insurance would not cover the damages of the fire if there was a cable fire with an invalid wall-box installed [14].

Considering the off-board charger, it is feasible to assume that this charger could utilize the schuko outlets. This is due to fact that it is operating as a low power charger, which would reduce the load. Thus, the wall-socket is not able to reach high temperatures, and thereby the risk for cable fires are minimized. This points out that this charger would be a safer alternative for home-charging applications. However, even if this charger is not able to reach higher temperatures, it is suggested that the shucko outlets must be equipped with a residual-current device that have the ability to break the current instantly to avoid hazards events from occurring [15].

3.2 Sustainability

In relation to the sustainability, the power system should endure multiplicity connection to the wall-sockets simultaneously, especially in the evening. This is the main issue rather than if the amount of power production is sufficient enough to sustain an operational society with power [17]. One solution could be to implement smart controllers where the loads are charged at different time points during the day depending on what needs to be prioritized, for instance, the grid or the vehicles.

Smart control of the power system could ensure that the system is not under heavy load at the same time. However, a scientist team from VTT Technical Research Centre of Finland, investigated an imaginable scenario if 5 million EVs was connected to the grid, and concluded a rise of power demand of 3.8 GW was needed if the smart control was not implemented. If the smart control was implemented, only 1 GW more of power demand was required [17]. Yet, researchers at Chalmers University of Technology predicts that this still could be an issue for smaller local grids, where the transformer capacity may not be enough to supply additional loads connected.

Simultaneously, while moving towards a renewable energy generation, it is essential to find resources that can replace coal and nuclear power in the future to achieve the extra power demand needed for the EVs. A suggestion is to implement unused charged EVs with bidirectional function, to utilize V2G technique, where the vehicle can operate as batteries to supply the grid [17]. This could benefit the grid to avoid a power outage.

This off-board charger, which is a low power charger, would not affect the power grid to the same extent as an OBC would, as it is a high-power charger. Thus, by having a lower load for the power grid to handle would likely prevent the grid from falling into power outage.

Other solutions for the future could be to redesign the current AC grid to a DC grid, thus the wall-outlets provides DC instead. This grid could provide all electronic devices including PHEVs to charge directly from the grid. Thus, the power conversion process within the vehicle or outside the vehicle is not needed anymore, leading to space-and cost savings for the PHEVs. This would likely put an end for the development stage for the OBC and the off-board charger, where these would be considered to be obsolete.

4
Theory

This chapter is presenting essential background theory regarding various technologies, approaches, and implementations to reduce overall size for OBCs. The provided OBC from CEVT is also presented with function and design specification. These descriptions will aid to find the most applicable solution for a functioning compact off-board charger for PHEVs.

4.1 Plug-in hybrid electric vehicle

A PHEV is a hybrid vehicle that belongs to the electric vehicle (EV) family. It differs from other EVs since it is equipped with both an internal combustion engine and an electric motor (EM) in its propulsion system. The battery in the PHEV can be recharged by being plugged into a power source by using a charging cable. This cable is either connected to a charging station or power outlet in a household. The range anxiety that may exist with battery electric vehicles, does not exist with the PHEVs since they will not run out of power even if the battery is uncharged [18].

4.2 On-board charger

A charger for the HV battery, known as the OBC, is located inside of the PHEV as a part of an EV's powertrain. The OBC consist of three main components; AC/DC converter, PFC controller and DC/DC converter shown in Figure 4.1. Additionally, some filters are included in the input and the output of the charger to reduce EMI. The functionality of the OBC is to convert the AC voltage from the supplying grid to DC voltage to the HV-battery of the vehicle. The stored electrical energy in the recharged battery is inverted from DC to AC voltage, which is transformed to mechanical energy via an EM to initial movement of the wheels [19].

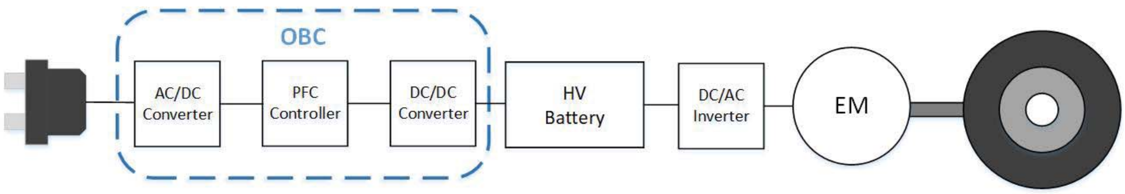

Figure 4.1: The energy conversion system inside a PHEV [20].

An overview of an OBC is shown in Figure 4.2. The AC/DC converter rectifies the AC voltage from the power source to a DC voltage, usually integrated with a Boost PFC converter circuit [21]. The DC/DC converter is isolated to give galvanic insulation ability, where the DC voltage is transformed to high frequency AC voltage. Next, this voltage is transferred, controlled and insulated through a transformer. Finally, the voltage is rectified to DC and remove high-frequencies components from the voltage [21], [22]. Both AC/DC- and isolated DC/DC converter is supervised by a controller [22].

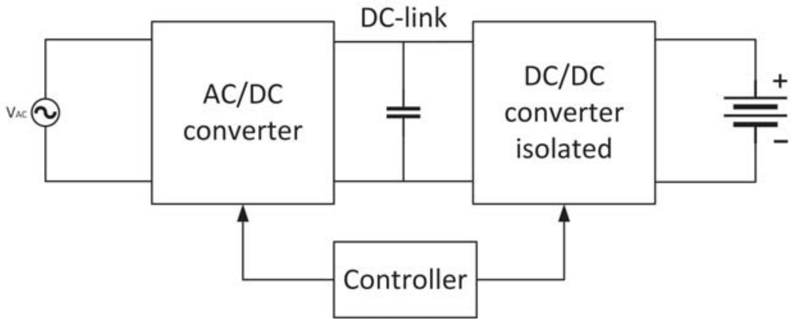

Figure 4.2: Electric vehicle battery charger architecture [23].

4.2.1 AC/DC converter

The AC/DC converter consists of a Full-bridge rectifier and Boost PFC converter, where this type of converter has the benefit to provide a low THD for the input current that includes harmonics, simple converter design and can sustain a moderated power factor. However, the Boost PFC converter size is increasing in proportion to the delivered power. This implies that if the high-power output is needed to be supplied, the converter becomes larger [22].

4.2.2 PFC controller

To achieve a sinusoidal AC output current with minimal-phase-shift between the current and voltage, it is vital to have an operational control system in the circuit. This control system is typically a closed-loop control designed as a PI- or PID controller that is controlling the gate at the switch with PWM signals [24]. The gate is alternating between on and off mode, to ensure that the inductor current is reaching the settled reference values. In other words, the PFC controller is forcing the current to be drawn in phase with the input voltage [25]. Since the error amplifier inside the controller is operating with a slow pace, it may take a certain number of cycles of the power line before the resulting output is stable [26].

The controller receives measurements of the output voltage, reference voltage, AC input voltage, and chopped average inductor current to compare these with their reference values in order to decide the amplitude and duty cycle of the PWM [24]. If there is a deviation between the reference value and measurement values, the PWM signal is modified by adjusting the duty cycle depending on the level of Boost that is required [24]. This is illustrated in Figure 4.3, where a typical conventional Boost configuration is showed.

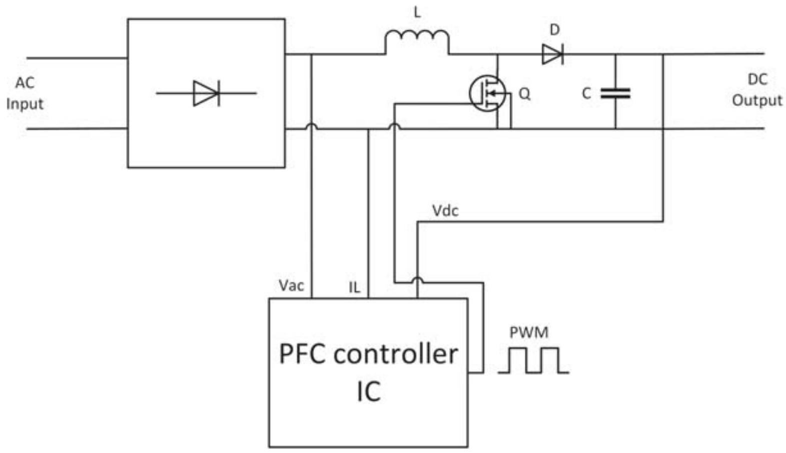

Figure 4.3: Receiving and distribution signals from the PFC controller to an AC/DC converter [27].

4.2.3 DC-link

A DC link, also known as a capacitor bank, is an intermediate stage between an input stage and output stage. This DC link commonly consists of a capacitor that is connected between two other capacitors with positive and negative ends. These stages are connected with each other by this DC link, which is shown in Figure 4.2. A common input stage is AC/DC converter (rectifier) with PFC circuit, where the DC link is operating as an output filter to prevent voltage ripple. To diminish the voltage ripple and improving the PF by reducing the reactive power, it is favorable to parallel connect several capacitors with a proper dimension [28]. For the output stage, a converter with switching ability or an inverter is usually implemented. If the AC/DC converter is operating for high power mode, the capacitance value is as low as possible to increase the storage capacity for storing energy, while converters with low power mode, needs to have low capacitance to ensure that the voltage ripple is not interfering [30].

4.2.4 DC/DC converter

A DC/DC converter is an electrical circuit that converts from a DC value to another DC value. Specifically, first, the incoming voltage is rectified to a DC, followed by switching devices that convert the voltage to a high-frequency AC voltage. Then, this AC voltage is converted back to a desired DC output voltage [30].

Within an OBC, an isolated Full-bridge DC/DC converter is used. This converter contains a transformer that provides an isolation in high-power applications, which is in this case important during battery charging. On the primary side of the transformer, there are four switches, in this case metal-oxide-semiconductor field-effect transistor (MOSFET) are used to make a Full-bridge. While on the secondary side, rectifying diodes are used. This topology can be equipped with zero-voltage-switching (ZVS), which means that there will be lower switching losses and therefore higher efficiency [31].

The DC/DC converter design is dependent on different factors such as efficiency, switching losses, and low stress. These factors need to be considered when creating a small converter size as possible [32].

4.3 Performance and size

To make the overall design of the charger as compact as possible, it is essential to reduce the size of the components and maintain high performance. In this case, the reactive components, inductors, and capacitors are desired to be reduced in size. This is because their size and volume are the largest inside the power electronic equipment and filters. In this subsection, it is presented how this can be carried out.

4.3.1 Standard regulations

EV charging applications are obliged to be in accordance with international standards regulations. These regulations show in what span the electrical performance requires to be within. For the switching frequency for the PFC, the minimum and maximum frequency is 70 kHz respectively 150 kHz, before too high distortion is obtained [33],[34]. For the DC/DC converter, the frequency range is between 140 to 350 kHz [35]. THD is accordance to EN 50160, where the supply voltage is required to be lower than 8 % [36]. The PF is desired to be at least 0.9 at full load according to IEC 61000-3-2 and IEEE-519 [24], [25]. Lastly, the majority of the OBCs have in general an efficiency of at least 90 % [37], [34]. In Table 4.1, the regulations are shown.

Table 4.1: Standards regulations for the performance of the electrical parameters.

Parameters	**Standard values**	**Unit**
AC/DC f_{sw}	70-150	kHz
DC/DC f_{sw}	140-350	kHz
THD	≤ 8	[%]
PF	≥ 0.9	-
Efficiency η	≥ 90	[%]

4.3.2 Switching technology

For the selection on what switching device to use, MOSFET and insulated-gate bipolar transistor (IGBT) are investigated since they are both within the correct range (assumed to be approximately 150-200 kHz, 600 V, and 4-8 A). From Table 4.4, it can be seen that both IGBT and MOSFET is within the right parameters for this project scope compared with other switch technologies.

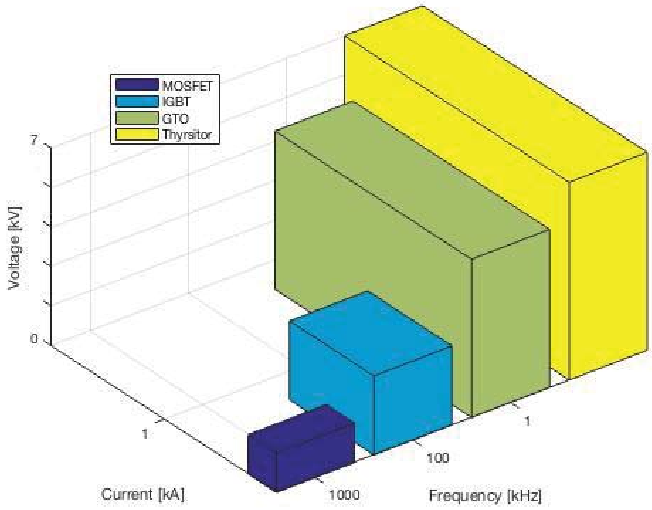

Figure 4.4: Comparison of semiconductors regarding frequency, voltage and current [39].

Therefore a comparison between MOSFET and IGBT is shown in Appendix B in B.3. From datasheets, the components are desired to have low resistance of the MOSFET as possible, since it will require less cooling [41], [42], [43].

Both MOSFET and IGBT transistors can be used, and in order to select one of the transistors for this project, a points-matrix was made. The factors that were considered most important are high switching frequency, temperature, efficiency, low $R_{DS(on)}$ and losses at high frequency. $R_{DS(on)}$ is the drain-source on resistance inside a transistor during on-state. This resistance decided the maximum current of a transistor. Since temperature and $R_{DS(on)}$ are linked together, high temperatures will increase the resistance [44].

The transistor that contains the best out of these factors has been given the grade '1' and the second best transistor has been given the grade '2' seen in Table 4.2 [40].

Table 4.2: Comparison of MOSFET and IGBT [40].

Factors	MOSFET	IGBT
High switching frequency	1	2
ZVC benefits	1	2
Higher efficiency at low voltage	1	2
Lower thermal impedance, hence better power dissipation	1	2
Elimination of current tail	1	2
Higher voltage and current capabilities	2	1
Cost at low power	2	1
Losses at high frequency	1	2
Low Rds(on)	1	2
Diode recovery behavior	1	2
Strong gate driver	1	2
On-state losses	1	2
Performance at low power	1	2
Body drain diode	1	2
Can perform fast switching applications with little turn-off losses	1	2
Lower conduction loss	2	1
Total point:	19 p	29 p

From this table, the MOSFET received 19 p while the IGBT got 29 p, hence MOSFET is selected for this project.

A MOSFET is active when supplied voltage is between the source-gate. Not until then, a drain current is conducting from the drain to source. Typically, MOSFET mitigate the switching losses since it is able to operate with a high switching frequency [6].

4.3.3 EMI filters

EMI is undesirable electrical signals, occurring in power electronic equipment due to frequent changes in both voltage and current [6]. In order to sustain a high-power quality, the arising EMI equipment needs to be mitigated, which is why it is crucial to conceal the interference [48]. This is achieved by implementing EMI filters, that eliminates high EMI by ensuring to decrease high frequency. An EMI filter consists of passive electronic components (inductors and capacitors) that mitigates and increase the resistant against interference for the devices that need to be shield [48]. A basic EMI filter can either be configured as π-filter, L-filter or T-filer [49]. A typical EMI filter for single-phase system is shown in Figure 4.5 [51].

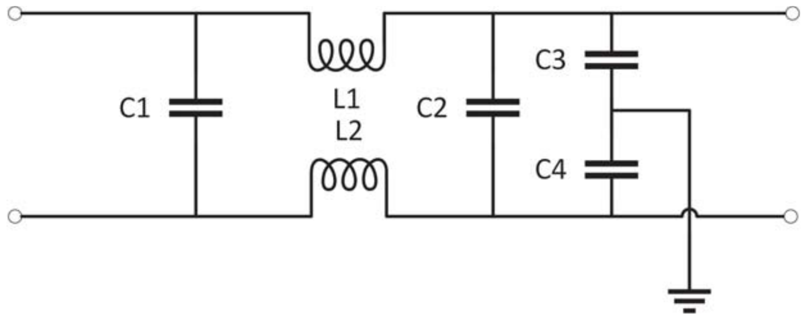

Figure 4.5: EMI filter for single stage power supply [39].

EMI filters can be designed to handle two types of noises: common mode (CM) and differential mode (DM) interference [51]. The capacitors C1 and C2 seen in Figure 4.5 is suppressing DM noise, known as the DM filter, while L1, L2, C3, and C4 are mitigating the CM interference, known as CM filter [50]. CM noise is the measurement of voltage or current between the ground and power lines, while DM noise is the measurement of voltage or current between the power lines, either as line-to-line or line-current [6].

The size of the filter can be decreased by increasing the switching frequency. However, this reduction is only true of the DM filters, meanwhile, the CM filters are slightly increased [52]. Furthermore, the inductor chokes can be mounted on the top of the filter capacitors in order to save space on the circuit board [53].

For the off-board charger, it is assumed that two EMI filters are included. Since EMI is not investigated, it is not possible to conclude how many filters are required. Thus, in order to include possible weights from the filters to the AC/DC module, this assumption is made [37], [34], [38].

4.3.4 Switching frequency

According to an IEEE article, an experimental attempt was made to make a compact high efficiency 3.3 kW OBC. The switching frequency was selected to 70 kHz for a PFC circuit and 200 kHz for a ZVS Full-bridge DC/DC converter [34]. For the PFC circuit, 70 kHz was selected to fulfill the EMI regulations, which implies that a switching frequency should be below 150 kHz. For the DC/DC converter, a switching frequency of 200 kHz was selected to ensure that the losses are minimum at full performance of the OBC. This is based according to Figure 4.6, where the ratio of the efficiency and output power is shown for an output voltage of 300 V [34]. This is reasonable to assume for this project since the HV battery requires an operation range of at least 320-380 V in order to charge.

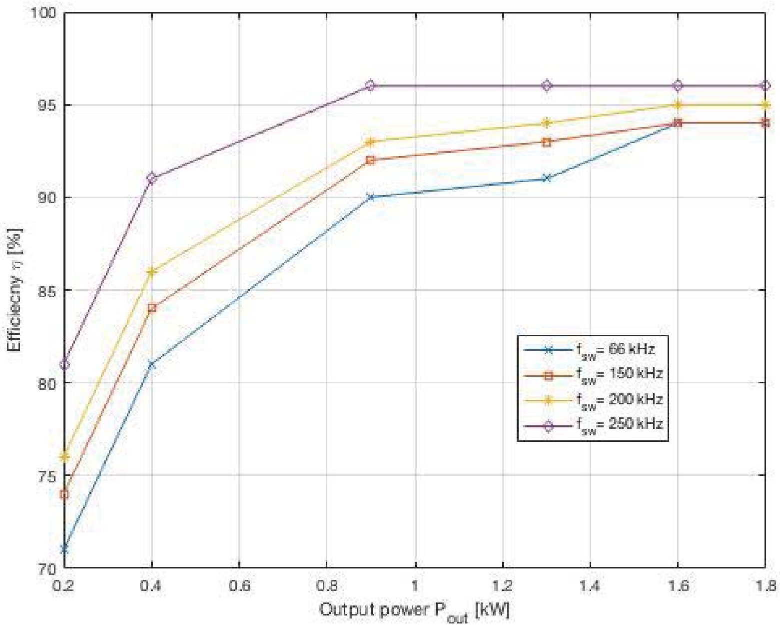

Figure 4.6: Output power from the DC/DC converter in relation to the efficiency at various switching frequency levels [54].

As shown in Figure 4.6, the efficiency is increasing with higher frequency, and increasing further with higher power output from the DC/DC converter. However, a too large switching frequency is undesirable to use since the inductors- and capacitors components are manufactured within a limited range of size [4].

With the case of the off-board charger, it is suggested to use a switching frequency of 150 kHz to reduce the components size for the PFC circuit. Since this project is about to design a low-power charger, an output power range between 800 W and 1200 W is more appropriate to expect from the DC/DC converter, seen in Figure 4.6. From this range, 900 W is selected for further research. Considering the switching frequency, a too high frequency would lead to higher switching losses in the switching devices. Therefore, a frequency of 200 kHz is selected to obtain a high reasonable efficiency of 92 %, avoiding too large losses and ensuring that the size of the components is reduced.

4.4 Power factor correction

In order to obtain the highest power quality while designing AC/DC converters, it is fundamental to establish a reasonable PF and THD, that follows international standards. PF is described as the ratio between real power (P) and the apparent power (S), or as if there is phase-shift between a sinusoidal current- and voltage waveforms, the equation can be expressed as [55].

$$PF = \frac{P}{S} = K_\theta \times K_d. \tag{4.1}$$

With a phase shift, the cosine of the phase angle between the current and voltage is established. This known as the displacement factor $K_\theta = cos(\Phi)$. The second parameter, distortion factor $K_d = \frac{I_{RMS(1)}}{I_{RMS}}$, determines how sinusoidal the waveforms is [7].

Since the real power is the transferred component, the reactive power (Q) must be as low as possible. This would give PF closer to 1.0, known as unity, where the active power is equal to apparent power. A sinusoidal current and voltage that are in phase with each other imply that PF is close to 1.0 [24]. This is known as a linear load. If the waveforms are sinusoidal but not in phase, the PF is not equal to 1.0 [55]. This is known as non-linear load [58]. This is illustrated in Figure 4.7, where the current spikes representing harmonic currents.

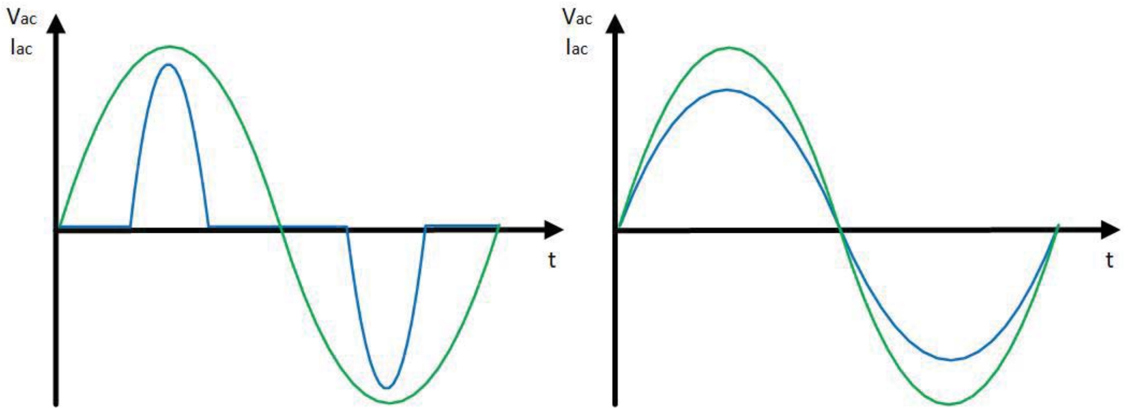

Figure 4.7: Illustrating the voltage- and current characteristics waveforms by not having a PFC to the left, and by having a PFC [59].

In order to reduce the distortion and ensure that the input current is in phase with the input voltage, known as a resistive load, a power factor correction (PFC) is needed. This would improve the overall power quality, where reduction of current harmonics, low output voltage ripple, increase efficiency, multiple output voltage levels, fast output dynamics and good load regulation. PFC is also a requirement within AC/DC-converters according to international standards, such as IEC 61000-3-2 and IEEE-519 [55]. For a power supply with PFC, the PF is expected to be between 0.95-0.99, while a power supply without PFC has a PF of 0.70-0.75 [60].

THD is defined as the level of distortion at the input current in this case shown as [6]

$$THD_i = 100\% \times \sqrt{\frac{1}{K_d^2} - 1} \tag{4.2}$$

Considering a linear load in equation 4.1, thus K_θ=1, gives $PF = K_d$. This implies in

$$PF = \frac{1}{\sqrt{1 + (THD)^2}} \tag{4.3}$$

Since PF is linked to the total harmonic distortion, an increase in THD will result in a decrease in PF. This is not desired since harmonic distortion can cause damages to cable, create overheating, circulating currents, fire risk, equipment malfunction and component failures [57].

4.4.1 LT1248 - PFC controller

The IC LT1248 is a universal controller with power factor correction. It can regulate to a maximum power of 1500 W and is able to operate in both continuous conduction mode (CCM) and discontinuous conduction mode (DCM) [61]. An overvoltage protection circuit is located at pin 8, where the output voltage is decided based on the equation as follows

$$V_{out} = V_{ref} \times \left(\frac{R1 + R2}{R2}\right) \tag{4.4}$$

where V_{ref} is the reference voltage, set as 7.5 V for this IC. The schematic model of the LT1248 in LTspice is shown in Figure 4.8.

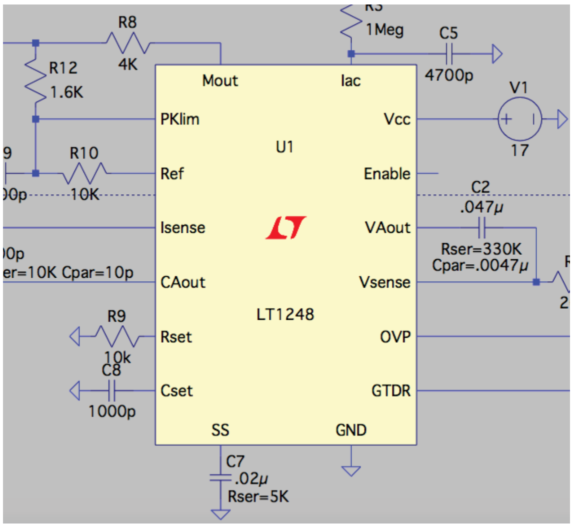

Figure 4.8: Schematic of LT1248 PFC controller in LTspice.

It has maximum switching frequency of 300 kHz internally. At pin *Rset* and pin *Cset* of the IC, the switching frequency can be determined. Since the switching frequency is equivalent to the oscillating frequency, it can be calculated according to the forumla

$$f_{sw} = \frac{1.5}{R_{SET} \times C_{SET}} \tag{4.5}$$

where R_{SET} is the the set resistor and C_{SET} is the set capacitor [61]. These values are selected from a frequency graph found in the datasheet for this PFC.

For this project, several IC designs were considered, but since this PFC controller had the highest maximum output power, this controller will be selected for the LTspice simulation.

4.5 Topologies

Different topologies for both AC/DC and DC/DC circuits are presented and one of each is selected for this project.

4.5.1 AC/DC converter with PFC

To access an overview of some different common (active) PFC topologies, such as the Classic Boost PFC, Dual Boost PFC, Totem-pole Bridgeless PFC and Interleaved Boost PFC, a few of their characteristics are presented in Appendix B in Table B.5.

In order to decide between what PFC topology to use in the off-board charger, a comparison table of characteristics between different PFC topologies is made. From the most important factors like the number of components and suitable for low power rating, the classic Boost, and Totem-pole Bridgeless PFC are both selected for further investigation.

Furthermore, to be able to select an optimal PFC for this project, a comparison between only classic Boost PFC and Totem-pole Bridgeless PFC is made, which can be seen in Table 4.3. From the table, some of the factors have been given higher priority such as the number of components being used, efficiency and power rating, marked with a $\star$.

In Table 4.3 there is a point system, where the grade "1" means the best characteristics and the grade "2" means secondary.

Table 4.3: Comparison of Classic Boost PFC and Totem-pole Bridgeless PFC.

Factors/Topology (PFC)	**Weight**	**Classic Boost**	**Totem-pole Bridgeless**
Low EMI		1	1
Power rating	$\star$	1	1
Number of components	$\star$	2	1
Efficiency	$\star$	2	1
Switching losses		2	1
Inherent ZVS		2	1
High frequency noise		2	1
Simple control		1	2
Cost		1	2
Common-mode interference		1	2
Can use Si, GaN, SiC (or only possible with GaN or SiC)		1	2
Total		16	15

The total points when looking at these factors are shown in Table 4.3, where it is seen that the Totem-pole receives the lowest amount of points, which is the preferable one.

However, the score is even between the classic Boost and Totem-pole. Therefore, simulation and calculations regarding the electrical performance of both Boost and Totem-pole will be conducted.

However, with an additional weight of '×2' at the prioritized factors marked with stars, the total scoring becomes 21 points for Boost and 18 points for Totem-pole. Thus, if other selection methods between these two typologies are not conducted, Totem-pole is selected.

The classical Boost PFC is one of the most common PFC application on the market. It can receive a peak line voltage between 0-375 V, and provide an output voltage of more than 380 V. It is equipped with a Boost inductor after the rectifier bridge, which generates a continuous smooth current. This gives the benefit that no more filter is required to be implemented, thus, lower cost for the topology [45]. The circuit design for the AC/DC converter with Boost PFC topology is shown in Figure 4.9.

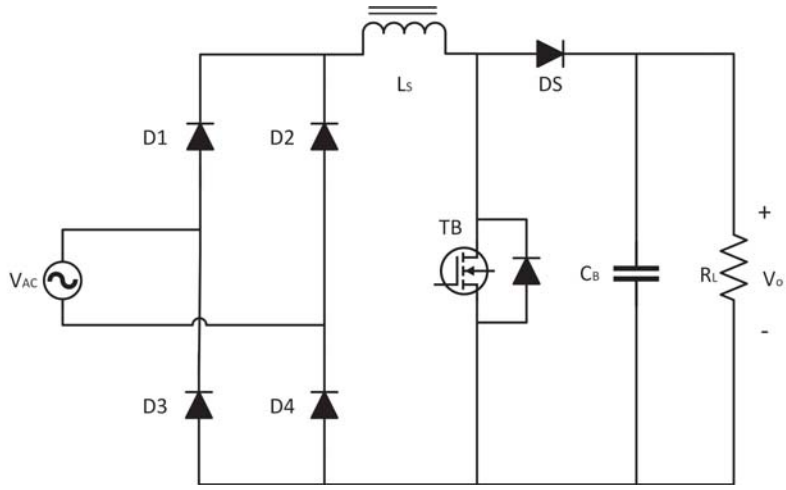

Figure 4.9: AC/DC converter with Boost PFC configuration [66].

Compared to the Boost PFC, the Totem-pole PFC have fewer number of components and low conduction loss [67]. Additionally, it provides a higher power density, higher efficiency and low CM noises [68]. For the PFC operation, the Totem-pole is active during the positive half and negative half cycles of the AC input waveform. The current flow is adjusted by determining the switching frequency for the transistors. The AC/DC converter with Totem-pole PFC topology is shown in Figure 4.10.

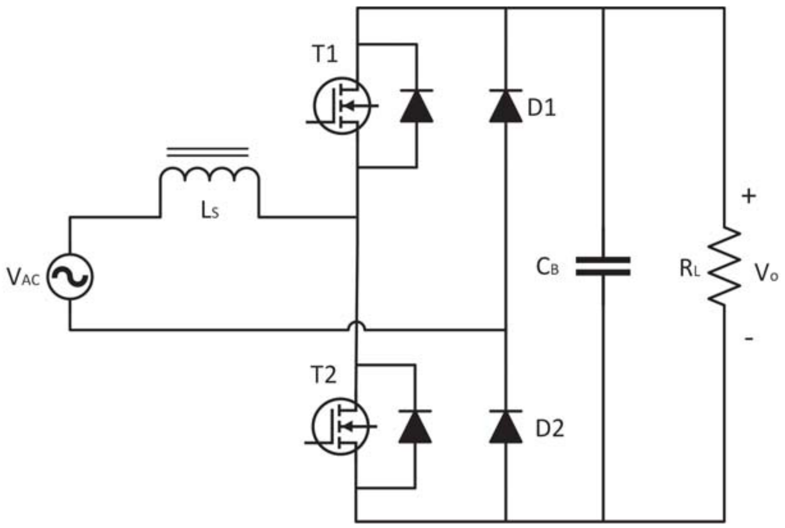

Figure 4.10: AC/DC converter with Totem-pole PFC configuration [66].

Operation mode
It is required to select an appropriate operation mode to calculate values for the components in the selected PFC. Hence a comparison has been conducted between the operation modes CCM, critical conduction mode (CrM) and DCM which can be seen in Appendix B in Table B.4.

To select an operation mode to use, a comparison points-matrix was created. The factors that were considered most important are stress on components, losses, low di/dt, these factors are also marked in the weigh column with a $\star$. The grade '1' in Table 4.4 represents the mode with the best abilities for the different factors.

Since the DCM operation mode has the highest peak current compared to both CCM and CrCM without any major advantages over CrCM, as shown in Appendix B, the comparison will be between CCM and CrCM in Table 4.4 [69]. A weight '×2' has been added to the most important factors shown with($\star$) in Table 4.4.

Table 4.4: Comparison in operation modes [69].

Factor	Weight	CCM	CrCM
Switching frequency	$\star$	1 (easier to filter)	2
Switch stress	$\star$	1	2
Inductor stress	$\star$	1	2
Diode stress	$\star$	2	1
Losses (at medium-high power)	$\star$	1	2
Cost		2	1
Large inductor value	$\star$	2	1
Low energy		2	1
Performance		1	1
Power saving (low power)		2	1
Improving power density (low power)		2	1
Low di/dt, can reduce EMI	$\star$	1	2
Turn-on losses (with MOSFET)		2	1
Total points:		29p	30p

As shown in the table, the total points were even, where the CCM received 29 p while the CrM collected 30 p. From Table 4.4, operation mode CCM is selected.

4.5.2 Material

With the selected transistor to be MOSFET from Table 4.2 and the selected operation mode to be CCM from Table 4.4, there will be turn-on losses to take into consideration. To avoid too high losses, a low value of the reverse recovery charge (Qrr) is needed. Hence to obtain a low-value Qrr, ultra-fast diodes or silicon carbide Schottky diodes can be utilized at CCM mode [45]. Ultra-fast diodes improve the efficiency and can be implemented in AC/DC conversion equipment [46]. Schottky diodes are commonly used for hard-switching implementation and EV applications [47].

4.5.3 DC/DC converter

The majority of OBCs on the market are equipped with a Full-bridge converter configuration for the DC/DC converter stage [34], [74], [37]. Thus, the DC/DC converter for this project is investigating the Full-bridge. Furthermore, the Half-bridge topology is also analyzed since it might have a less impact on the size and weight.

There are two types of Full-bridge converters, Full wave bridge rectifier and Full wave center tapped rectifier. The main difference is that the Full wave center tapped has a bulky center tapped transformer, which is also costly. Therefore, the full wave bridge rectifier is preferable to investigate since it is smaller in size and less costly. From here on out, the Full wave bridge rectifier will be referred to as only Full-bridge converter [75].

A Full-bridge converter consists of four switches and four diodes, divided into two legs, shown in Figure 4.11 There are two switches on one leg and they do not conduct at the same time. However, to avoid short-circuit on the DC input, the switches are turned-off during a short 'blanking'-time. If ideal switches are assumed then the switches are not turned-off simultaneously [6].

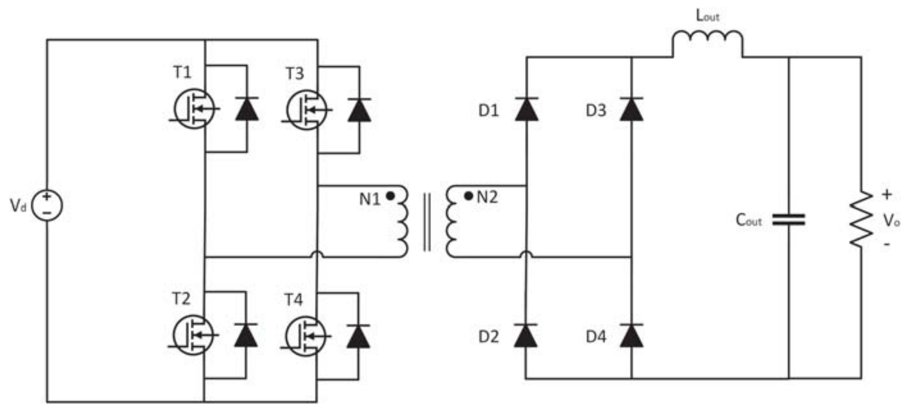

Figure 4.11: Isolated Full-bridge DC/DC converter [39].

The Full-bridge converter is designed with four switches, where the switch pair T1 and T2 are switched on together and T3 and T4 are then off until they shift. The Full-bridge converter also has an electrically isolated transformer. Some advantages and disadvantages for this Full-bridge converter are presented in Table 4.5

Compared to the Full-bridge, the Half-bridge DC/DC converter only has one leg with two switches and two diodes or capacitors. This is illustrated in Figure 4.12.

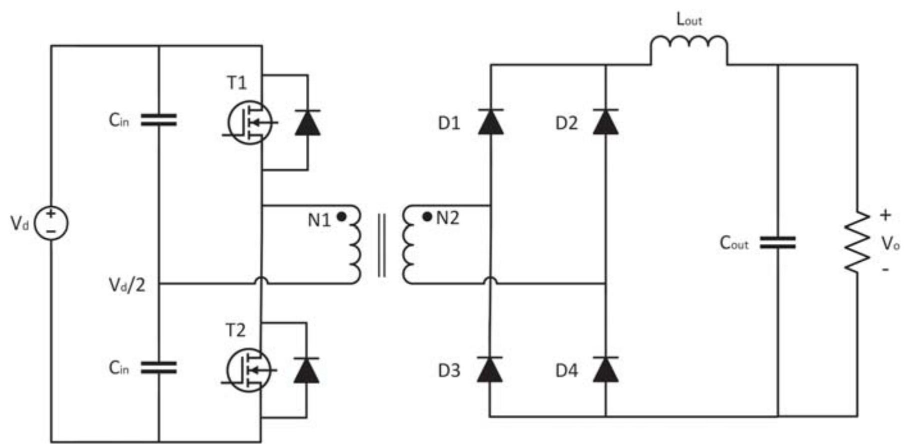

Figure 4.12: Isolated Half-bridge DC/DC converter [39].

The capacitors C1 and C2 are arranged to create a voltage potential point. For the switches, T3 and T2 are operating separately from each other. The diodes connected in parallel from the switches are used to protect the switches [6]. The advantages and disadvantages of the Half-bridge are listed in Table 4.6.

Table 4.5: Advantages and disadvantages of the Full-bridge converter [76],[77], [78].

Full-bridge DC/DC converter	
Advantages	**Disadvantages**
Utilized for high power applications (>1kW)	High number of components is required.
The output voltage of a Half-bridge is twice as large, giving higher power rating. This gives the possibility to reduce the number of windings as well, and yet remaining with the same output voltage.	Less economical alternative, in relation to high conductive losses if this converter is operating for low power rating.
Utilizing four diodes to rectify and polarity change the incoming wave.	Higher losses than the Half-bridge converter, due to it have more switches components.
An efficiency between 90-98 %.	More voltage ripple than a Half-bridge.

Table 4.6: Advantages and disadvantages of the Half-bridge converter [76], [77], [78].

Half-bridge DC/DC converter	
Advantages	**Disadvantages**
Utilized for high power applications (250W - 1kW).	At the DC bus, the supply potential is half-sized, thus the output voltage is reduced. This implies that the current needs to double to obtain the same power output. Thus, the transformer core needs to be large.
Air gap of the magnetic path is not needed.	Current mode control is not applicable for this converter.
Cheaper and simpler to design.	Two capacitors connected in series are required at the input of the bridge and needs to have a large design due to the capacitance is halved.
Lower switching losses than the Full-bridge converter, due to that it has fewer switches components.	Since only two transistors are operating, they are required to handle twice as large conducting current, resulting in high losses.
An efficiency between 88-96 %.	

Since a comparison between different output power from 900 W, 1300 W and 1700 W are conducted, both Half-bridge and Full-bridge may theoretically be suitable candidates for external charger application. Simulation and calculations of both Full-bridge and Half-bridge will be conducted to analyze which one is most preferable to utilize.

4.5.4 Number of components

To see the difference clearer between the number of power electronic components used for the selected topology circuits, a list is summarized in Table 4.7. The Boost and Totem-pole circuits represent the selected AC/DC converters, while Full-bridge and Half-bridge represent the selected DC/DC converters. EMI-filter components are not included in the list since they will be included in the final topology selection for all cases.

Table 4.7: The number of power electronic components in the selected circuits.

Circuits/ Components	Diode PFC	Inductor	Switch	Trafo	Bridge-diodes	Capacitor	Total
Boost	1	1	1	0	4	1	8
Totem-pole	0	1	2	0	2	1	6
Half-bridge	0	1	2	1	4	3	11
Full-bridge	0	1	4	1	4	1	11

4.6 Cooling implementation

In this project, the off-board charger needs a cooling system to reduce high temperatures generated at the heat loads. This cooling system should have a size that can be encapsulated into the ‘module of the charging cable’ structure. Since the structure is enclosed, it might be difficult find a balance between having an efficient thermal management system and simultaneously prevent dust and moisture from infiltrating. The aim is to find a cooling system for a sealed or semi-sealed module [79]. The cooling system that is used in this project is natural or convection cooling, where the heat is transferred by air flow.

To use the natural air flow efficiently, there is a need to add vents to the enclosed electronic equipment including a cooling fan. To prevent dust contamination while using vents, air filter units can be used [81]. A filter is necessary to use since dirt and moisture in combination can become conductive and thus can cause intermittent operation. For high power applications, convection cooling may not be practical to have due to the cost and size required. However, for this project it might be appropriate to implement cooling channels or pipes where the incoming air can be equally distributed over the module.

An alternative to this could be to transfer the heat from the components to outside of the enclosed module. This can be achieved by using a heatsink as a roof of the charger module, that transfer and remove the heats. The high temperature producing components ought to be mounted directly in contact with the heatsink and evenly spaced to make the heat transfer as efficient as possible. An idea for a starting point with an enclosed module is shown in Figure 4.13 [82].

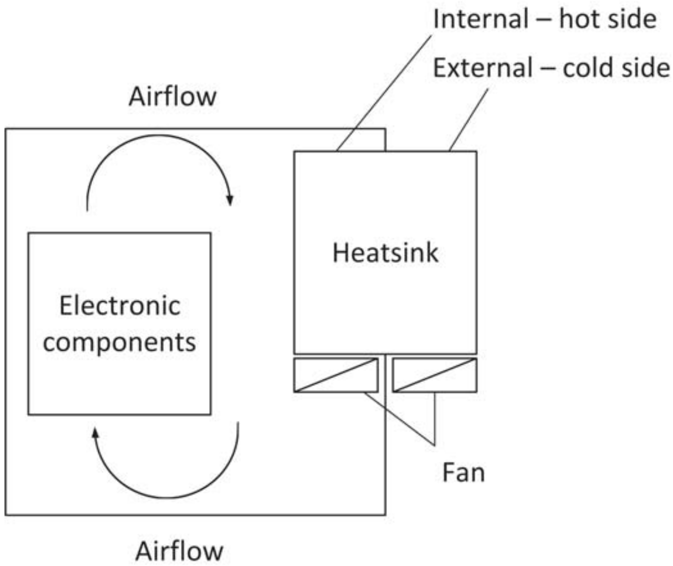

Figure 4.13: Sealed module enclosed with thermoelectrically enhanced heat rejection [80].

4.7 OBC from Geely Group

A specific OBC, named Geely 8888003014 G BQ8AA, was provided by CEVT for this project. This OBC was designed in 2017 by Geely Group and assembled here in Sweden. However, at the moment, a new model is under developing stage and is scheduled to be complete in 2018, where this model includes equivalent electronic components as in the 2017 model. The circuit board for the data communication system inside the OBC is manufactured by Kongsberg Automotive [37]. In Figure 4.14, the physical OBC is shown.

Figure 4.14: OBC Geely 8888003014 G BQ8AA from a PHEV.

4.7.1 Design specification

According to design specification of the OBC, this battery charger is a 1-phase 3.4 kW charger for PHEVs, where the power electronics and cooling system are packaged in a 4 liter metallic module. This gives a total weight of approximately 4 kg [37]. The maximum current rate of 16 A can be received from the grid to the OBC. For protection against environmental contamination, IP67 and IP6K9K standards are implemented into the shield design. The design specification for the OBC is listed in Table 4.8.

Table 4.8: Design specification of OBC - Geely 8888003014 G BQ8AA [37].

Specification	Values	Units
AC input voltage range	85-264	Vac
AC input frequency range	44-65	Hz
AC input current	2-16	A
DC output voltage range	200-410	Vdc
DC output power	3.4	kW
PFC - switching frequency	98.3	kHz
DC/DC - switching frequency	98.3	kHz
Efficiency	92-94	%
PF	> 0.99	-
Power density	1	kW/kg
Dimension (H x W x L)	6.8 x 19.2 x 25.5	cm
Weight	≤ 4	kg
Volume	3329.28	cm^3
Ingress protection	IP67	-

4.7.2 3 separated connectors

In order for the OBC to operate properly, there are three separated inbuilt connectors. These connectors are one AC connector, DC connector, and LV connector. The AC connector receives the incoming power from the charging cable, supplied from the AC grid, which is plugged into the power outlet. The DC connector delivers the converted DC power to the battery inside a PHEV. The LV connector receives and sends signals channel through a communication CAN-bus between the battery and the charging cable to establish sufficient and correct current level for the battery [37].

4.7.2.1 AC connector

The AC connector consists of five input pins. PIN1, PIN2, and PIN3 are corresponding to L1, protective earth (PE) to the chassis of the vehicle and neutral (N). Between the one single-phase conductor L1 and the neutral connector, receives up to 230 V. PE is the protective earth that protects equipment and people. PIN4 and PIN5 are interlocked connections that receive 15 mA. These connections are implemented for safety measurements, to ensure it is only possible to charge when there is a connection between the cable and AC connector at the electrical vehicle inlet (EVI). It has a weight of 103 g [89]. The pin-configuration for the AC connector is illustrated in Figure 4.15 [37].

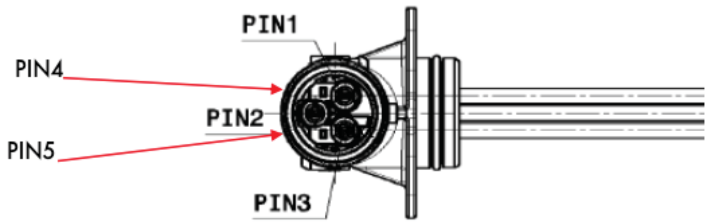

Figure 4.15: AC connector with pin-configuration [37].

4.7.2.2 HVDC connector

The DC output consists of four output pins. PIN1 and PIN2 are corresponding to DC+ and DC-, where it is supplying between 200-410 V output voltage for the HV battery. Similar to the AC connector, the DC connector is also having PIN3 and PIN4 as interlocked connections. It has a weight of 106 g [89]. In Figure 4.16, illustrating the pin-configuration for the DC connector [37].

Figure 4.16: AC connector with pin-configuration [37].

4.7.2.3 LV system connector

The low-voltage (LV) connector receives and sends signals through a communication CAN-bus between the battery and the charging cable. This communication line is established in order to ensure sufficient and correct current level is delivered to the battery to avoid any damages to the battery. In regard to safety aspects, other signals are being sent to locking the engine during charging process [37]. This connector has a weight of 82 g [89].

4.7.3 Circuit diagram

According to the available documents from CEVT, the OBC is suggested to have a typically HV board architecture. This architecture is constructed with an AC/DC converter with interleaved PFC circuit coupled together with an isolated Full-bridge DC/DC converter. Both the interleaved PFC circuit and DC/DC converter are having a switching frequency of 98.3 kHz. Additionally, various type of filter is implemented at the front and end of the charger to mitigate the level of occurring ripples and thereby establish a higher level of power quality. A schematic diagram of the OBC is shown in Figure A.1 Appendix A.

4.7.4 Data communication

In order for the charger to know when the battery is fully charged or needs to be recharged, a data communication line is required between a vehicle and power supply station. At present, the connector is equipped with two separated communication contacts: CP and PP. A CP is used for transmitting significant information using pulse width modulation (PWM) signals, while PP ensures that the engine startup sequence is deactivated, the cable is attached to the EVI, and maintaining ampacity during the complete charging process [83]. Ampacity is the maximum rated current that is conducted through a cable to withhold a safe temperature level [84]. Both CP and PP detects if the cable is attached to the vehicle, and are being transmitted through the EVI. The return signals back to the charger is going by the PE. When the battery is fully charged, the charging process is aborted inside of the vehicle and release the connectors by a break apparatus [37].

Depending on the geographic location in the world, the configuration arrangement of the connector has different styles to benefit the market and customers. CP and PP are often arranged symmetrically from each other either combine with the phases. For single-phase function, CP and PP are combined with L1, N, and PE, and for single-and three-phase as L1, L2, L3, N and PE [85]. In Table 4.9, the different configuration arrangement is described, where GB is a Chinese abbreviation for *Guobiao* and CCS stands for combined charging system [85].

Table 4.9: Type of connectors with configuration arrangement of the contacts [86].

Mode/type	**Type 1 (US**	**Type 2 (EU)**	**GB (China)**	**Japan**
AC	SAE J1772/ IEC 62196-2	IEC 62196-2	GB Part 2	IEC 62196-2
DC	Tesla US	Tesla EU	GB Part 3/ IEC62196-3	CHAdeMO/ IEC62196-3
CCS (AC+DC)	SAEJ1772/ IEC62196-3	IEC 62196-3		

4.7.5 Operation of OBC

The OBC Geely 8888003014 G BQ8AA follows a specific operation pattern before, under and after the charging process. This is regulated and controlled by the micro-controller unit (MCU) SPC560B54L3B4E0 located on the low voltage board system. This operation pattern is shown and listed as following [37]:

1. Charging system is blocked when the propulsion system (electrical- and combustion engine) is running.
2. Propulsion system is blocked when the charging system is about to charge.
3. Data communication through the EVI, where CP and PP detect if the charge cable is attached to the vehicle. If the cable is attached, OBC will wake up from it sleeping-mode and begin to perform CAN communication with the HV battery.

4. The OBC receives essential data, maximum voltage, and current limitation, from the HV battery. This is done to know how much generation the OBC is allowed to produce and to avoid any damages on the battery.
5. While the CP and PP limit the maximum current from the AC grid.
6. As soonest the levels from the grid and HV battery are verified, the motor is locked and cannot be ignited. Simultaneously, the cable is attached to the vehicle. At this stage, the LEDs in the EVI illuminates yellow.
7. Through the EVI, OBC updates the charger with previous status information if the cable connected, charging rate, error etc.)
8. When PP, CP and AC voltage from the grid is approved, a digital signal processor (DSP) inside the OBC activates the charging process with a signal. Now, the LEDs in EVI illuminates with green lights
9. Through a CAN communication, the vehicle dynamics domain master (VDDM) permits for unlocking the cable from the vehicle and abort the charging process.
10. As soon as the cable is detached from the vehicle, the motor is being unlocked, and the propulsion system can be ignited again. LEDs in the EVI illuminates with yellow light.
11. When the cable is unplugged from the EVI, the LEDs illuminates with white light.
12. CAN Communication from the OBC begins to cease, and goes back to sleeping-mode.

4.7.6 Heat losses

The only measured data over the thermal losses for the OBC as a component itself was available. These data are presented in Table 4.10, where the efficiency from the OBC for different currents ratings is presented. The rest of the efficiency are thermal dissipation. This is measured with a 230 V (RMS) and 50 Hz supply as an input. The output voltage is selected to be 375 V since this level is close to the battery start charging point, 380 V. For this output voltage it requires a cooling temperature of 40 °C. As shown in the table, various input current and output voltage ratings affect the amount of heat dissipation. By having a higher current, leads to that lower heat losses are obtained. Vice versa, by having a lower current- and voltage rating gives higher heat losses [87].

Table 4.10: Efficiency and power dissipation of the OBC with various currents. These data was measured with a cooling temperature of 40 °C [87].

Input current [A]	Output voltage [V]	Efficiency [%]	Dissipation [%]
2	375	88	12
4	375	92	8
6	375	93	7
8	375	93	7
10	375	94	6
12	375	94	6
14	375	94	6
16	375	94	6

4.7.6.1 Transformer losses

According to a test report from 2016, the highest power losses occurring internally of the OBC is located in transformer [88]. These losses are generated by listed as:

- DC losses
- Skin effect losses
- AC losses due to proximity effect

These parameters are based on winding losses in transformer shown in Figure 4.17.

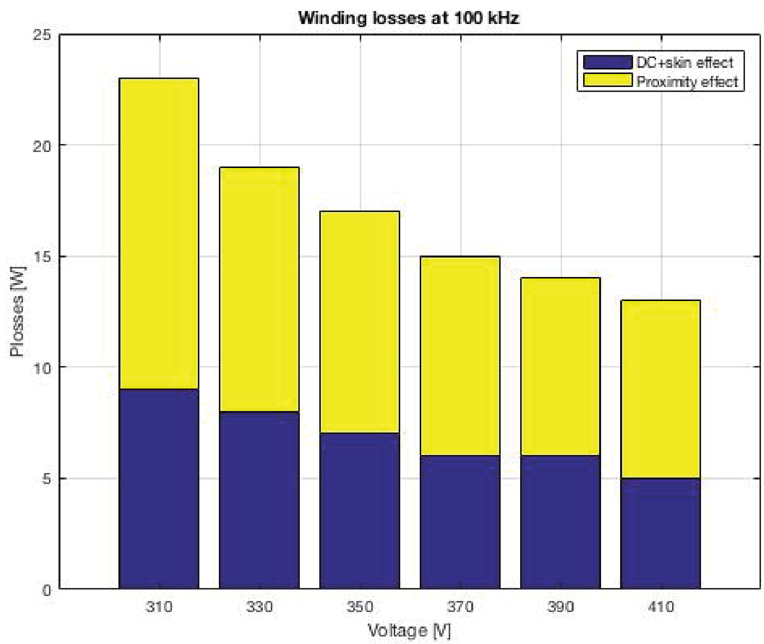

Figure 4.17: Losses in the winding in transformer at 100 kHz [88].

The Litz wire is assumed to have 32 strands, giving a cross section of 1 mm^2. It should be noted that transformer is provided with thermal interface material near the surface of the transformer and capacitors [88].

4.7.7 Weight and volume

From a datasheet about assemblies and materials related to the Geely OBC, information about power electronic components serial number, quantity and their weight was given [89]. However, the given datasheet is not the latest version, which suggests weight and size estimation needs to be conducted for each power electronic component inside the OBC. Their weight and size are described in subsection 5.1.2.

For the off-board charger, the weight and volume of the components are being estimated based on data from datasheets. These components will be compared with the components from the Geely OBC.

4.7.8 Thermal management

In order to reduce heat losses occurring at the heat loads, such as combustion engine inside the vehicle, requires a thermal management system. This type of system typically uses liquid cooling through pipes which is highly effective in removing heat dissipation. This type of cooling system is also implemented in PHEVs, where one of the heat loads is the OBC. The cooling system for the OBC is shown in Figure 4.18.

Figure 4.18: Back side of OBC, where the cooling system is equipped with cooling pipes mounted to remove heat dissipation from the components.

The cooling system has an estimated weight of 893.11 g. The heat load or charging-load is the only load occurring during the charging process when the vehicle is not moving, it implies that the drive-load can be excluded. To avert higher volume and size of the cooling system, one single heatsink may be sufficient to utilize for both loads [90].

In order to protect the OBC from environmental contamination, such as rain, dust, and sand, it is packed inside an impenetrable enclosure. To ensure to avoid high temperatures that are damaging the OBC, the walls of the enclosure is connected to the heat loads to diverting the heat to the outdoor air. Additionally, while selecting the insulation material to the walls of the enclosure, it needs to have a tolerable range for the electrical insulation and thermal conduction [90]. Considering an OBC with a charging rate of mode 1, delivering an efficiency of approximately 94 % with a power dissipation of 250 W [90].

In relation to this project, water cooling pipes is not an option since the charger will be outside the vehicle. Therefore, a heatsink implementation would be used. If a heatsink would not be sufficient to reduce high-temperature levels, air cooling in combination with a heatsink is another alternative to utilize.

Additionally, to reduce the thermal further and saving weight for the OBC, heat pipes can be scattered over the base of the heatsink. This transport and condense the heat towards the flanges of the fan, and simultaneously increasing the power density. Installation of a liquid cooling plate for the power electronic devices can mitigate the temperature lower. These plates are often customized in regard to the power density, heat loads, and type of material that is selected. The heat loads are often transmitted over to the protected package where the heat is highly concentrated [90].

The pad size of each component on the printed circuit board (PCB) of the heatsink, is recommended to be larger than the component itself [34].

4.8 Charging cable from Mennekes

The mode 2 charging cable for EVs, designed by Mennekes, is produced to be utilized as an emergency charging cable only. An emergency scenario could be if there is no accessible charging infrastructure. For this reason, it is not designed to operate as a permanent charger for the load, compared to a charging station, which is a continuous load and is in accordance to the IEC 61851-1 standard [91]. The length of the cable is approximately 4 meters long [92].

The charging cable is connected to a certified commission for conformity testing of electrical equipment (CEE) wall sockets or households. To avoid high temperatures, the cable is equipped with a module, where an integrated heat-tracking device is included to ensure the cable itself, vehicle nor battery get damaged [91], [92]. When the temperature is too high, it breaks the current and thereby the charging process. As soon as a reasonable temperature level is reached, the charging process is initiated again. The module of the charging cable is presented in Figure 4.19.

Figure 4.19: Charging cable with control and supervision module.

Since it is connected to a power outlet, it is using single-phase operation, where the delivering current rate is having an adjustable range between 4-8 A. Considering the robustness of the cable, it can withstand a weight of 500 kg. One important safety feature, it is only operating and delivering power to the vehicle when it is connected properly to the EVI. In relation to contamination protection, it has an IP67 standard, implying it is fully dust protected and waterproofed [93], [91]. These design-specification is summarized and presented in Table 4.11.

Table 4.11: Design specification of Mennekes charging cable [92].

Mennekes charging cable with Mode 2 charging for EVs	
Protection	IC-CPD 1 protection (IP67)
AC grid	Single-phase operation, 230 V, 50 Hz, 30 mA
Delivering current rate	4-8 A with maximum 8 A
Dimension (H x W x D)	5.2 cm x 24.0 cm x 10.0 cm
Temperature range:	-32$\leq T_{amb} \leq$ 40 C°

This module from Mennekes will be used as a reference design, where the aim is to design a module with similar dimension for the off-board charger.

4.9 Thermal calculations

4.9.1 Power losses

In this subsection, the loss calculations will be discussed in more detail supplemented with relevant equations [69].

Diode
To calculate power loss for the input rectifier diode bridge, the following equations are needed

$$P_{conduction} = V_F \times I_{avg} \tag{4.6}$$

where the value of the voltage drop V_F is obtained from datasheet.

The switching loss of a diode can be calculated by

$$P_{switching} = (E_{on} + E_{off}) \times f_{sw} \approx E_{on} \times f_{sw} \tag{4.7}$$

where E_{on} is the energy during on-state and E_{off} the energy during off-state.

The E_{on} can be known by using

$$E_{on} = 0.25 \times Q_{RR} \times V_R \tag{4.8}$$

where Q_{RR} is the reverse recovery charge, V_{RR} is the reverse recovery voltage.

By adding the conduction and switching losses together, the total diode loss becomes

$$P_{loss} = P_{conduction} + P_{switching}. \tag{4.9}$$

Duty cycle
The duty cycle for Boost and Totem-pole is calculated by

$$D = \frac{U_o - U_{in}}{U_o}. \tag{4.10}$$

The duty cycle for Half-bridge converter is

$$D_{Half} = \frac{U_o \times N_1}{U_{in} \times N_2} \tag{4.11}$$

and the duty cycle for Full-bridge converter is calculated as

$$D_{Full} = \frac{U_o \times N_1}{U_{in} \times N_2 \times 2} \tag{4.12}$$

where N1 and N2 are the numbers of turns on the primary and secondary side of the transformer [6].

Transistor
The conduction losses are expressed as

$$P_{conduction} = R_{DS,on} \times {I_{dc}}^2 \times D \tag{4.13}$$

where the $R_{DS,on}$ are the drain-source on-state resistance, the I_{dc} is the dc current after the rectifying diode bridge and D is the duty cycle.

The switching loss is calculated by

$$P_{switching} = 0.5 \times V_{dc} \times I_{dc} \times (t_r + t_{don} + t_f + t_{doff}) \times f_{sw} \tag{4.14}$$

where t_{don} is the delay on time and the t_{off} is the delay off time from datasheet [94].

The total loss will then become

$$P_{loss} = P_{conduction} + P_{switching}. \tag{4.15}$$

The gate drive loss and turn on loss are neglected since their values are small.

Inductor
The inductor losses are calculated according to the equation

$$P_{loss} = P_{core} + P_{DCR} + P_{ACR} \tag{4.16}$$

where the ACR is the AC resistance of the inductor and the DCR is the DC resistance of the inductor. The P_{ACR} and P_{DCR} are the wire loss caused by AC and DC resistance. The DCR value is taken from the datasheet, where the core loss and P_{ACR} are low and therefore will be neglected [157]. The Boost inductor losses are calculated based on a design guide of a Boost PFC converter [69].

The inductor current $I_{L,RMS}$ is calculated by using the CCM boundary condition

$$I_{L,RMS} \geq \frac{\Delta I}{2} \tag{4.17}$$

where the current ripple is

$$\Delta I = \frac{V_L \times D}{L \times f_{sw}}. \tag{4.18}$$

To obtain the inductor current can now be found

$$I_{L,RMS} \geq \frac{\Delta I}{2}. \tag{4.19}$$

The inductor copper loss can be calculated by using

$$P_{DCR} = P_{L,cu} = {I_{L,RMS}}^2 \times DCR. \tag{4.20}$$

Capacitor
When calculating the DC-link losses, the reactance value is first needed

$$X_c = \frac{1}{2 \times \pi \times f_{sw} \times C}. \tag{4.21}$$

Then equivalent series resistance (ESR) can be calculated

$$ESR = tan\delta \times X_c \tag{4.22}$$

where the $tan\delta$ is taken from datasheet. Now the losses can be calculated using

$$P_{loss} = {I_{co,RMS}}^2 \times ESR \tag{4.23}$$

where $I_{co,RMS}$ is the RMS output capacitance current [69].

Transformer
Inside the transformer, there are iron losses, copper losses, stray losses and dielectric losses. The copper losses consist of skin effect, proximity and frequency components. The skin effect is the current at high frequencies that is concentrated near the surface of the conductor. While the proximity effect is when the current in an conductor

influence other currents [99],[96]. At higher frequencies, the skin effect and proximity effect increases [96].

Iron losses include both eddy and hysteresis losses. Since high frequencies are used, the material that is best suited is ferrites. Ferrites are a combination of iron-oxide (Fe_2O_3) and metallic materials, such as Zinc. If ferrites are utilized, then the eddy losses are neglectable [6]. Furthermore, hysteresis losses or core loss is the consumed power from altering the direction of the BH-curve, it is dependent on the core material and the frequency used. B represents the flux density and H is the magnetic field strength. Moreover, the dielectric losses can occur in the solid insulation. When the solid insulation takes its toll on the quality or gets damaged the efficiency of the transformers gets worse. Finally, stray losses are the stray inductance that occurs when leakage field is presence. Stray inductance losses are very small compared to the major losses hysteresis, and copper, it will be neglected [98].

In the following segment, the transformer power losses equations will be presented, where most of the heat is generated are from the transformer, transistors and diodes.

The number of turns is obtained by first calculating the turns per volt that are needed

$$T_e = \frac{1}{4.44 \times f_{sw} \times B_m \times A_c}[Turns/Volt] \tag{4.24}$$

where T_e is $\frac{1}{Vind}$, V_{ind} is induced voltage. The 4.44 represents a sinusoidal waveform, A_c is the core area and the B_m is the maximum magnetic flux density [100].

Thus the number of turns in primary winding is given by

$$N_1 = T_e \times V_p \tag{4.25}$$

where V_p is the voltage in the primary winding.

The skin depth (d) is calculated in order to see how large area of the wires should be designed when considering the skin effect. The skin depth is calculated by

$$d = \frac{1}{\sqrt{\pi \times \mu_0 \times \sigma \times f_{sw}}} \tag{4.26}$$

where μ_0 is the permeability in vacuum and σ is the conductivity in copper [6].

The window area is the amount of space that the $wire_{Bundle}$ can fit inside the core. This area is calculated as

$$A_w = b_w \times h_w \tag{4.27}$$

where width b_w and height h_w are selected from the datasheet.

The maximum area that the copper wire was dimensioned for, is obtained with

$$A_{cu,max} = \frac{k_{cu} \times A_w}{N_p \times N_s} \tag{4.28}$$

where k_{cu} is the copper fill factor [6]. The copper wire area of the winding should be less than $A_{cu,max}$.

The core girth of the transformer is defined by

$$Girth = D_{core} \times \pi \tag{4.29}$$

where the diameter D_{core} is taken from datasheet.

The length of the wire was calculated as

$$L = Girth \times (N_p + N_s) \tag{4.30}$$

where L is the total wire length of the primary and secondary winding.

The size of the transformer is calculated as

$$V = l \times b \times h \tag{4.31}$$

where the transformer length, height, and width are from the datasheet. With an added I-core.

When calculating losses, the focus is on the major losses of the transformer, located in the winding and the core. There are other losses as well, however, they are significantly lower in this case, that they are neglected. The losses are calculated by

$$P_{loss} = P_w + P_{core} \tag{4.32}$$

To calculate the winding losses P_w, the wire resistance is needed

$$R_{wire} = \frac{\rho_{cu} \times L}{A_{cu,bundle}} \tag{4.33}$$

where ρ_{cu} is the electrical resistivity of copper, L is the total wire length and the copper wire area of the bundle.

While the R_{dc} can be known from the expression as follows

$$R_{dc} = (MTL) \times N \times R_{wire} = girth \times N \times R_{wire} \tag{4.34}$$

where MTL is the mean turn length, which is assumed to be close to girth value [101]. N is both N_1 and N_2 together.

With R_{dc} known, the winding loss can be calculated

$$P_w = R_{dc} \times I_{RMS}^2 \tag{4.35}$$

where I_{RMS} is $\frac{I}{\sqrt{3}}$ because of the triangular waveform [102].

To calculate the magnetic loss density P_M, Steinmetz equation is implemented as

$$P_M = k \times f^a \times B_{peak}^d \tag{4.36}$$

where k, a and d are constants depending on what type of core material and frequency is used [98]. In the selected core, there is Ferrite material 3F3, thus the constants are $k = 2.5 \times 10^{-4}$, a=1.63, d=2.45 [6], [103], [104].

The volume of the core is calculated from and the values found in the datasheet [98]. Giving the volume

$$V_{core} = A_{core} \times Height. \tag{4.37}$$

The core losses can be calculated by

$$P_{core} = P_M \times V_{core} \tag{4.38}$$

which give the total losses

$$P_{loss} = P_w + P_{core}. \tag{4.39}$$

The efficiency is known as the standard equation

$$\eta = \frac{P_{out}}{P_{in}} \tag{4.40}$$

where the power input was calculated as

$$P_{out} = P_{in} - P_{loss}. \tag{4.41}$$

Hence the new efficiency of the transformer is

$$\eta = \frac{P_{in} - P_{loss}}{P_{in}}. \tag{4.42}$$

Microcontroller unit

The logic board consists of an LV board and DSP board, where the microcontroller unit (MCU) SPC560B54L3B4E0 is located on the LV-board. This controller is expected to generate highest losses in the low voltage system. Due to lack of information, the losses from the MCU needs to be estimated. The power dissipation for each pin can be roughly calculated with the equation follows as

$$P_{loss} = V^2 \times f_{sw} \times C_{load} \tag{4.43}$$

where it is known from data sheet that f_{sw} = 279-285 kHz, supply voltage of V=5V and C_{load}= 3.8-5 pF [37], [105]. To obtain the complete losses of the MCU, a scaling factor is needed. This factor is assumed to be 2 for interconnection for pins [106].

This factor is multiplied with the losses for one pin, thus gives the total losses of the MCU [107]. The power losses for this controller is assumed to be the same for the controller in the off-board charger.

4.9.2 Thermal calculation and design

When the total amount of losses in the circuit is known, the thermal resistance value can be calculated

$$R_{th,ja} = \frac{T_j - T_a}{P_{tot}} \tag{4.44}$$

where T_j is the maximum permissible operating temperature of the components according to their datasheets, P_{tot} is the total power dissipation and T_a is the highest assumed ambient temperature [6].

Since it is vital to analyze the temperature level of the components, it is desired to calculate the thermal resistance of a heatsink to ensure the temperature level is in a safe range. The total thermal resistance from the junction to ambient is presented as

$$R_{th,ja} = R_{th,jc} + R_{th,cs} + R_{th,sa} \tag{4.45}$$

where the R values are representing the thermal resistance between the junction and the case, the case and the sink, the sink and the ambient temperature, and all together they make the thermal resistance between the junction and the ambient temperature. These thermal parameters can be represented as a thermal model of a heatsink shown in Figure 4.20 [6].

With the thermal resistance values from all the components separately are added together in parallel, to get one thermal resistance value as

$$\frac{1}{R_{th,sa,tot}} = \frac{1}{R_{th,sa,1}} + \frac{1}{R_{th,sa,2}} + ... + \frac{1}{R_{th,sa,n}}. \tag{4.46}$$

In order to obtain the dimensions of a heatsink, the $R_{th,sa}$ value needs to be known. The lower the $R_{th,sa}$ value is, the larger heatsink will be required.

In order to calculate the operating temperature for a transformer, an estimation formula is used,

$$\Delta T = (\frac{P_{loss}}{A})^{0.833} \tag{4.47}$$

where the value 0.833 has been derived from empirical data [108].

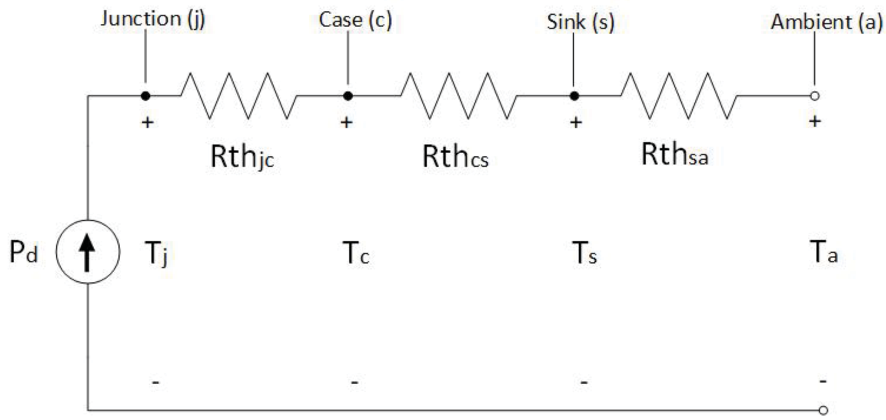

Figure 4.20: Thermal resistance of a heatsink model [39].

5
Results

In this section, the dissembling procedure of the OBC is presented. Necessary analyzes and measurements were conducted as well. This procedure aids to acquire deeper knowledge about the OBC and to give a better idea of how the off-board charger should be designed. A final topology is selected based on size, weight, electrical performance and power losses according to the design specification. These parameters were obtained by simulation and calculations.

5.1 OBC - disassembling

From the dissembling process, it was first noticed that under the front aluminum casing there is a plastic safety shield to protect the power electronics from impacts. This shield is sealed with epoxy (silicon material) to protect the OBC from a contaminated environment. Under this shield, the circuit board could be observed in Figure 5.1 to the left. Underneath the circuit board were yellow thermal interface material (TIM) implemented to the main shell. The material is used to increase the thermal connection between the cooling system and the heat loads. Thus, dissipate thermal heat generated from the components are removed more efficiently. This is presented in Figure 5.1 to the right.

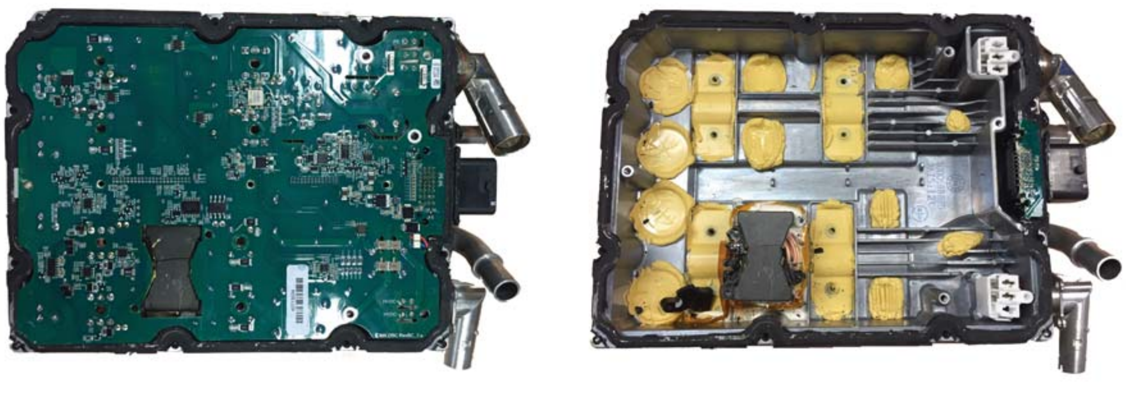

Figure 5.1: To the left: under the plastic safety shield the circuit board over the low voltage system is seen inside the OBC. To the right: the base of the OBC casing, where the cooling system is located, are mounted with TIM to dissipate thermal heat generated from the components.

On the back side of the circuit board, the high voltage system with its power electronic components is mounted. This is where the power conversion from AC to DC is processed. In Figure 5.2, the internal components organization is presented.

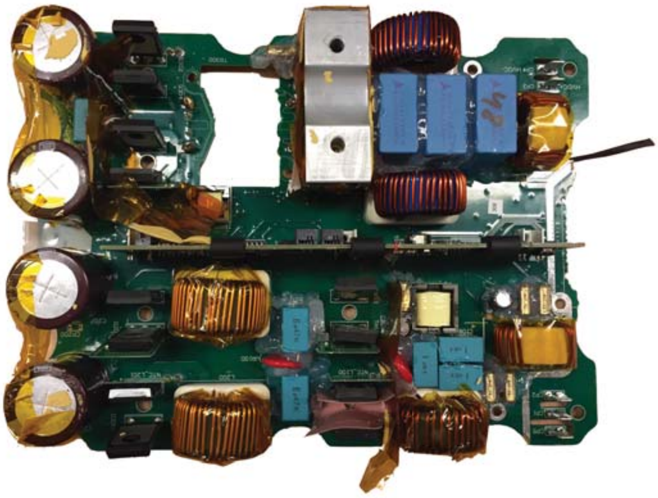

Figure 5.2: Back side of circuit board, where the high voltage system and its power electronic components are implemented.

5.1.1 Layout of components

After the dissembling sequence, it was time to identify what components are included in this OBC. From the theory background chapter, it was quickly concluded that an OBC consist of two stages: one AC/DC converter with PFC circuit, and one DC/DC converter. These stages are marked in Figure 5.3, including the flow of the incoming AC and supplying DC, is located on the power board.

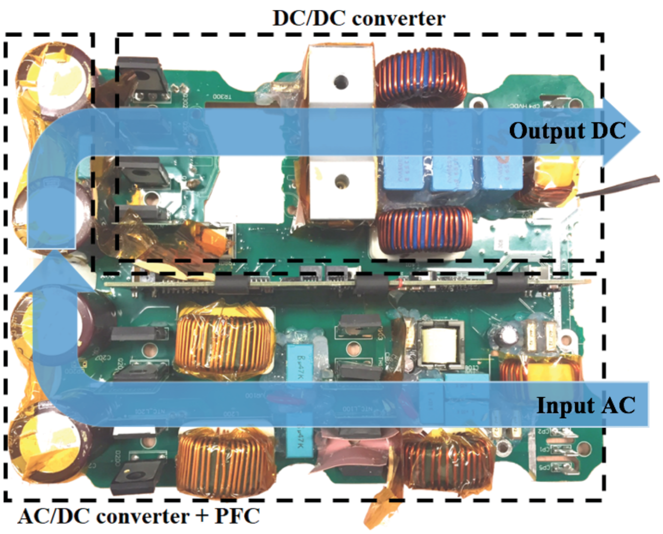

Figure 5.3: Layout overview of the OBC, where an AC/DC converter with PFC circuit, and a DC/DC converter are included. The flow of the incoming AC and supplying DC are illustrated with blue arrows.

Further, through this flow, the high voltage system can be divided into 15 segments, where the incoming grid AC voltage is converted through all these segments into a DC voltage. These key segments are identified on the board as followings: an AC connector, fuses, filters, first rectifier, PFC circuit, DC-link, full-bridge, transformer, second rectifier, filters and DC connector. There are four heatsinks to thermally protect certain components, by the help of a cooling pipe that is placed outside the casing. Each heatsink is provided with rectangular shaped fins to distribute the cooling temperature easier. The heatsinks are arranged on the top of the MOSFETs, transistors and diodes. This configuration is shown in Figure 5.4.

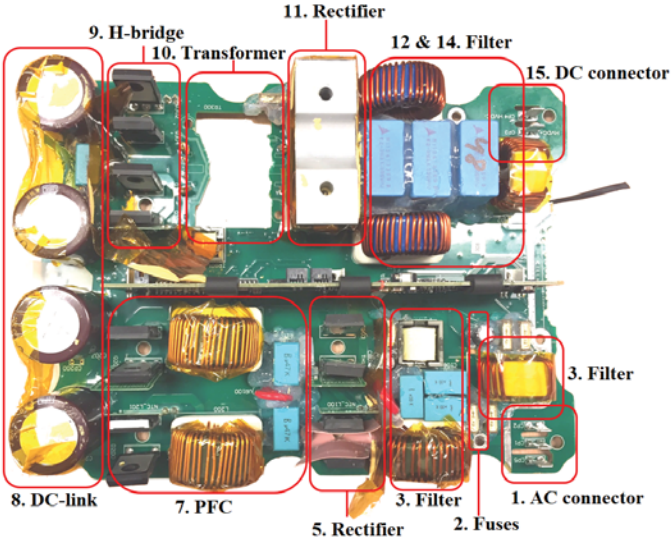

Figure 5.4: Identification of the segments that are included in the high voltage system.

A detailed description about each segment is presented in the list as follows [37]:

1. **AC power connector** - EVI in the OBC receives power (230V AC, 16 A) from the AC grid through the AC power connector.
2. **Fuses** - Electrical devices to protect electrical equipment against abrupt overcurrents (max. 20 A) occurring in the system by break the flowing current.
3. **EMI filter and transient protection** - Filter that is required to conceal interference that occurring in power line. See subsection 4.3.3 for more information.
4. **Passive discharge circuit** - Is an implementation method to discharge a circuit for vehicles, and ensure mitigate losses.
5. **1st diode rectifier** - Electrical setup of silicon controlled diodes ensure the current flowing in one direction, where AC current converts to DC current. The rectifier receives in the input: 85-264 V_{RMS}, max 16 A, 45-65 Hz.
6. **EMI filter/suppressor** - See number 3. EMI filter.
7. **PFC, 2-channel** - An interleaved PFC circuit that ensures that power is maintaining a high quality, by keeping low losses and high efficiency. This PFC delivers between 400-420 V, with 420 V and 12 A as the maximum values.

The switching frequency for the PFC circuit is 98.3 kHz.

8. **Capacitor Bank (DC-link)** - A set of several capacitors connected in parallel to store energy and mitigate phase shift between voltage and current. See subsection 4.2.3 for more information.
9. **Phase shifted full bridge** - Part of the DC/DC converter with high power operation, that ensure high efficiency, transparent control and minimized in size. It receives the voltage and current from the AC/DC converter stage. The switching elements are having a frequency of 98.3 kHz.
10. **Transformer** - Electrical device that transfer the voltage and current into different voltage levels. The windings of the transformer are equipped with Litz wire to create higher isolation, reduce skin effect and eddy currents. This transformer is the second part of DC/DC converter.
11. **2nd diode rectifier** - The last part of the DC/DC converter. See number 5. diode rectifier for more information.
12. **LC filter (resonant circuit)** - These types of filters are commonly implemented into passive EMI filters, where they either are designed as low pass filter (LPF), high pass filter (HPF) or BPF (band pass filter) depending on application [109].
13. **Passive discharge circuit** - See number 4. passive discharge circuit.
14. **CM filter** - These filters ensure to mitigate noises from the capacitors with parasitic elements. This removes the last voltage ripple to ensure that smooth and pure DC is supplied to batteries. - See subsection 4.3.3 for more information.
15. **HVDC connector** - EVI in the OBC delivers DC power (200-410 V DC, max 420 V and 8 A) through the HVDC connector.

5.1.2 Component characteristics

Measurements were conducted to obtain data of the components. Some components inside the OBC, like inductors and transformers, were missing model numbers and component values. Hence, those components were removed from the circuit board and measured to get their values. The component list is shown in Appendix B.

Four inductors and one transformer were de-soldered from the OBC's circuit board. A Fluke multimeter (8808A) was used to quickly find out which legs of the inductors were in pairs. Additionally, an Automatic Precision Bridge (B905) were used to obtain the approximate values of the inductors.

In relation to the weight and volume, the largest components, from the high voltage system from the OBC were identified to be the transformers, inductors, and capacitors. These components have been measured by checking their dimension and weight. For the weight measurements of the power electronic components, an Ohaus AX324 Adventurer Analytical Balance was used as a weight scale. For the larger parts, a Jadever Weighing Scale JWE-15K 15kg was utilized. Since there was a lack of information about serial numbers and name of the components, they have been denoted with suitable names. In Table 5.1, the component name, component value, dimension, volume, and weight are presented as following:

Table 5.1: Volume and weight of the power electronic components.

Component	Value	Amount	Dimension (H x W x L) [cm]	Volume [cm^3]	Weight [g]
Toroid Coil (12, 14)	7.2 μH	2	4 x 2.3 x 4	28.9	77.91
Toroid Coil (7)	388 μH	2	4 x 2.7 x 3.8	30.6	105.4
Toroid Coil/small trafo (3)	3.68 mH	1	2.9 x 2 x 3.4	18.2	38.35
Toroid Coil (3)	188 μH	1	4 x 2.3 x 4	28.9	77.67
Capacitor (12, 14)	3.3 μF	3	3.2 x 1.6 x 3.1	15.9	18.35
Capacitor (7)	47 μK	5	1.9 x 1.1 x 1.8	3.8	4.73
Capacitor (8)	270 μF	4	3 x 3.2	22.6	32.97
Transformer (near 9, 10)	N/A	1	1.2 x 1.5 x 1.5	2.7	3.77
Transformer (3)	N/A	1	1 x 2 x 2	4.0	5.59
Transformer (11)	N/A	1	4 x 4.5 x 6	108	850.39
Switch (5,7,9,11)	N/A	8	1.5 x 2 x 0.5	4.7	1.5
Diode (5,7,9,11)	N/A	8	1.5 x 2 x 0.5	4.7	1.5

In Table 5.1 there are numbers next to the components name which refers to their location on the circuit board that can be seen in Figure 5.4.
The number of components gave the total volume and weight presented in Table 5.2.

Table 5.2: Total weight and volume for the power electronic components.

Component	Value	Amount	Total volume [cm^3]	Total weight [g]
Toroid Coil (12, 14)	7.2 μH	2	57.8	155.82
Toroid Coil (7)	388 μH	2	61.2	210.8
Toroid Coil/small trafo (3)	3.68 mH	1	18.2	38.35
Toroid Coil (3)	188 μH	1	28.9	77.67
Capacitor (12, 14)	3.3 μF	3	47.6	55.05
Capacitor (7)	47 μK	5	18.8	23.65
Capacitor (8)	270 μF	4	90.5	131.16
Transformer (near 9, 10)	N/A	1	2.7	3.77
Transformer (3)	N/A	1	4.0	5.59
Transformer (11)	N/A	1	108.0	850.39
Switch (5,7,9,11)	N/A	8	37.6	12
Diode (5,7,9,11)	N/A	8	37.6	12
Total:			428.5	1576.4

As it can be observed from the table, the total volume and weight is 428.5 cm^3 respectively 1576.4 g for the power electronic components that are included in the OBC.
A summary of other parts that are equipped in the OBC is shown in Table 5.3.

Table 5.3: Other weight of the OBC.

Other parts	Weight [g]
Metallic casing + plastic safety shield	2046.5
Cooling system of OBC	893.11
Plastic safety shield	144
Metal-box (with circuit)	3580
OBC circuit board	1196

It is identified that these largest electric power components that take most weight and volume are located in following sections: AC/DC- and DC/DC converters, filters, PFC circuit and the DC-link.

5.2 Charging cable - disassembling

The module of charging cable for mode 2 charging for EVs from Mennekes, was dissembled as well to get an overview of what components are included and how they are organized inside. In Figure 5.5 to the left, the plastic safety shield is removed to observe the high voltage components that are included. In the same figure to the right, the base of the plastic cover from the module is shown.

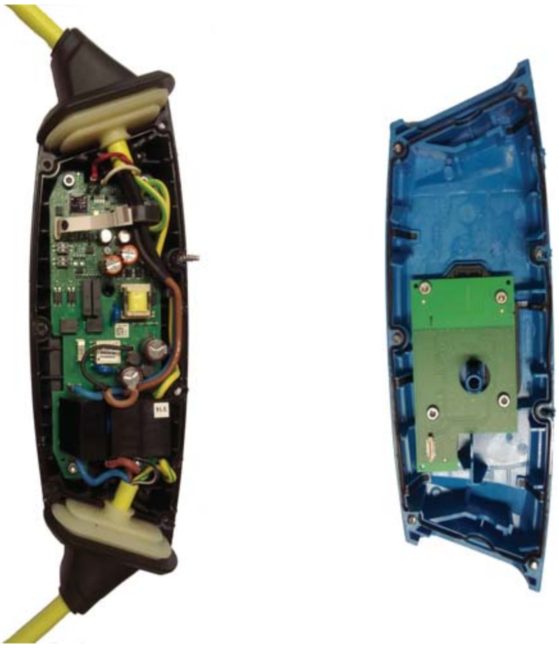

Figure 5.5: To the left: under the plastic safety shield the circuit board over the high voltage system is observed inside the module of the charging cable. To the right: the base of the module's plastic casing is shown.

After the dissembling process, it could be identified that the largest components are three relays located at the output of the module. These relays are controlling the supplying current to the grid. However, in order to save as much space as possible for the electric power components to fit properly inside the module of the off-board charger, no components inside the Mennekes' module are required. The total weight of the cable is 1.97 kg, without the module, and the internal weight of the circuit board is 0.330 kg. By removing the internal content, gave approximately 1.64 kg with cable together with the desolate module. These weights are listed in Table 5.4. The module itself has a volume of 1320 cm^3. This weight and volume needed to be included when finalizing the off-board charger.

Table 5.4: Other weight of the charging cable.

Other parts	Weight [g]
Cable (with circuit, without module)	1597.5
Sealed module on cable (without cable)	357.5
Circuit-board in charging cable	330

5.3 Off-board charger - design characteristics

5.3.1 Design requirements

In order to make the off-board charger more compact, the components need to be reduced in size. By scaling down the requirements of this charger, it is feasible to obtain a small-sized design. In Table 5.5, the desired target design specification of the off-board charger is shown.

Table 5.5: Target design specification of off-board charger.

Specification	Values	Units
AC input voltage (RMS)	230	Vac
AC input frequency	50	Hz
AC input current	approx. 4-8 (max. 10)	A
DC output voltage range	320-380	Vdc
DC current output	≤ 4	A
DC power output range	900-1700	W
PFC - Switching frequency	150	kHz
DC/DC - Switching frequency	200	kHz
THD	≤ 8	%
Target efficiency	≥ 92	%
Target PF	≥ 0.9	-
Power density	≤ 1	kW/kg
Dimension (H x W x L)	5.2 x 24.0 x 10.	cm
Weight	≤ 2	kg
Ingress protection	IP67 and IP6K9K	-

5.3.2 Components selection

To determine the components values of the selected AC/DC- and DC/DC converter, the following steps are executed accordingly to standard calculations [110], [34]. The components for the EMI filters are also determined by standard equations [49]. Standard values are selected accordingly to datasheets to determine the size and to select proper components in the simulation part. The calculations and selection of components are based on a power output between 900 to 1700 W, for 3 different current inputs 4 A, 6 A and 8 A. This is accordance to Table 5.5.

5.3.2.1 AC/DC converter with Boost PFC

According to the design specification, the efficiency η is assumed to be the minimum as in the OBC, 92 %. With an output power of 900 W, gave the input power to

$$P_{in} = \frac{P_{out}}{\eta} = \frac{900}{0.92} = 978.26W \tag{5.1}$$

where P_{in} is the input power supplied to the converter and P_{out} is the output power. Since the input power is calculated and the input RMS voltage from the grid is known, the input current was estimated to

$$I_{in(RMS)} = \frac{P_{in}}{V_{in(RMS)}} = \frac{978.26}{230} = 4.25A. \tag{5.2}$$

This input current is roughly 4 A. The peak input current is obtained by

$$I_{in(p)} = \sqrt{2} \times 4.25 = 6.02A. \tag{5.3}$$

Finally, the average input current is estimated

$$I_{in(avg)} = \frac{2 \times I_{in(p)}}{\pi} = \frac{2 \times 6.02}{\pi} = 3.83A. \tag{5.4}$$

Rectifier diodes
To design a protective diode to the rectifier bridge that can withstand the highest supplied voltage, which is 230 V (RMS) from the grid, gave the peak current as

$$V_{in(p)} = \sqrt{2} \times V_{in(RMS)} = \sqrt{2} \times 230 = 325.27V. \tag{5.5}$$

To calculate the current through the diode, the inductor current ripple must be estimated. It has a current ripple factor RF_I typically between 10-20 %. To obtain a more protective design for the diode, the current ripple factor is assumed to be 20 %, expressed as

$$\Delta I_L = RF_I \times I_{in(p)} = 0.2 \times 6.02 = 1.20A. \tag{5.6}$$

Since the same current flows through the diode and inductor, the peak inductor current is equal to the peak diode current

$$I_{diode(p)} = I_{L(p)} = I_{in(p)} + \frac{\Delta I_L}{2} = 5.89 + \frac{1.20}{2} = 6.49A. \tag{5.7}$$

From earlier calculations is concluded that the rectifier diode needs to conduct an average current of $I_{in(avg)} = 3.83$ A.

Boost inductor
Since earlier calculations, it is known that the peak input voltage is $V_{in(p)} = 325.27V$. This value was utilized to calculate the duty cycle of the peak Boost transistor, where V_{out} is set to be 400 V, expressed as

$$D_{boost(p)} = 1 - \frac{V_{in(p)}}{V_{out}} = 1 - \frac{325.27}{400} = 0.19. \tag{5.8}$$

With the selected switching frequency of 150 kHz, gave the calculated value of the inductor as

$$L_{boost} = \frac{V_{in(p)} \times D_{boost(p)}}{f_{sw} \times \Delta I_L} = \frac{325.27 \times 0.19}{150e^3 \times 1.20} = 343.34\mu H. \tag{5.9}$$

A standard value 330 μH inductor manufactured by Bourns was selected. It provides a tolerance of 15 % and can withstand a temperature of 125 °C [111].

Transistor
Since a switching frequency of 150 kHz is selected, it was desirable to have a MOSFET selected, in contrast to a IGBT. The MOSFET needs to handle an output voltage of 400 V including its ripple. In this case, the voltage ripple factor was selected to be 6 % since it is average value and to reduce the size of the output capacitor. The output voltage with voltage ripple is expressed as

$$\Delta V = RF_V \times V_{out} = 0.06 \times 400 = 24V. \tag{5.10}$$

This suggested to select a MOSFET that is able to operate for a voltage for at least 424 V and a conducting peak current of 6.02 A. By select a MOSFET STF10N60DM2 manufactured by IXYS, having the properties 600 V and 8 A, a safety margin could be established [112].

Boost diode
From previous calculations, it was determined that the conducting average current through the diode is 3.83 A. This suggested to select Schottky diode 869-QH08BZ600 from Power Integrations that is having a forward current of 8 A and a reversed voltage of 600 V. Since the diode is made of silicon carbide material, it can withstand higher frequency [113].

Output capacitor
The output capacitor of the converter was estimated accordingly to

$$C_{min} \geq \frac{\frac{P_{out}}{V_{out}}}{2\pi \times f_r \times RF_V \times \Delta V} = \frac{\frac{900}{400}}{2\pi \times 100 \times 24} = 149.21\mu F \tag{5.11}$$

where $\Delta V = 24V$ and the rectifying frequency is denoted as f_r=100 Hz to obtain the minimum capacitor value that is required at a higher frequency. Since earlier, the voltage ripple factor was selected to be 6 %. Since it is an average value, a margin of 25% incresasing of the capacitance is added to obtain the actual value.

$$C_{out} = 25\% \times C_{min} = 1.25 \times 149.21 = 186.51\mu F \tag{5.12}$$

Since it was favorable to have several capacitors for the capacitor bank, it was assumed that the bank also consists of 4 capacitors as the OBC. Thus, it gave 4 x 47 μF capacitors to obtain 186 μF. The selected component was an electrolytic aluminum capacitor from United Chemi-con with 20 % tolerance and maximum temperature of 105°C [114]. The maximum hold-up time for the capacitor was calculated according to the expression

$$T_{hold-up} = \frac{1}{4 \times 2 \times f_{LL}} = \frac{1}{4 \times 2 \times 50} = 2.5ms \tag{5.13}$$

where the f_{LL} is the line frequency of 50 Hz. This gave the extended operation time to be 2.5 ms that the converter would run after the power would be interrupted [34].

5.3.2.2 AC/DC converter with Totem-pole PFC

Totem inductor

To calculate the value of the inductance, the values were set accordingly to the design specification for a current of 4 A. The current ripple factor and switching frequency was selected to be 20 % respectively 150 kHz for this converter as well.

$$L = \frac{D(1-D) \times V_{out} \times V_{in}}{\Delta I_L \times \sqrt{2} \times P_{out} \times f_{sw}} = \frac{0.19(1-0.19) \times 400 \times 230}{0.2 \times \sqrt{2} \times 900 \times 150e^3} = 370.8\mu H \tag{5.14}$$

where both the duty cycle and voltage ripple were assumed to be the same as earlier calculations [115].

Rectifier diodes and transistor

Assumed to be the same selection as for the Boost PFC, since the rectifier diodes and transistor operating for the same average input currents and peak currents.

Output capacitor

The output capacitance for the capacitor bank was selected with the presented expression

$$C_{out} \geq \frac{P_{out} \times \pi \times f_{LL} \times \Delta V}{{V_{out}}^4} = \frac{900 \times 50 \times 24}{400^4} = 132.53\mu F \tag{5.15}$$

where voltage ripple was assumed to be same as $\Delta V = 24$ V based on earlier calculations [68]. Likewise, the Boost PFC it was assumed that four capacitors were needed for the capacitor bank, which gave 4 x 33 μF capacitors to obtain 132 μF. The hold-up time of 2.5 ms for this capacitor was assumed to be the same as for the Boost PFC converter.

5.3.2.3 Full and Half-bridge DC/DC converter

For the design of the Full-bridge DC/DC converter, it was vital to design the transformer properly since it was expected to be the largest component inside the off-board charger and generating the majority of the power losses. For the Half-bridge, only 2 MOSFETs were considered in the primary bridge [34]. This DC/DC converter was selected to have a switching frequency of 200 kHz according to the design specification.

Transformer
A transformer material was selected to be 3F3 since it is used for 40-420 kHz [6]. Also, a transformer core was chosen as ETD49/25/16-3F3. This transformer core has an area of 211 mm^2 and a core diameter of 16.39 mm. ETD core includes a round core, which means that the winding resistance will decrease. The transformer and its core are shown in Figure 5.6.

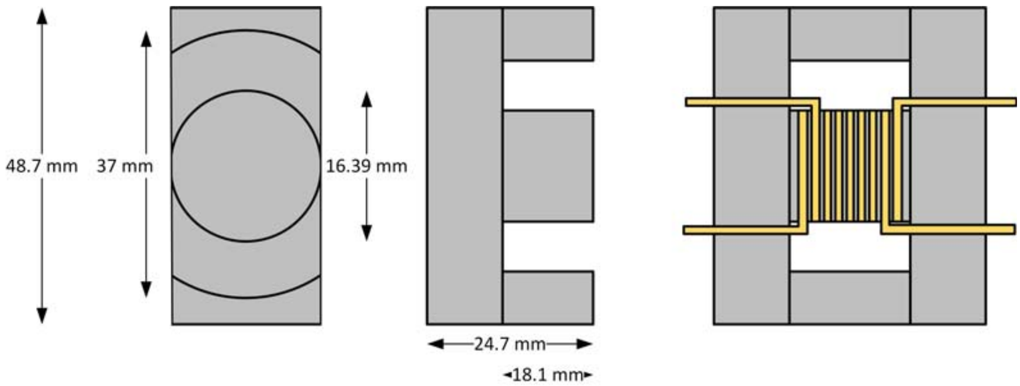

Figure 5.6: Dimension of the selected transformer and its core.

Output inductor
By simulation test, the output inductor of the DC/DC converter was estimated to be 0.25 μH, with a transformer ratio 14:14.

Transistors and output rectifiers
For the switches in the primary bridge side, a 600 V MOSFET operating for higher frequency and have a doubled withstand current input. For the diodes at the secondary bridge side, since 2.25 A is conducting in the DC/DC converter stage, a current rate of 3 A silicon carbide diodes were selected [116].

Output capacitor
Since 400 V is expected at the output of the converter after the secondary diode bridge, a 33 μF 400 V electrolytic capacitor is selected [34].

5.3.2.4 EMI filters

For the design of the EMI filter, it was known from before that 230 V (RMS) and 50 Hz is supplied to the charger [49]. Since it desired that the output voltage should be 400 V, the maximum load current was calculated according to

$$I_{out(max)} = \frac{P_{out}}{V_{PFCout}} = \frac{900}{400} = 2.25A \tag{5.16}$$

where the expected P_{out} to be 900 W and V_{PFCout} is 400 V [34]. This gave that the load current to be 2.25 A to obtain an output power of 900 W. This gave the impedance as

$$Z = \frac{V_{in(RMS)}}{I_{out(max)}} = \frac{230}{2.25} = 102.22\Omega. \tag{5.17}$$

Inductor and capacitor
To ensure that a margin was established for a minimal suppression, the cut-off frequency was assumed to be at least 10 times larger than the line frequency f_{LL}=50 Hz. This gave the cut-off frequency to be f_{cut}= 500 Hz. This frequency was used to calculate the final components of the filter. The inductor was calculated as

$$L_{EMI} = \frac{Z}{2\pi \times f_{cut}} = \frac{102.22}{2\pi \times 500} = 32.5mH. \tag{5.18}$$

For the capacitor, it is expressed and calculated as

$$C_{EMI} = \frac{1}{2\pi \times f_{cut} \times Z} = \frac{1}{2\pi \times 500 \times 76.66} = 3.11\mu F. \tag{5.19}$$

For the type of EMI filter, a basic π-filter was selected. To obtain the inductance and capacitor value, L_{EMI} and C_{EMI} are needed to be divided by 2. This design required 2 capacitors and 2 inductors [49].

5.3.3 Weight and size

It was vital to reduce the components in terms of size and weight, especially the largest components which were identified to be the Boost inductor, output capacitor, and filters components. Their volume was determined using basic geometrical figures. The Boost inductor and output capacitor are having the shape of a cylinder, while filter capacitor, MOSFET, and diode are based on a rectangular box.

Since certain datasheets could not provide sufficient information of certain components, their weight was estimated through an online conversion tool based on their dimension and material [117].

AC/DC converter with Boost PFC
Standard components were selected for 4 A, 6 A respectively 8 A supplied to AC/DC converter with Boost PFC [118]-[126]. Their dimension, volume and weight are summarized in Table 5.6 listed as

Table 5.6: With various current ratings supplied to the AC/DC converter Boost PFC, gives different component value, volume and weight.

Current rate	**Component**	**Standard value**	**Dimension (D x (W) x H) [cm]**	**Volume** [cm^3]	**Weight [g]**
4 A	Rectifier diode	600 V/ 4 A	1.57 x 0.46 x 1.04	0.75	6
	L_{boost}	330 μH	2.79 x 1.40	8.56	24.15
	MOSFET	600 V/ 8 A	1.04 x 0.46 x 1.64	0.78	2
	Boost diode	600 V/ 9 A	1.067 x 0.47 x 0.9	0.45	2
6 A	Rectifier diode	600 V/ 6 A	1.57 x 0.46 x 1.04	0.75	6
	L_{boost}	220 μH	3.25 x 1.65	13.69	32.35
	MOSFET	600 V/ 10 A	1.04 x 0.46 x 1.64	0.78	2
	Boost diode	600 V/ 10 A	1.02 x 0.45 x 1.59	0.73	6
8 A	Rectifier diode	600 V/ 8 A	1.59 x 0.45 x 1.02	0.73	6
	L_{boost}	150 μH	3.25 x 1.65	13.69	47.05
	MOSFET	600 V/ 13 A	1.04 x 0.45 x 1.6	0.75	2.27
	Boost diode	600 V/ 12 A	1.067 x 0.47 x 1.65	0.83	6

The output capacitors of the DC-link is presented in Table 5.7 for various currents ratings. These have been selected accordingly to standard values [114], [127], [128].

Table 5.7: Output capacitor for the AC/DC converter with Boost PFC.

Current rate	**Component**	**Standard value**	**Dimension (D x H)** [cm]	**Volume** [cm^3]	**Weight [g]**
4 A	C_{out}	47 μF	1.8 x 1.5	3.82	10.306
6 A	C_{out}	68 μF	2.0 x 2.5	7.85	12.30
8 A	C_{out}	100 μF	1.8 x 4.0	10.18	15.40

It should be noted that these values are for one capacitor and that the DC-link consist of four capacitors to give the total capacitance for the bank. The total capacitance for the DC-link is shown in Table B.6 in Appendix B.

AC/DC converter with Totem-pole PFC

Standard components were selected for 4 A, 6 A respectively 8 A supplied to AC/DC converter with Totem-pole PFC [129]-[131]. The rectifier diodes in the bridge and the transistors were assumed to be the same as in the Boost PFC. Their dimension, volume and weight are summarized in Table 5.8 listed as

Table 5.8: With various current ratings supplied to the AC/DC converter Totem-pole PFC, gives different component value, volume and weight

Current rate	Component	Standard value	Dimension (D x (W) x H) [cm]	Volume [cm^3]	Weight [g]
4 A	Rectifier diode	600 V/ 4 A	1.57 x 0.46 x 1.04	0.75	6
	L_{totem}	390 μH	2.41 x 1.39	6.34	18.23
	MOSFET	600 V/ 8 A	1.04 x 0.46 x 1.64	0.78	2
6 A	Rectifier diode	600 V/ 6 A	1.57 x 0.46 x 1.04	0.75	6
	L_{totem}	270 μH	3.25 x 1.65	13.69	32.16
	MOSFET	600 V/ 10 A	1.04 x 0.46 x 1.64	0.78	2
8 A	Rectifier diode	600 V/ 8 A	1.59 x 0.45 x 1.02	0.73	6
	L_{totem}	180 μH	2.79 x 2.54	15.53	49.0
	MOSFET	600 V/ 13 A	1.04 x 0.45 x 1.6	0.75	2.27

For one output capacitor at the capacitor bank is presented in Table 5.9 for various currents ratings. These are selected accordingly to standard values.

Table 5.9: Output capacitor for the AC/DC converter with Totem-pole PFC.

Current rate	Component	Standard value	Dimension (D x H) [cm]	Volume [cm^3]	Weight [g]
4 A	C_{out}	33 μF	1.6 x 2.0	4.021	6
6 A	C_{out}	47 μF	1.8 x 2.5	6.36	17.17
8 A	C_{out}	100 μF	1.8 x 4.0	10.18	15.40

It should be noted that these values are for one capacitor and that the DC-link consist of four capacitors to give the total calculated capacitance value for the bank [132]-[134]. The total capacitance for the DC-link is also shown in Table B.6 in Appendix B.

EMI filters

Standard components were selected for the EMI filter for 4 A, 6 A respectively 8 A [135]-[139]. The inductors and capacitors values are presented in Table 5.10 and Table 5.11.

Table 5.10: Various current ratings supplied to the EMF filter, gives different component value, volume and weight for the inductor.

Current rate	Component	Standard value	Dimension (D x H) [cm]	Volume [cm^3]	Weight [g]
4 A	L_{EMI}	18 mH	1.32 x 1.28 x 0.62	1.023	5
6 A	L_{EMI}	10 mH	1.27 x 1.27 x 0.85	1.371	4.250
8 A	L_{EMI}	6.2 mH	0.8 x 0.8 x 0.45	0.288	2.250

Table 5.11: Various current ratings supplied to the EMF filter, gives different component value, volume and weight for the filter capacitor.

Current rate	Component	Standard value	Dimension (H x W x L) [cm]	Volume [cm^3]	Weight [g]
4 A	C_{EMI}	2.2 μF	2.65 x 1.45 x 2.95	11.33	5
6 A	C_{EMI}	3.3 μF	2.65 x 1.45 x 2.95	11.33	5
8 A	C_{EMI}	3.3 μF	2.65 x 1.45 x 2.95	11.33	5

It should be noted that one EMI filter consists of 2 inductors and 2 capacitors.

Full-bridge and Half-bridge DC/DC converter
The input voltage is set to be maximum 400 V, with an input current level between 2-8 A feed to the DC/DC converter. Under ideal conditions when 400 V is fed to the converter, gave the standard components selection where component value, volume, and weight [140]-[149]. The components selection for the DC/DC full-bridge converter are presented in Table 5.12.

Table 5.12: Weight and volume of the components that are included in the full-bridge DC/DC converter.

Current rate	Component	Standard value	Dimension (D x (W) x H) [cm]	Volume [cm^3]	Weight [g]
4 A	Transformer	14:14	4.87 x 3.13 x 1.64	25	74.9
	L_{out}	6.2μH	0.8 x 0.8 x 0.45	0.288	2.25
	MOSFET	600 V/ 4 A	1.03 x 0.48 x 1.54	0.76	2
	Rectifier diode	600 V/ 3 A	1.036 x 0.49 x 1.61	0.82	2.56
	C_{out}	33μF	1.6 x 2.5	5.03	7.38
6 A	Transformer	14:14	4.87 x 3.13 x 1.64	25	74.9
	L_{out}	4.3μH	1.05 x 1.05 x 0.5	0.55	1.800
	MOSFET	600 V/ 6 A	1.13 x 0.49 x 1.63	0.90	2
	Rectifier diode	600 V/ 4 A	1.02 x 0.45 x 1.59	0.73	6
	C_{out}	33μF	1.6 x 2.5	5.03	7.38
8 A	Transformer	14:14	4.87 x 3.13 x 1.64	25	74.9
	L_{out}	3.3μH	0.52 x 0.57 x 0.28	0.0.83	0.604
	MOSFET	600 V/ 8 A	1.04 x 0.46 x 1.64	0.78	2
	Rectifier diode	600 V/ 5 A	1.02 x 0.45 x 1.59	0.73	6
	C_{out}	33μF	1.6 x 2.5	5.03	7.38

The components MOSFET, diodes and output capacitors that are used in Full-bridge were selected to be the same for the Half-bridge. This is assumed since they have similar structure and operating under the same conditions. Two capacitors were connected in parallel with the transistors [150], [151]. Likewise, Full-bridge, the components selected for the Half-bridge DC/DC converter was selected under ideal conditions, shown in 5.13.

Table 5.13: Weight and volume of the components that are included in the Half-bridge DC/DC converter.

Current rate	Component	Standard value	Dimension (D x (W) x H) [cm]	Volume [cm^3]	Weight [g]
4 A	Transformer	7:14	4.87 x 3.13 x 1.64	25	74.9
	L_{out}	6.2μH	0.8 x 0.8 x 0.45	0.288	2.25
	C_{in}	47μF	1.6 x 1.45	2.91	10
	MOSFET	600 V / 4 A	1.03 x 0.48 x 1.54	0.76	2
	Rectifier diode	600 V/ 3 A	1.036 x 0.49 x 1.61	0.82	2.56
	C_{out}	33μF	1.6 x 2.5	5.03	7.38
6 A	Transformer	7:14	4.87 x 3.13 x 1.64	25	74.9
	L_{out}	3.3μH	0.52 x 0.57 x 0.28	0.083	0.604
	C_{in}	47μF	1.6 x 1.45	2.91	10
	MOSFET	600 V / 6 A	1.13 x 0.49 x 1.63	0.90	2
	Rectifier diode	600 V/ 4 A	1.02 x 0.45 x 1.59	0.73	6
	C_{out}	33μF	1.6 x 2.5	5.03	7.38
8 A	Transformer	7:14	4.87 x 3.13 x 1.64	25	74.9
	L_{out}	2.7μH	0.2 x 0.25 x 0.16	0.08	0.032
	C_{in}	47 μF	1.6 x 1.45	2.91	10
	MOSFET	600 V/ 8 A	1.04 x 0.46 x 1.64	0.78	2
	Rectifier diode	600 V/ 5 A	1.02 x 0.45 x 1.59	0.73	6
	C_{out}	33μF	1.6 x 2.5	5.03	7.38

5.3.4 Summary of weight and size

A summation of weight and volume for the various topologies are presented in Table 5.14. The total number of components for each topology is included based on subsection 4.5.4.

Table 5.14: Total weight-and volume of the different topologies.

	Volume [cm^3]			Weight [g]		
Component	**4A**	**6A**	**8A**	**4A**	**6A**	**8A**
AC/DC Boost	28.07	49.60	58.91	93.37	113.55	140.92
AC/DC Totem	25.48	42.19	59.21	58.23	116.84	127.14
DC/DC Half-bridge	38.03	37.74	37.50	108.77	120.88	120.31
DC/DC Full-bridge	36.64	37.1	36.153	102.77	116.08	114.88

EMI-filters were not included in Table 5.14. However, the filters were included in the total volume's and weight's in the final design, see subsection 5.7.

5.4 LTspice simulation

In order to verify that the calculated components from the previous chapter were relevant to implement for the selected topologies to the off-board charger, they were tested in LTspice. These simulation models were compared regarding efficiency, PF, and THD. To avoid errors in LTspice, the simulation parts were simulated separately from each other.

All simulations in AC/DC stage were based on transient analysis in order to generate plots of the voltage and current in relation to time. The starting time was set as zero, where a time period of 300 ms was selected for AC circuits. This was since a large variation in the losses for each component and to ensure steady-state is reached. For the DC circuits, 30 ms was selected. The EMI filters were not included in the simulation since interference was not investigated.

5.4.1 AC/DC converter with Boost PFC

To simulate the AC grid that was supplying the charger with power, a voltage source was selected with the properties, sine wave, AC 230 V (RMS), 50 Hz. In order to obtain 230 V (RMS), an amplitude of 325.27 V was selected with a low serial resistance. By using the trace label tool in LTspice, the RMS value for the input voltage was verified to be 230 V (RMS) and the input current was about 4.5 A (RMS). To obtain the different input currents from the grid, a current load was connected. For this case, to obtain approximately 4 A from the AC grid, the current load must be adjusted to 164 Ω according to the following steps

$$P_{in} = V_{in} \times I_{in} = 230 \times 4.25 = 977.5W. \tag{5.20}$$

$$I_{out} = \frac{P_{in}}{V_{out}} = \frac{977.5}{400} = 2.44A. \tag{5.21}$$

$$R = \frac{V_{out}}{I_{out}} = \frac{400}{2.44} = 164\Omega. \tag{5.22}$$

This value was set to the current load, together with the calculated standard values to the circuit for 4 A current rate. To obtain the other input currents for 6 A and 8 A from the grid, the current load is adjusted to 113 Ω respectively 87 Ω.

For the PFC controller, it was desirable to select an IC PFC circuit that has the ability to operate with a high switching frequency and CCM mode. Thus, the LT1248 controller was selected for this converter. An additional diode was connected in parallel with the Boost inductor and Boost diode to maintain the power. This is shown in Figure 5.7, where the AC/DC converter with Boost PFC is simulated in LTspice.

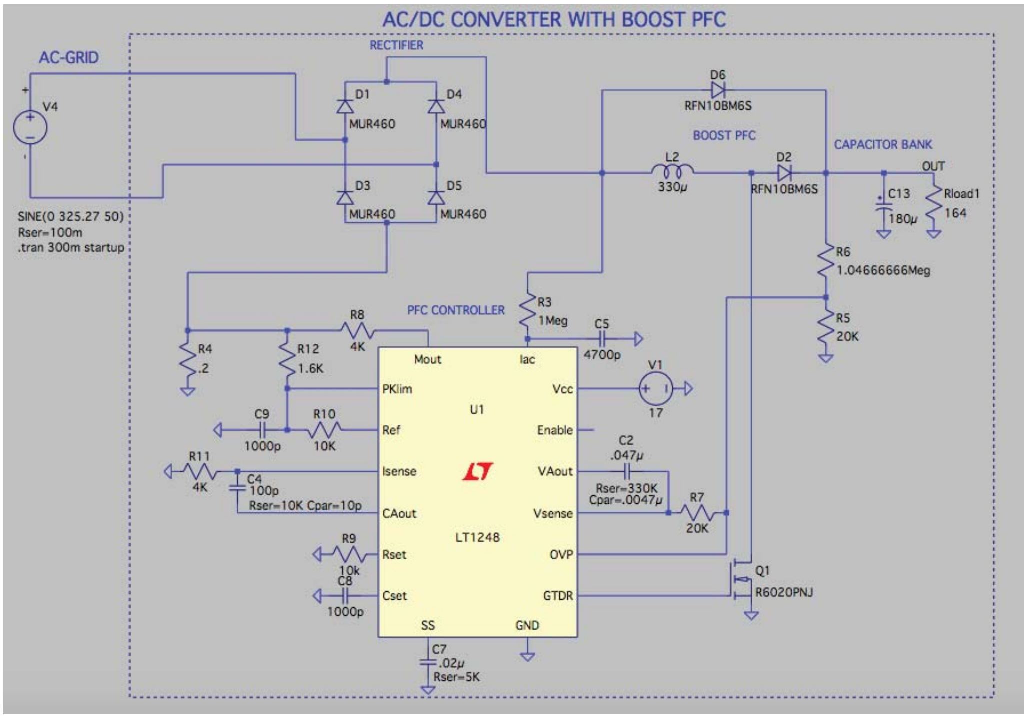

Figure 5.7: Simulation schematic in LTspice of the AC/DC converter with Boost PFC.

The output voltage was set to be approximately 400 V by having the R_1= 1.0467 MΩ and R_2 = 20 kΩ according to equation 4.4.

$$V_{out} = V_{ref} \times \left(\frac{R1 + R2}{R2}\right) = 7.5 \times \left(\frac{1.0467e^6 + 20e^3}{20e^3}\right) = 400V. \tag{5.23}$$

The switching frequency of 150 kHz was selected by having R_{SET}=10 kΩ and C_{SET}=1000 pF on the IC in LTspice, accordingly to frequency graph found in datasheet. According to equation 4.5, gave the switching frequency as

$$f_{sw} = \frac{1.5}{R_{SET} \times C_{SET}} = \frac{1.5}{10e^3 \times 1000e^{-12}} = 150kHz. \tag{5.24}$$

In Figure 5.8, it is shown that the AC input-current and voltage are in phase with each other. This implied that PFC circuit was operating properly. It was observed that there is a phase-shift between current and voltage for 10 ms before they approached unity.

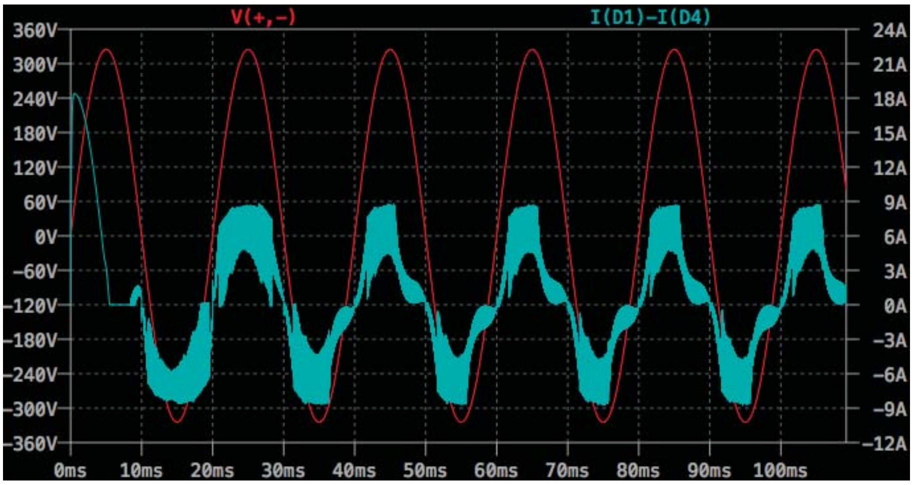

Figure 5.8: The waveforms of input voltage-and current from the AC grid with a PFC.

At the PFC bus from converter, the output voltage was V_{PFCout}= 400.58 V with an output current I_{out}= 2.44 A, seen in Figure 5.9. As shown in the graph, it took about 80 ms for the PFC to reach steady state at the output. A small overshoot of the voltage and current occurred in the first 10 ms of the time-period when a higher current is used at the input. An output ripple current of 290 mA and output ripple voltage of 48 V. By increasing the output capacitance, the ripple can be mitigated. However, the DC/DC converter in the next stage is expected to remove the ripple.

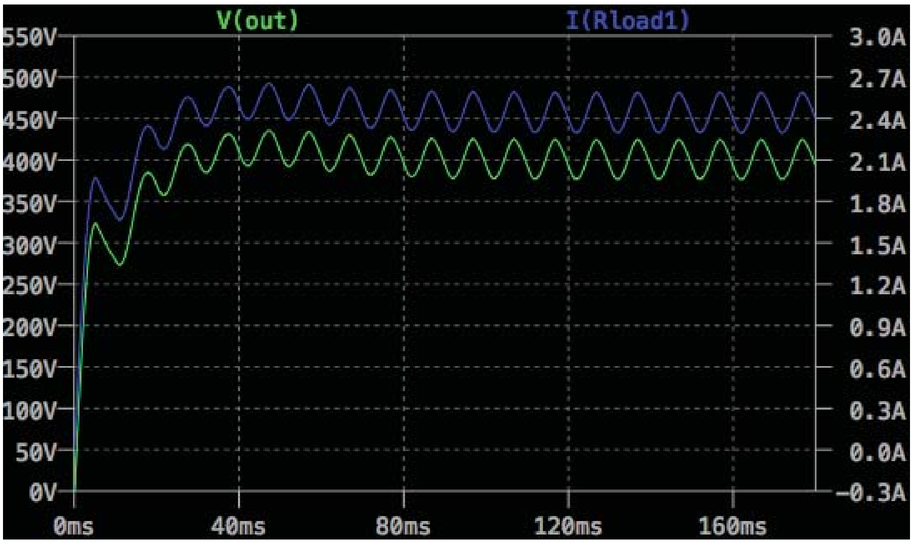

Figure 5.9: The waveforms of output voltage-and current from Boost PFC with 230 V (RMS) and 4 A supplied from grid.

The same mathematical procedure for the current load was executed for 6 and 8 A. This gave the current load to be 113 Ω and 87 Ω. This gave V_{PFCout}= 364.90 V and I_{out}= 3.23 A for 6 A, V_{PFCout}= 332.85 V and I_{out}= 3.83 A for 8 A.

5.4.2 AC/DC converter with Totem-pole PFC

Since there was no available Totem-pole IC circuit for LTspice, another IC PFC circuit had to be selected and modified to operate as a Totem-pole configuration. Once again, the LT1248 was selected for this application. Since this Totem-pole configuration has two switches, the frequency needed to be doubled to 300 kHz. Therefore, according to equation 4.5, the components are set to be R_{SET}=15 kΩ and C_{SET}=300 pF on the IC. The output voltage was set to be 400 V. The AC/DC converter with Totem-pole PFC is shown in Figure 5.10.

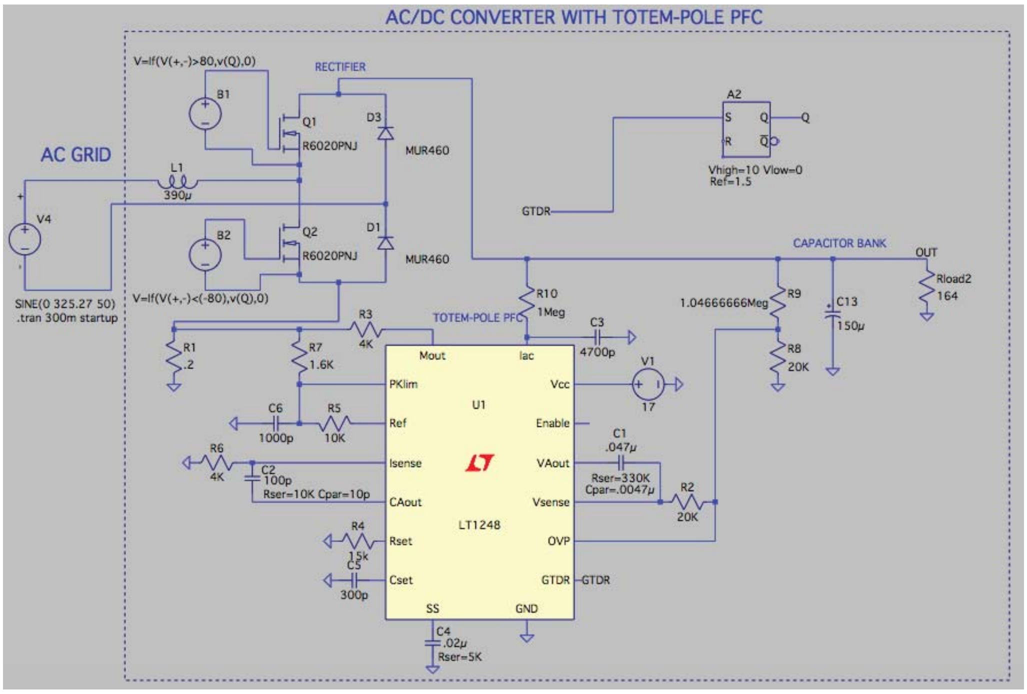

Figure 5.10: Simulation schematic in LTspice of the AC/DC converter with Totem-pole PFC.

Since Totem-pole had a complex control configuration, the pulse sequence for the switches was simplified [152]. The gate drive (GTDR) signal from the IC was connected to a SR-flip flop, where its output signal was fed to two behavioral voltage sources that are controlling the transistors. Q1 was activated at the positive half side of AC input waveform, and Q2 was activated at the negative half side. The pulse sequence for the transistors Q1 and Q2 together with the AC voltage input waveform is presented in Figure 5.11.

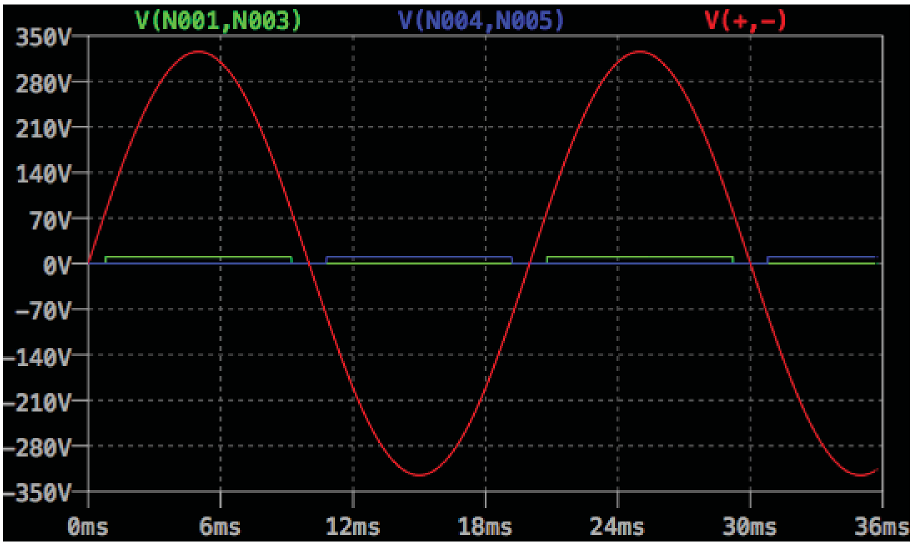

Figure 5.11: The waveforms of AC voltage input and the pulse sequence of Q1 and Q2.

At the PFC bus, the output voltage was V_{PFCout}=289.54 V with an output current I_{out}=1.76 A, seen in Figure 5.12. It is noticed that there were both output ripple current of 490 mA and output ripple voltage of 85 V. By increasing the value of the output capacitor, the ripple can be mitigated. However, in the next conversion stage, the DC/DC converter is expected to remove the ripple.

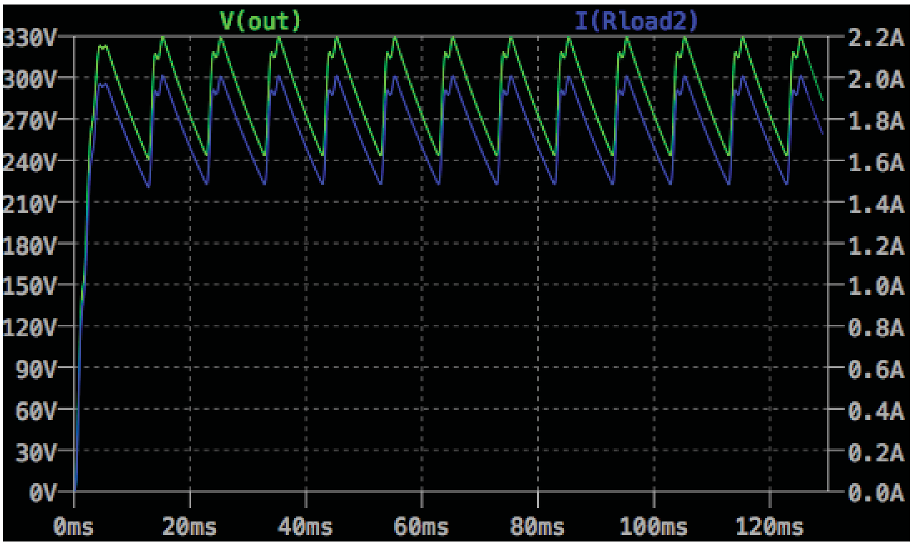

Figure 5.12: The waveforms of output voltage-and current from Totem PFC with 230 V (RMS) and 4 A supplied from grid.

5.4.3 Full-bridge and Half-bridge DC/DC converter

Since the simulation parts are not connected with each other, a voltage source was connected to the DC/DC converter to simulate the incoming DC voltage from the previous converter stage. It was expected that the ripple in the DC voltage are removed from the next switching elements. Thus, the ripple was neglected to be simulated. The transistors were operating with 200 kHz as a switching frequency accordingly to the design specification. The duty cycle needed to be adjusted to 30 %. The transistors M1 and M4 was operated with the same pulse parameters, while M2 and M3 had the same parameters included a delay time, thus the pulses would be separated from each other. It was assumed that the LV system is supplying the transistors with PWM. In Figure 5.13, the isolated Full-bridge DC/DC converter is shown.

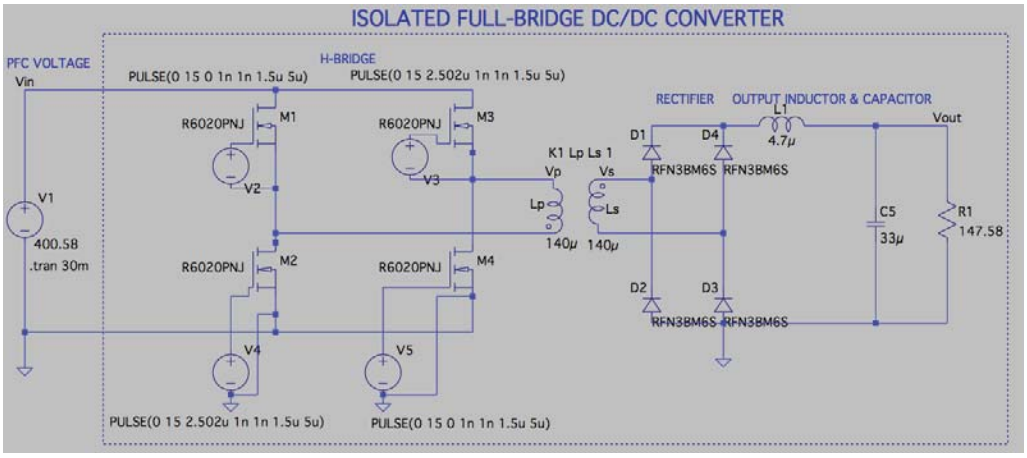

Figure 5.13: Simulation schematic in LTspice of the Full-bridge DC/DC converter.

For an input current of 4 A from the AC grid, the transformer ratio was adjusted to 14:14 ratio to obtain an output voltage in the interval of the HV battery operation mode. Thus primary winding was set to be N_p=140 μH and the secondary winding to N_s=140 μH. The current load needs also to be adjusted to obtain correct input current. The value of the output inductor needed to be reduced in order to avoid too high overshoot. From the Boost PFC bus, the input to DC/DC converter gave $V_{PFC(out)}$= 400.58 V and $I_{PFC(out)}$= 2.44 A, where the current load was set to be 147.58 Ω. It could be noted there is a small ripple of the input current of 12 mA.

This gave the output current- and voltage waveforms to be V_{out}=380.95 V and I_{out}=2.5627 A from the DC/DC converter. It can be observed that there is a small overshooting in both the current and voltage in the first 1.5 ms. This delivered output is within the charging range 320-380 V DC which is sufficient to charge the HV battery. The waveforms are shown in Figure 5.14.

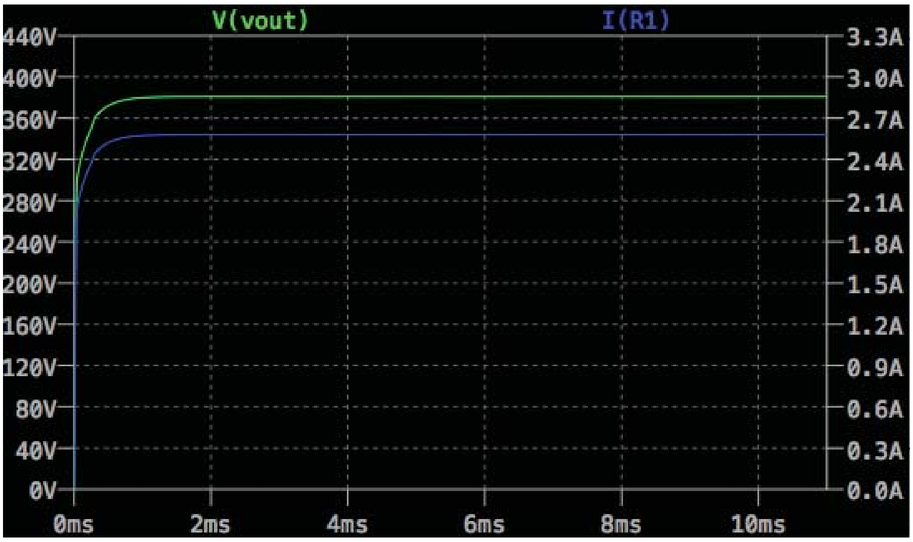

Figure 5.14: The waveforms of output voltage-and current from the DC/DC conversion stage when 4 A supplied from the AC grid.

For the Half-bridge DC/DC converter, two transistors in the primary bridge were removed and replaced by two capacitors connected in parallel to demonstrate Half-bridge configuration. From simulation, it was concluded that the capacitor value needed to be 47 μF. According to calculations, the transformer ratio was 7:14, where the inductance is proportional to N^2, thus the primary winding was set to be N_p=70 μH and N_s =280 μH. The output inductor and current load were set to be the same as in the Full-bridge. In Figure 5.15, the Half-bridge converter is shown.

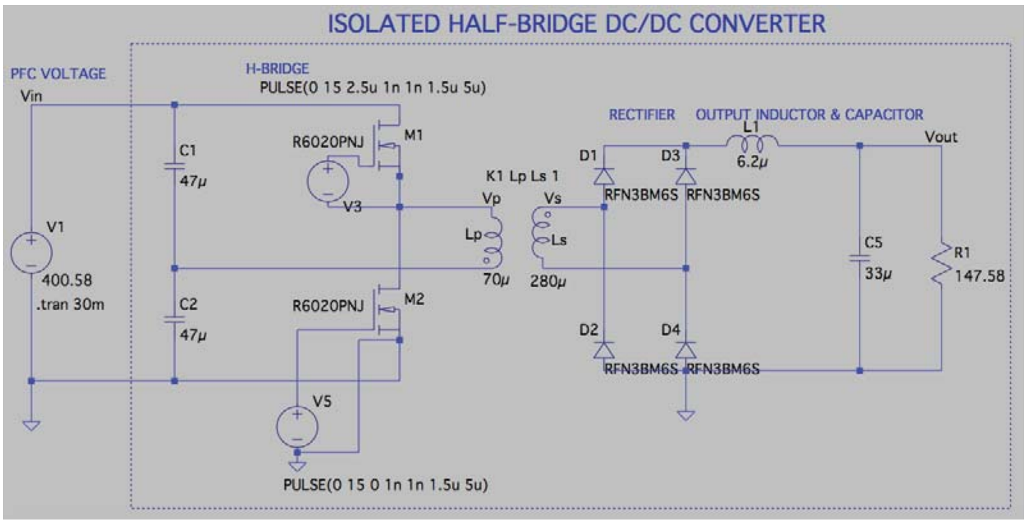

Figure 5.15: Simulation schematic in LTspice of the Half-bridge DC/DC converter.

This gave similar a result as in the Full-bridge, V_{out}=380.40 V and I_{out}=2.577 A.

A summary of the voltage and current outputs from all simulations are shown in Table C.1 and in Table C.2 in Appendix C.

5.4.4 Summary of LTspice results

Since it was observed from the simulation that the efficiency results were approximately 50 % for Totem-pole and Boost efficiency decreased with higher current indicates that the PFC circuits were not optimized to run a Totem-pole configuration. This was due to that there is no PFC IC component existing in LTspice for that particular topology. Additionally, the switching sequence for Totem was too complex to design from scratch. Thus, the output voltage is assumed to be 400 V in further calculations.

To obtain the THD-and PF data, a fast Fourier transformer (FFT) analysis was performed at the AC input current where harmonics were analyzed with higher frequency. With 4 A supplied to the Boost PFC, gave the frequency components shown in Figure 5.16. THD and PF values for the Totem-pole PFC was based on test results from a 1.6 kW Totem-pole PFC circuit from Texas Instruments [153].

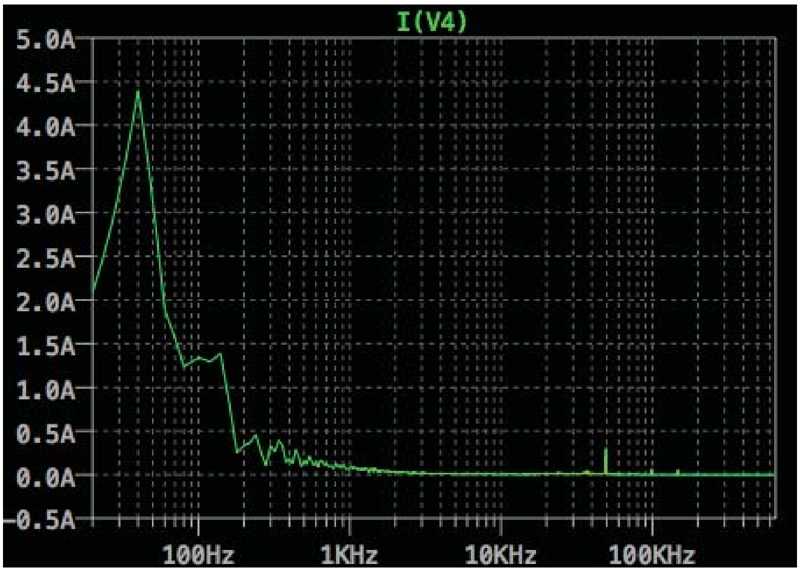

Figure 5.16: Peaks currents levels with higher frequency.

As shown in the graph, the distortion was reduced at a higher frequency. The level of THD for the various input currents 4 A, 6 A respectively 8 A, is shown in Figure 5.17.

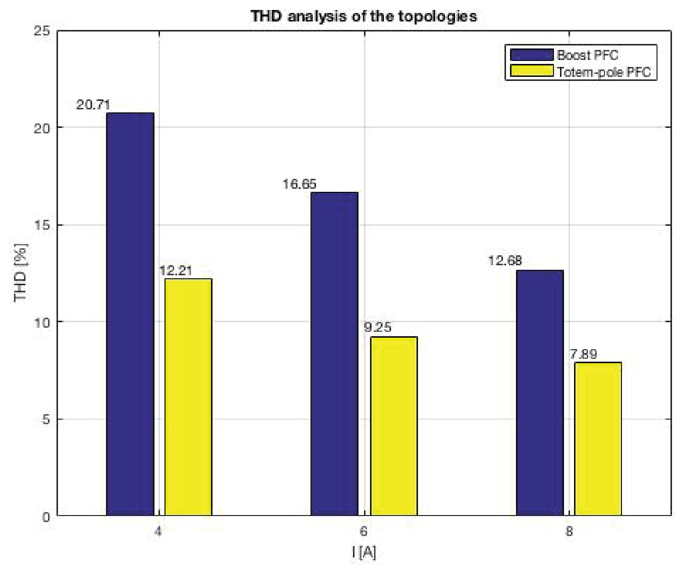

Figure 5.17: THD level at AC input current for the Boost-and Totem PFC.

This shows that it was favorable to select the Totem-pole PFC topology since it has lower THD compared to Boost PFC.

PF for the different topologies at the different current ratings are presented in the graph in Figure 5.18.

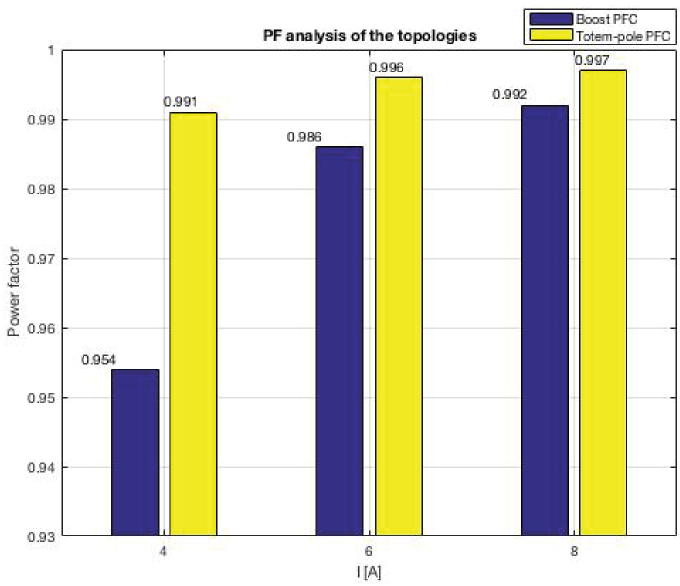

Figure 5.18: PF level at AC input current for the Boost-and Totem-pole PFC.

The graph evidently shown that PF level is higher for the Totem-pole topology than the Boost PFC. Again, this indicated that the Totem-pole PFC was more beneficial.

5.5 Power loss calculations

In order to obtain the power losses data for the selected AC/DC topologies, the input and output parameter are presented in Table 5.15. The calculations below are an estimation of the power losses.

Table 5.15: Input and output parameters of the AC/DC converter for 4 A.

Parameter	Boost	Unit
Power input	978.26	W
Voltage input	230	V
Voltage output	400	V
Current input	4.2533	A
Switching frequency	150	kHz

5.5.1 AC/DC Boost

Based on subsection 4.9.1, the power loss calculations steps are presented for each component [69].

Input diode-bridge
To calculate the power loss for the input rectifier diode bridge, the Schottky diode STPSC406 was used. The voltage drop are about 1.9 V at 150 °C at current 4 A, values taken from datasheet diagram [118]. The switching losses were neglected for the input rectifying diode bridge due to the low frequency of 50 Hz.

$$I_{avg} = \frac{I_{ac,RMS} \times \sqrt{2} \times 2}{\pi} = 3.8293A \tag{5.25}$$

where the the input RMS-current is 4.2533A from calculation.

Conduction loss for the diode-bridge of a half cycle was

$$P_{conduction} = 2 \times V_F \times I_{avg} = 1.9 \times 3.8293 = 14.55139W. \tag{5.26}$$

Boost diode PFC
Both conduction losses and switching losses were calculated from [69]. The selected diode for the Boost PFC circuit was QH08TZ600. The current after the diode bridge was calculated with

$$I_{avg} = \frac{I_{ac,rms} \times \sqrt{2} \times 2}{\pi} = 3.8293A. \tag{5.27}$$

The voltage after the diode bridge was obtainted as

$$V_{dc} = \frac{V_{ac,rms} \times \sqrt{2} \times 2}{\pi} = 207.07V \tag{5.28}$$

The conduction loss can then be calculated as

$$P_{conduction} = V_F \times I_{avg} = 2.23 \times 3.8293 = 8.5393W \tag{5.29}$$

where the V_F at T_j at 150 °C is 2.23 V from datasheet [113]. The turn-off losses in a diode were relative small, therefore could be neglected, while the turn-on losses are [157],

$$P_{switching} = (E_{on} + E_{off}) \times f_{sw} \approx E_{on} \times f_{sw} \tag{5.30}$$

where E_{on} depends on Q_{RR} and V_R which are seen in

$$E_{on} \times f_{sw} = 0.25 \times Q_{RR} \times V_R \times f_{sw} = 0.25 \times 25.5n \times 400V \times 150kHz = 0.3825W \tag{5.31}$$

where Q_{RR} is the reverse recovery charge taken from datasheet [113].

The total diode Boost loss then became

$$P_{loss} = P_{conduction} + P_{switching} = 8.5393 + 0.3825 = 8.9218W. \tag{5.32}$$

Transistor PFC
The MOSFET STF10N60DM2 was selected for the Boost PFC circuit, where the duty cycle was calculated in previous subsection 5.3.2.1.

$$D = \frac{U_o - U_{in}}{U_o} = 0.19. \tag{5.33}$$

The conduction losses are

$$P_{conduction} = R_{DS,on} \times {I_{avg}}^2 \times D = 0.53 \times 3.8293^2 \times 0.19 = 1.47663W \tag{5.34}$$

where the $R_{DS,on}$ are the drain-source on-state resistance and the I_{avg} was the output current from the rectifying diode bridge.

The switching loss could now be calculated as

$$P_{switching} = 0.5 \times V_{dc} \times I_{dc} \times (tr + tdon + tf + tdoff) \times f_{sw} \tag{5.35}$$

where the V_{dc} voltage was 207.07 V from previous calculations [94]. Thus the switching loss can be calculated with

$$P_{switching} = 0.5 \times (207.07) \times 3.8293 \times (55.5ns) \times 150kHz = 3.3003W \tag{5.36}$$

where t_{don} is the delay on-time and the t_{off} is the delay off-time from datasheet [143].

$$P_{loss} = P_{conduction} + P_{switching} = 1.47663 + 3.3003 = 4.776955W \approx 4.78W \tag{5.37}$$

The gate drive loss and turn on loss were neglected since they are considering to be relative small.

Boost inductor
The inductor losses are the same as in the Totem-pole induction calculation.

The inductor value was calculated to be 343 μH. A component was selected 2200LL-331-RC 330 μH and from datasheet, the DCR value is found to be 0.077 Ω. To calculate the Boost inductor losses the formulas used comes from [69].

The inductor current $I_{L,RMS}$ was calculated by utilizing the CCM boundary condition

$$I_{L,RMS} \geq \frac{\Delta I}{2} \tag{5.38}$$

where the current ripple was

$$\Delta I = \frac{V_L \times D}{L \times f_{sw}} = \frac{170V \times 0.19}{330\mu \times 150kHz} = 0.6525A \tag{5.39}$$

where the V_L is collected from the simulation.

The inductor current could now be found

$$I_{L,RMS} \geq \frac{\Delta I}{2} = \frac{0.6525}{2} = 0.3262A. \tag{5.40}$$

The DCR value 0.077 Ω was found in the inductor datasheet [111].
The inductor copper loss was calculated by using

$$P_{loss} = P_{DCR} = {I_{L,RMS}}^2 \times DCR = 0.3262^2 \times 0.077\Omega = 0.008196W \tag{5.41}$$

since the inductor power loss value was low, it will be neglected for all current levels within power loss calculations [157]. The inductor core losses were not taken into consideration.

DC-link
When calculating the DC-link losses, the reactance needed to be known. A capacitor of 47 μF is used.

$$X_c = \frac{1}{2 \times \pi \times f_{sw} \times C} = \frac{1}{2 \times \pi \times 150kHz \times 47\mu F} = 0.022575W. \tag{5.42}$$

Then the equivalent series resistance (ESR) can be calculated

$$ESR = tan\delta \times X_c = 0.24 \times 0.022575W = 0.0013W. \tag{5.43}$$

where $tan\delta$ is from datasheet [132].
Now the losses can be found using

$$P_{loss} = {I_{co,RMS}}^2 \times ESR = 2.44^2 A \times 0.0013W = 0.007778W. \tag{5.44}$$

where $I_{co,RMS}$ is the RMS output capacitance current. In this case, the current was assumed to be 2.44 A since the maximal output current was equal to the input power P=978.26 W divided by the output voltage V=400 V.

Four capacitors, 47 μF each, are needed in the DC-link. Thus, the total loss was

$$P_{loss} = 4 \times 0.007778A = 0.03111W \tag{5.45}$$

The losses for AC/DC for both Totem-pole and Boost are calculated for 6 A and 8 A with the same mathematical procedure as above. This is summarized in Table 5.16 and Table 5.18.

Table 5.16: Power losses for Boost at different current levels.

Boost			
Loss [W]	**4A**	**6A**	**8A**
Input diode-bridge	14.55	17.69	31.83
PFC Diode	8.92	12.17	17.30
PFC transistor	4.78	7.47	11.54
Inductor	-	-	-
DC-link	0.0312	0.1168	0.04705
Total power loss	28.26	37.36	60.68
Output power	950	1375.68	1787.15
Efficiency [%]	97.11	97.36	96.72

A loss comparison was conducted to see how reasonable the calculated loss values are. The Boost power loss values below were calculated by finding efficiency value in literature and by using

$$P_{loss} = (1 - \eta) \times P_{in} = (1 - 0.9725) \times 978.26 = 26.902W \tag{5.46}$$

where the η is found to be 97.25 % when the output power was assumed to be around 950 W shown in Figure 5.19 [155].

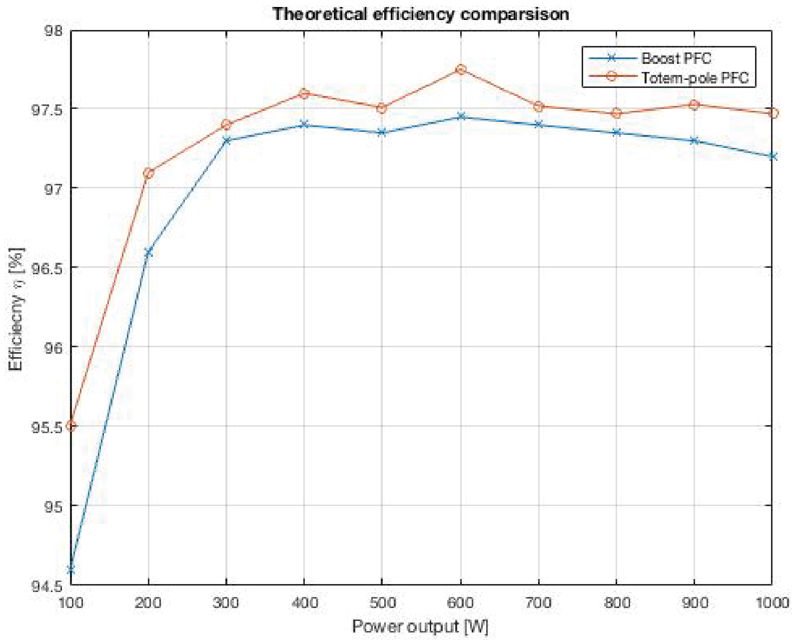

Figure 5.19: Comparison of theoretical efficiency of the Boost PFC and Totem-pole PFC at different output power [155].

From this, it can be seen that the calculated power loss and the loss from the graph is within the same size, hence the results seem to be reasonable.

5.5.2 AC/DC Totem-pole

Since the power loss calculations for the Totem-pole has been more difficult to find good estimation equations, the Totem-pole power loss values are instead calculated from finding efficiency value in literature, see Figure 5.19, hence

$$P_{loss} = (1 - \eta) \times P_{in} = (1 - 0.975) \times 978.26 = 24.46W \tag{5.47}$$

where the η is found to be 97.5 % when the output power was assumed to be around 950 W from Figure 5.19.
The difference in power loss between Boost and Totem-pole was

$$\Delta P_{loss} = P_{loss,boost} - P_{loss,totem} = 26.902W - 24.46W = 2.4455W. \tag{5.48}$$

From the calculated ΔP_{loss}, an estimation for power loss of Totem-pole at different current levels can be achieved, shown in Table 5.17. The difference ΔP_{loss} between Boost and Totem-pole is assumed to be constant.

Table 5.17: Totem-pole estimation power losses.

Power loss [W]	Boost	Totem
4A	28.26	25.81
6A	37.36	34.92
8A	60.68	58.23

The power loss and efficiency for the other input current ratings, are presented in Table 5.18, where ΔP_{loss} was assumed to be constant for all cases.

Table 5.18: Power losses for Totem-pole at different current levels.

Totem-pole			
Loss [W]	**4A**	**6A**	**8A**
Total power loss	25.81	34.92	58.23
Output power	952.45	1378.12	1789.60
Efficiency [%]	97.36	97.53	96.85

5.5.3 DC/DC - Half and Full

In order to obtain the power losses data for the selected DC/DC topologies, the input and output parameter are presented in Table 5.19. For this subsection, the loss calculations were based on the selection that Totem-pole was the selected AC/DC converter.

For the DC/DC converter, the V_{in} was assumed to be 400 V and the V_{out} was assumed to be 380 V. The 380 V output voltage is desired since the HV battery is having a charging range between 320-380 V.

The output voltage from Boost and Totem-pole AC/DC was assumed to be 400 V, [34]. The input voltage for the DC/DC Full-bridge transistors was 400 V, while for Half-bridge the input voltage at the transistors are 200V. The input voltage of the transformer after the transistor was obtained from simulation, 394 V for the Full-bridge, and 196 V for the Half-bridge.

DC/DC input current has been calculated by taking the AC/DC output power and divide it with the voltage 400 V, hence for current level 4 A the DC/DC input current is calculated to be 2.381 A. The calculations below are the same equations used in subsection 5.5.2, with same references.

Table 5.19: Input DC/DC values taken from Totem-pole calculation.

Current levels	**Totem**	
Full-bridge	**Vin [V]**	**Iin [A]**
4A	400	2.381
6A	400	3.445
8A	400	4.474
Half-bridge	**Vin [V]**	**Iin [A]**
4A	400	2.381
6A	400	3.445
8A	400	4.474

Transistor
The selected MOSFET was R6004KNX [143]. According to equation 4.11 and

equation 4.12, the duty cycle was close to be 0.5 for the switches at both Half-bridge and Full-bridge. The conduction losses for the Half-bridge converter were

$$P_{conduction,half} = R_{DS,on} \times {I_{Don}}^2 \times D = 0.98 \times 2.381125^2 \times 0.5 = 2.77818W \quad (5.49)$$

where the $R_{DS,on}$ are the drain-source on-state resistance taken from datasheet [143],[156]. I_{Don} is assumed to be the input DC/DC current.

The conduction loss was the same also for the Full-bridge converter. The switching loss for Half-bridge could be calculated as

$$P_{switching,half} = 0.5 \times V_{dc} \times I_{dc} \times (tr + tdon + tf + tdoff) \times f_{sw}. \quad (5.50)$$

$$P_{switching,half} = 0.5 \times 200V \times 2.381125A \times (80ns) \times 200kHz = 3.8098W \quad (5.51)$$

and the switching loss for Full-bridge could be calculated as

$$P_{switching,full} = 0.5 \times 400V \times 2.381125A \times (80ns) \times 200kHz = 7.6196W. \quad (5.52)$$

The total losses for one transistor in Half-bridge converter

$$P_{loss,half} = P_{conduction,half} + P_{switching,half} = 2.77818 + 3.8098 = 6.58798W. \quad (5.53)$$

The total losses for one transistor in Full-bridge converter

$$P_{loss,full} = P_{conduction,full} + P_{switching,full} = 2.77818 + 7.6196 = 10.39778W. \quad (5.54)$$

The total losses at half a cycle, thus for the Full-bridge, two transistors turned on simultaneously and for the Half-bridge one transistor turned on at a time.

$$P_{tot,half} = P_{conduction,full} + P_{switching,full} = (2.77818 + 3.8098) = 6.58798W. \quad (5.55)$$

$$P_{tot,full} = 2 \times P_{conduction,full} + P_{switching,full} = 2 \times (2.77818 + 7.6196) = 20.79556W. \quad (5.56)$$

Output diode-bridge
The selected diode was C3D03060F at a switching frequency of 200 kHz.

For the Full-bridge, the current from secondary winding is 3.969776 A which was utilized to calculate the diode rectifier output current I_{dc}.

$$I_{dc} = \frac{2 \times \sqrt{2} \times I_{RMS}}{\pi} = 3.574A. \tag{5.57}$$

The conduction losses for the diode rectifier bridge during a half-cycle was calculated as

$$P_{conduction} = 2 \times V_F \times I_{dc} = 2 \times 1.8V \times 3.574 = 12.866594W \tag{5.58}$$

where the voltage drop V_F=1.8 V was taken from datasheet.

To calculate the switching losses,

$$P_{switching} = (E_{on} + E_{off}) \times f_{sw} \approx E_{on} \times f_{sw} \tag{5.59}$$

$$E_{on} = Q_{RR} \times V_R \tag{5.60}$$

where the values of the reverse recovery current Q_{RR} are given from a datasheet. However, since there is no reverse recovery charge for the for SiC diode, the switching losses became low. Therefore, these losses were assumed to be neglected [157].

In the output rectifying diode bridge, two diodes are conducting simultaneously, hence the total losses became

$$P_{loss,full} = (P_{conduction} + P_{switching}) = 12.866594W. \tag{5.61}$$

For Half-bridge the output diode bridge current is 3.29268 A, hence I_{dc} became 2.96445 A. The same calculations were proceed for the Full-bridge. The conduction losses then became

$$P_{conduction} = 2 \times V_F \times I_{dc} = 2 \times 1.8V \times 2.96445 = 10.6720327W \tag{5.62}$$

with the switching losses neglected, the power loss is obtained with

$$P_{loss,half} = (P_{conduction} + P_{switching}) = 10.6720327W. \tag{5.63}$$

Inductor
The inductor loss for the the Full-bridge became

$$P_{loss,full} = {I_{dc}}^2 \times DCR = 3.574054^2 \times 0.005 = 0.06386931W \tag{5.64}$$

where the DCR value was collected from datasheet

$$P_{loss,half} = {I_{dc}}^2 \times DCR = 2.96445^2 \times 0.005 = 0.04394W. \tag{5.65}$$

Output capacitor
When calculating the DC-link losses [69] for the Full-bridge, the reactance was required, which was obtain with the expression

$$X_c = \frac{1}{2 \times \pi \times f_{sw} \times C} = \frac{1}{2 \times \pi \times 200kHz \times 33\mu F} = 0.02411W. \tag{5.66}$$

Then equivalent series resistance (ESR) was calculated

$$ESR = tan\delta \times X_c = 0.25 \times 0.02411W = 0.006028W. \tag{5.67}$$

where $tan\delta$ was collected from datasheet [149].
The output current is determined from

$$I_{out} = \frac{P_{out,inductor}}{V_{out}} = \frac{899.1339W}{380V} = 2.36614A \tag{5.68}$$

Now the losses could be found using

$$P_{loss} = {I_{co,RMS}}^2 \times ESR = 2.4^2 A \times 0.006028W = 0.0347229W. \tag{5.69}$$

where $I_{co,RMS}$ was assumed to be similar in size to the output inductor current.

For Half-bridge the output inductor current was

$$I_{out} = \frac{P_{out,inductor}}{V_{out}} = \frac{923.699W}{380V} = 2.430787A. \tag{5.70}$$

Now the losses for the capacitor at Half-bridge was obtained using

$$P_{loss} = {I_{co,RMS}}^2 \times ESR = 2.430787^2 A \times 0.0042328W = 0.025010716W. \tag{5.71}$$

Transformer
The transformer has been selected according to several reasons. Partly because to minimize the size and receive high efficiency in order to gain optimal heat development.

A transformer material was selected to be 3F3 since it was used for 40-420 kHz [6]. Also, a transformer core was selected as ETD49/25/16-3F3. This transformer core has an area of 211 mm^2 and a core diameter of 16.39 mm. ETD core includes a round core, which implies that the winding resistance will decrease.

The maximum saturated flux density for soft ferrite material is 0.35 T. Hence, B_m was a value lower than 0.35 T. For a switching frequency of 200 kHz and temperature of 100 °C, a flux density of 150 mT was assumed to be reasonable.

To be able to choose a suitable transformer core size a comparison was made, see Table D.2 and Table D.3 in Appendix D.

To calculate the transformer losses, Half-bridge was selected to perform a complete calculation and could then be compared with the Full-bridge. The formulas below are calculated for Half-bridge at current level of 4 A. The number of turns was obtained by first calculating the turns per volt that are required

$$T_e = \frac{1}{4.44 \times f_{sw} \times B_m \times A_c} = 0.03558 Turns/volt \tag{5.72}$$

where T_e is $\frac{1}{Vind}$, V_{ind} is induced voltage. The value 4.44 represents a sinusoidal waveform, A_c is the core area and the B_m is the maximum magnetic flux density [100].

Thus, the number of turns in primary winding was given by the expression follows as

$$N_p = T_e \times V_p = 0.03558 \times 196.06V = 6.97 \approx 7turns \tag{5.73}$$

where V_p is the voltage in the primary winding, with a value of 196.06 V collected from simulation. The secondary winding turns are

$$N_s = T_e \times V_s = 0.03558 \times 380V = 13.52 \approx 14turns. \tag{5.74}$$

The skin depth (d) was calculated in order to see how large area of the wires should be designed when considering the skin effect. The skin depth was calculated by

$$d = \frac{1}{\sqrt{\pi \times \mu_0 \times \sigma \times f_{sw}}} = 0.000145897m \approx 0.1458mm \tag{5.75}$$

where μ_0 is the permeability in vacuum and σ is the conductivity in copper [6].

From the skin depth d=0.1458 mm, the diameter of wire where the all part of wires is used became 0.2918 mm, thus the area was 0.066 mm^2. However, to increase the concentration of current density of the calculated wire size, the diameter was selected to be $\leq$ 0.1 mm.

The window area is the amount of space that the $wire_{Bundle}$ can conform inside the core. This area was calculated as

$$A_w = b_w \times h_w = 186.43mm^2 \tag{5.76}$$

where width b_w=10.3 mm and height h_w=18.1 mm was selected from the datasheet [158].

The maximum area that the copper wire was dimension with was obtained with

$$A_{cu,max} = \frac{k_{cu} \times A_w}{N_p + N_s} = 2.663mm^2 \tag{5.77}$$

where k_{cu} is the copper fill factor, which for Litz wire has the value of 0.3 [6].

The copper wire area should be less than 2.663 mm^2. From datasheet, a Litz-wire is selected with a diameter of 0.1 mm and with 270 number of strains, which became an area of 2.545 mm^2. Litz wire is often utilized at high frequencies in order to reduce the losses.

The core girth of the transformer was defined by

$$Girth = D_{core} \times \pi = 16.39 \times \pi = 51.522mm \tag{5.78}$$

where the diameter D_{core}=16.39 mm from the datasheet [158].

The length of the wire was calculated as

$$L = Girth \times (N_p + N_s) = 51.522 \times 21 = 1081.96mm \approx 1.08m \tag{5.79}$$

Thus for the length of the wire on the primary side, was expressed by

$$L_p = Girth \times N_p = 360.654mm \approx 0.36m. \tag{5.80}$$

The length of the wire on the secondary side was expressed by

$$L_s = Girth \times N_s = 721.308mm \approx 0.72m. \tag{5.81}$$

The size of the transformer was estimated by obtaining the volume by

$$V = l \times b \times h = 19727.39mm^3 \approx 19.7cm^3 \tag{5.82}$$

where the transformer length=48.7 mm, height=24.7 mm and width=16.4 mm from the datasheet. With an added I-core, the volume became 25 cm^3.

When calculating losses, the focus was on the major losses of the transformer, located in the winding and the core. There are other losses as well, however, they are significantly low in this case, that they are assumed to be neglected. The losses were calculated by

$$P_{loss} = P_w + P_{core}. \tag{5.83}$$

To calculate the winding losses P_w, the wire resistance is needed

$$R_{wire,p} = \frac{\rho_{cu} \times L_p}{A_{cu,bundle}} = 0.002381\Omega \tag{5.84}$$

$$R_{wire,s} = \frac{\rho_{cu} \times L_s}{A_{cu,bundle}} = 0.004762\Omega \tag{5.85}$$

where ρ_{cu} is the electrical resistivity of copper with the value 1.68×10^{-8}, and the copper wire area of the bundle was 2.5447 mm^2.
While the R_{dc} was obtained with the expression as follows

$$R_{dc,p} = (MTL) \times Np \times R_{wire,p} = girth \times 7 \times 0.002381 = 0.08587\Omega \tag{5.86}$$

$$R_{dc,s} = (MTL) \times Ns \times R_{wire,s} = girth \times 14 \times 0.004762 = 0.34349\Omega \tag{5.87}$$

where MTL is the mean turn length, which is assumed to be close to the girth value [101].

With R_{dc} known, the winding loss could be calculated

$$P_{w,p} = R_{dc,p} \times {I_{RMS,p}}^2 = 3.723928W \tag{5.88}$$

where $I_{RMS,p}$ was the input transformer current taken from simulation, 6.585366 A. To calculate the $P_{w,s}$ the $I_{RMS,s}$ was needed

$$I_{RMS,s} = I_{RMS,p} \times \frac{7}{14} = 3.29268A. \tag{5.89}$$

$$P_{w,s} = R_{dc,s} \times {I_{RMS,s}}^2 = 3.724029W. \tag{5.90}$$

$$P_{w,tot} = 7.447958W. \tag{5.91}$$

To calculate the magnetic loss density P_M, Steinmetz equation was implemented as

$$P_M = k \times f^a \times B^d_{peak} = 1047mW/cm^3 \tag{5.92}$$

where k, a and d are constants depending on what type of core material and frequency is used [98]. In the selected core, there is Ferrite material 3F3, thus the constants are $k = 2.5 \times 10^{-4}$, $a = 1.63$, $d = 2.45$ [103].

The volume of the core was calculated from and the values found in the datasheet [98]. This gave

$$V_{core} = A_{core} \times Height = 211 \times 18.1 = 3819mm^3. \tag{5.93}$$

The core losses were then calculated by

$$P_{core} = P_M \times V_{core} = 1.047 \times 3.819cm^3 = 3.999W. \tag{5.94}$$

This gave the total losses as

$$P_{loss} = P_w + P_{core} = 7.447958W + 3.999 = 11.446958W. \tag{5.95}$$

For Full-bridge the transformer losses became

$$P_{w,p} = R_{dc,p} \times I_{RMS,p^2} = 7.795417W \tag{5.96}$$

where $I_{RMS,p}$ is the input transformer current collected from the simulation, 3.705125 A.
To calculate the $P_{w,s}$ the $I_{RMS,s}$ was needed

$$I_{RMS,s} = I_{RMS,p} \times \frac{7}{14} = 3.969776A. \tag{5.97}$$

$$P_{w,s} = R_{dc,s} \times I^2_{RMS,s} = 7.79548W. \tag{5.98}$$

$$P_{w,tot} = 15.5909W. \tag{5.99}$$

$$P_{loss} = P_w + P_{core} = 6.99 + 3.999 = 19.5899W. \tag{5.100}$$

The values for P_{loss} are shown in Table 5.20, where the values for both Full-bridge and Half-bridge at the current level 4 A is shown.

The different current levels at both Full-bridge and Half-bridge has been calculated by utilizing the same presented equations. This is shown in Table 5.20.

Table 5.20: Calculated transformer parameters for different configurations and current levels for Totem-pole.

Totem-pole			**Full-bridge**	**Half-bridge**
Parameters	**Unit**	**Equation**	**4A**	**4A**
N_p	[Turns]	(5.73)	15	7
$A_{cu,max}$	$[mm^2]$	(5.77)	1.928	2.663
L_p	[m]	(5.80)	0.773	0.361
L_s	[m]	(5.81)	0.721	0.721
$R_{wire,p}$	$[m\Omega]$	(5.84)	7.347	2.381
$R_{wire,s}$	$[m\Omega]$	(5.85)	6.858	4.762
$R_{dc,p}$	$[\Omega]$	(5.86)	0.5678	0.0859
$R_{dc,s}$	$[\Omega]$	(5.87)	0.4947	0.3435
$P_{w,p}$	[W]	(5.88)	7.795	3.724
$P_{w,s}$	[W]	(5.98)	7.795	3.724
P_{loss}	[W]	(5.95)	19.589	11.447

5.5.4 Micro controller unit

The losses of the MCU in the LV board system was calculated according to equation 4.43 presented as

$$P_{loss} = V^2 \times f_{sw} \times C_{load} = 5^2 \times 285e^3 \times 5e^{-12} = 35.625\mu W \tag{5.101}$$

where the maximum values were selected to obtain the worst-case-scenario considering the losses. The switching frequency is selected to be 285 kHz, the supply voltage of V=5 V and C_{load}=5 pF. These selections were based on the datasheet [37]. To obtain the complete losses of the MCU, a scaling factor of 2 is multiplied with the losses for one pin. This gave the total power losses of the logic board as 71.25 μW. Since this loss value was considered to be low, this could be neglected in further calculations.

5.5.5 Summary of loss calculations

In comparison between Boost and Totem-pole, Table 5.21 and Table 5.22 shows that Totem is more efficient and has lower power losses.

Table 5.21: Efficiency - Boost.

Boost				
	Units	**4A**	**6A**	**8A**
Pin	[W]	978.26	1413	1847.8
Pout	[W]	950	1375.68	1787.15
Ploss	[W]	28.26	37.36	60.68
Efficiency	[%]	97.11	97.36	96.72

Table 5.22: Efficiency - Totem-pole.

Totem-pole				
	Units	**4A**	**6A**	**8A**
Pin	[W]	978.26	1413	1847.8
Pout	[W]	952.45	1378.12	1789.60
Ploss	[W]	25.81	34.92	58.23
Efficiency	[%]	97.36	97.53	96.85

From calculations a summary is shown in Table 5.23.

Table 5.23: Loss comparison of the four configurations.

	Equation	**4A**	**6A**	**8A**	**4A**	**6A**	**8A**
		Ploss [W]			**Ploss [W]**		
AC/DC:		**Totem-pole**			**Boost**		
Input rectifier diode bridge	(5.26)	11.1	16.2	27.3	14.55	17.69	31.83
Inductor	(5.41)	3.44	2.26	3.36	-	-	-
Diode	(5.32)	-	-	-	8.92	12.17	17.30
Transistor	(5.37)	11.1	16.2	27.3	4.78	7.47	11.54
DC-link	(5.45)	0.175	0.268	0.212	0.031	0.117	0.0102
DC/DC:		**Half-bridge**			**Full-bridge**		
Transistor	(5.53)	6.588	11.875	15.575	20.796	33.258	41.082
Transformer	(5.95)	11.447	20.584	31.688	19.589	30.842	47.875
Output rectifier diode bridge	(5.61)	10.672	24.773	32.008	12.867	26.262	33.576
Inductor	(5.65)	0.0439	0.0783	0.098	0.064	0.0879	0.144
Output capacitor	(5.69)	0.025	0.051	0.086	0.034	0.069	0.116

5.5.6 Topology selection

Considering all essential factors, weight, efficiency, PF, THD and power losses based on previous results, it was more favorable to select a Totem-pole than a Boost configuration for the AC/DC converter. Therefore, a Totem-pole was selected for further investigation. However, if the cost was taken into consideration, it would be more preferably to selected Boost since it was a less costly alternative. From here on out, the AC/DC converter with Totem-pole was conducted in further investigation.

With the AC/DC selection made, the comparison between Half-bridge and Full-bridge is shown in Table 5.24 and Table 5.25.

Table 5.24: Efficiency - DC/DC - Totem.

DC/DC Half-bridge - Totem				
	Units	**4A**	**6A**	**8A**
Pin	[W]	952.45	1378.12	1789.60
Pout	[W]	923.67	1320.76	1710.14
Ploss	[W]	28.77	57.36	79.46
Efficiency	[%]	96.98	95.84	95.56
DC/DC Full-bridge - Totem				
Pin	[W]	952.45	1378.12	1789.60
Pout	[W]	899.10	1287.64	1666.81
Ploss	[W]	53.34	90.48	122.79
Efficiency	[%]	94.39	93.43	93.14

Table 5.25: Total power loss - Totem-pole + DC/DC alternative.

Power losses [W]			
	4A	**6A**	**8A**
Totem	25.81	34.92	58.23
Half-bridge	28.77	57.36	79.46
Total:	**54.58**	**92.28**	**137.69**
Totem	25.81	34.92	58.23
Full-bridge	53.34	90.48	122.79
Total:	**79.15**	**125.40**	**181.02**

The Half-bridge has the lowest power loss and has slightly higher efficiency as shown in Table 5.24 and Table 5.25. The weights between Half-bridge and Full-bridge were relative similar. Therefore, the weight was considered to not to be a major factor in this selection.

From Table 5.24 and Table 5.25, data for Totem-pole and Half-bridge were combined and utilized to design the cooling system for the charger.

From the total losses, the new output power can be calculated. For Totem-pole and Half-bridge converter at current level 4 A gave

$$P_{out} = P_{in} - P_{loss} = 978.26 - 54.58 = 923.68W. \tag{5.102}$$

Efficiency is then 94.42% for the total off-board charger.

5.6 Cooling system

To find an applicable heatsink for the selected circuits and components, thermal resistance needed to be known. This was obtained through calculations based on the equation in subsection 4.9.2.

In order to analyze the temperature levels of the components mounted on a heatsink, the Heatsinkcalculator simulation tool was utilized. This tool is designed to be simplified and to generate quick results. Since the transistors, diodes, and transformer required to have most cooling, these components are mounted on the heatsink.

5.6.1 Heat calculations

Transistor
To avoid the operating temperature of the components exceeds 150 °C, the thermal resistance for a transistor in the Half-bridge at current level 4 A was calculated as

$$R_{th,ja} = \frac{T_{j,max} - T_a}{P_{loss}} = \frac{150 - 40}{6.588W} = 16.697°C/W \tag{5.103}$$

where the $T_{j,max}$ of 150 °C was collected from datasheet [143]. T_a was selected to be 40 °C to simulate a worst-case temperature. For the second transistor in the Half-bridge, the $R_{th,ja,2}$ became 16.697 °C/W. The thermal resistance between heatsink and ambient is

$$R_{th,sa} = R_{th,ja} - R_{th,jc} - R_{th,cs} = 16.697 - 3.13 - 0.8 = 12.767°C/W \tag{5.104}$$

where the $R_{th,cs}$ is thermal resistance of TIM which is assumed to be 0.8 $°C/W$ and the $R_{th,jc}$ of 3.13 $°C/W$ was from datasheet [143]. For the second transistor in Half-bridge, the $R_{th,sa,2}$ became 12.767 °C/W. At current level 6 A and 8 A for Half-bridge, the thermal resistance $R_{th,ja}$ and $R_{th,sa}$ of the transistor is shown in Table 5.26.

Output diode bridge
To avoid the operating temperature increase over 175 $°C$, a thermal resistance for one diode in the output diode bridge for the Half-bridge at current level 4 A was found to be

$$R_{th,ja} = \frac{T_{j,max} - T_a}{P_{loss}} = \frac{175 - 40}{10.672W/2} = 25.299°C/W. \tag{5.105}$$

$$R_{th,sa} = R_{th,ja} - R_{th,jc} - R_{th,cs} = 25.299 - 12 - 0.8 = 12.499°C/W. \tag{5.106}$$

where the $R_{th,jc}$ of 12 $°C/W$ was obtained from datasheet [113].
At current level 6 A and 8 A for the Half-bridge, the thermal resistance $R_{th,ja}$ and $R_{th,sa}$ of the output diode bridge is shown in Table 5.26.

Transformer - selected configuration

Since calculation of the transformers operating temperature was complex, where the temperature distribution inside the transformer are considered to be vaguely, a temperature estimation needed to be established. The core loss and winding loss is turned into heat, which is dissipated in form of radiation and convection through the exposed surfaces of the transformer.

In this formula, the total losses (core and winding) are put together, and an estimation that the heat will dissipate the same amount at every surface of the core. To calculate the temperature rise ΔT, a formula was used with a built-in spread-estimation. Calculations below are made for the current level 4 A, where the temperature rise was

$$\Delta T = (\frac{P_{loss}}{A})^{0.833} = (\frac{11447mW}{53.2139cm^2})^{0.833} = 87.72255°C \tag{5.107}$$

where the value 0.833 has been derived from empirical data [108].

From this estimation the operating temperature was approximately

$$T_{operating} = \Delta T + T_a = 87.723 + 40 = 127.72°C. \tag{5.108}$$

However, this result does not include the temperature increase with time. To avoid the operating temperature increase over 155 $°C$ with time, a bigger transformer core may be preferable. For the current levels 6 A and 8 A the operating temperature for the transformer became above the temperature limit for the core, hence a larger core might be needed and calculations were not conducted with those currents. A thermal resistance for the transformer was calculated

$$R_{th,ja} = \frac{\Delta T}{P_{loss}} = \frac{87.72255}{11.447W} = 7.66336°C/W. \tag{5.109}$$

$$R_{th,sa} = R_{th,ja} - R_{th,jc} - R_{th,cs} = 7.66336 - 0.8 = 6.8633°C/W \tag{5.110}$$

where $R_{th,cs}$ is the TIM that was assumed to be 0.8 °C/W.

The thermal resistance $R_{th,jc}$ was not applicable in a transformer since the heat existed in the winding and core. Thus a $R_{th,jc}$ value was neglected.

The thermal resistance values for the other current levels in the Half-bridge is shown in Table 5.26.

Table 5.26: Thermal resistance - Half-bridge.

Half-bridge	**Rth,ja**			**Rth,sa**		
	4A	**6A**	**8A**	**4A**	**6A**	**8A**
AC/DC						
Input diode bridge	12.16	8.33	4.94	6.86	4.73	2.65
Transistor	9.91	6.79	4.03	4.11	0.99	N/A
DC/DC						
Transistor	16.697	9.26	7.06	12.767	2.48	1.26
Transformer	7.663	6.948	6.465	6.863	6.148	5.665
Output diode bridge	25.29	10.89	8.44	12.499	6.59	4.94
Total				0.714	0.248	-

In Table 5.26, the thermal resistance values were calculated for one component, for an instance, one diode in the diode bridge. The N/A written in the table is showing were a negative thermal resistance value was given, thus it was unable to find a heatsink to cool the component down rapidly enough.

With the thermal resistance values from all the components separately, they are added together in parallel, to get one thermal resistance value as shown in equation 4.46. The results are added as a row for the total $R_{th,sa}$ shown in Table 5.26.

However, for the transformer at current level 6 A and 8 A, the operating temperature is either too narrow or have exceeded the temperature limit of the core. Therefore, at these currents levels a larger transformer core is required. The size of the core depends on the cooling conditions.

5.6.2 Summary from heat calculations

The $R_{th,sa}$ values in parallel makes the total thermal resistance between heatsink to ambient for the current level of 4 A to be $R_{th,sa,tot}$=0.714 °C/W. For 6 A the $R_{th,sa,tot}$=0.248 °C/W, which resulted in a larger heatsink than desired.

5.6.3 Heatsink selection

From the calculated thermal resistance $R_{th,sa}$ values, heatsinks were selected by collected data from datasheets. A heatsink with thermal resistance close to the calculated thermal resistance value was selected.

- Size of heatsink Totem + Half-bridge 4 A (0.6): 150mm x 100mm x 15mm [159].
- Size of heatsink Totem + Half-bridge 6 A (0.23): 200mm x 200mm x 15mm [160].

These heatsinks are selected with the intent that the thickness should be thin, approximately 1-3 cm. A reasonable size of heatsink without using a fan for the

Half-bridge at the current level 4 A was obtained. For the Half-bridge with a thermal resistance value of 0.714 °C/W, a size of a heatsink became 150 x 100 x 15 mm, where having a low thickness was taken into consideration [159]. For 6 A the size of the heatsink became larger than desired. Thus, it was continued with just the heatsink at current level of 4 A.

5.6.4 Design suggestion

The final design of the heatsink is illustrated in Figure 5.20, where the high heat loads components are mounted on the surface of the heatsink. The design of the heatsink was created in Tinkercad developed by Autodesk. This size (4 A) of the heatsink was selected in subsection 5.6.3.

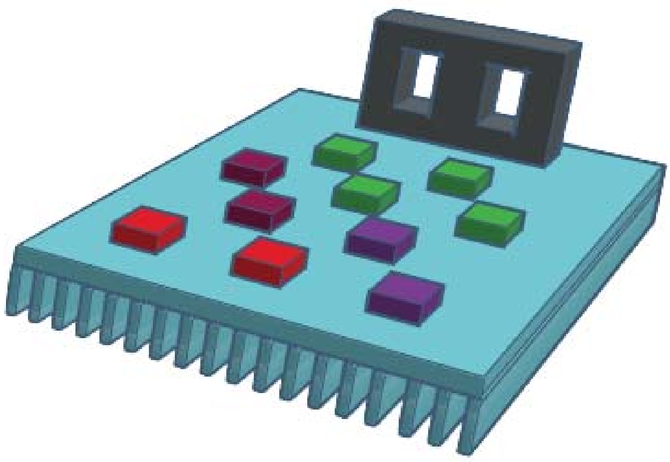

Figure 5.20: Proposed heatsink design with mounted components.

5.6.5 Heatsink simulation

With the selected topologies, the total amount of components became 18. However, only considering the components that require cooling are 11 components. These components are mounted on the back of the heatsink. The simulation setup is based on the selected heatsink from ABL Components. The dimension was selected to be H=15 mm, L=150 mm and W= 100 mm. A total of N=18 fins, where b=4 mm is the thickness of the base plate of the heatsink, and the size of each fin is estimated to be t=2 mm [159], [162]. This is graphical presented in Figure 5.21.

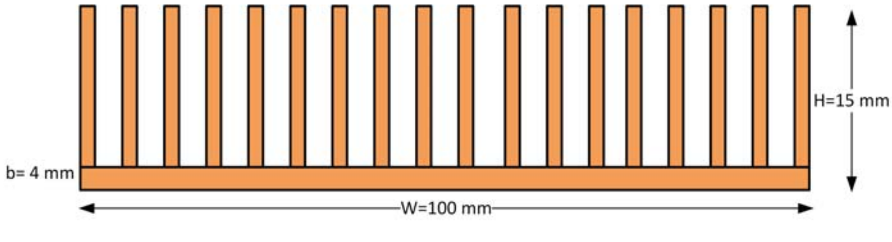

Figure 5.21: Dimension of selected heatsink with mounted components.

The material selection was anodized aluminum (6063-T6), thus the surface emissivity was assumed to be 0.85 [163]. Natural convection was selected for this test. The junction to case thermal resistance R_{th-jc} was selected from data sheet. It should be noticed that this test was simulated during one cycle, implying the all components in the bridge should have power dissipation. This is since the current flow is alternating between each pair of the diodes at the frequency of the current. The maximum temperature limit is 175 °C for the diodes, 150 °C for the MOSFETs and 155 °C for the transformer core. Various TIM was tested with insignificant impact on the result [161]. Thus, a TIM with 0.18 mm thickness an a thermal conductivity 1.2 W/mk was selected. This heatsink with the components are presented with heatsink-base temperature and heat radiation shown in Figure 5.22.

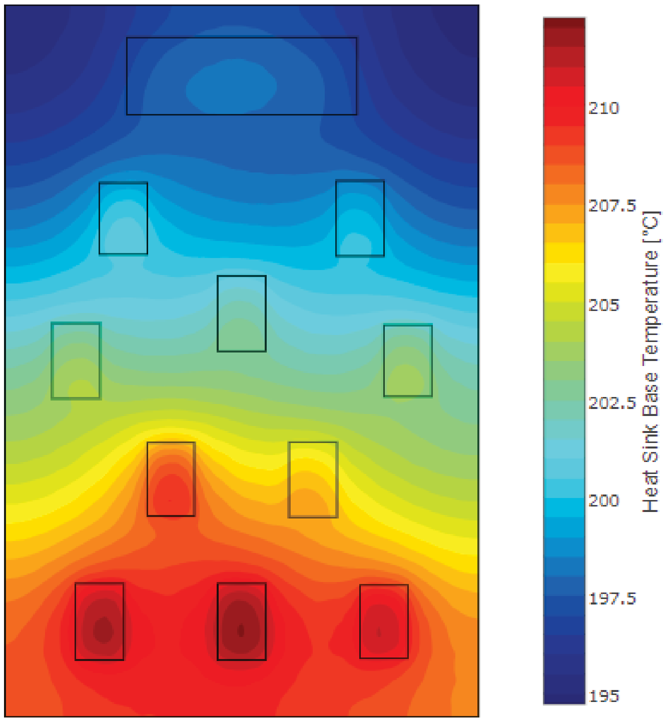

Figure 5.22: Heatsink simualtion without fan.

The temperature of the components with natural cooling exceeded their maximum limits, is listed in Table 5.27.

Table 5.27: The temperature of the components with natural cooling.

Power source	T_{avg} [°C]	T_{max} [°C]
Transformer	291	292
Totem MOSFET 1	277	278
Totem MOSFET 2	277	277
Totem Diode 1	269	270
Totem Diode 2	271	272
Half-bridge MOSFET 1	227	228
Half-bridge MOSFET 2	230	231
Half-bridge Diode 1	272	273
Half-bridge Diode 2	271	272
Half-bridge Diode 3	275	276
Half-bridge Diode 4	268	269

To possibly mitigate these high temperatures, a simulation with natural convection included with a larger heatsink size was conducted. The heatsink size was increased from 100 x 150 x 15 mm to 200 x 200 x 25 mm. Although, even with the increased size, the temperature of the components exceeded their limits as well. Additionally, it was observed that this heatsink was larger than desired module for the off-board charger. The results of this simulation are shown in Figure E.1 and Table E.1 in Appendix E.

Thus, simulation with forced cooling needed to be tested. With a fan implemented to the heatsink, the temperature levels reduced rapidly, as shown in Figure 5.23. Each fan was regulated to a speed of approximately 3.9 m/s, by use of assumed installed speed fan software inside the LV board system. The fan size is 30 mm in diameter [164]. It is assumed that LV system inside the charger is supplying the fan with 12 V DC.

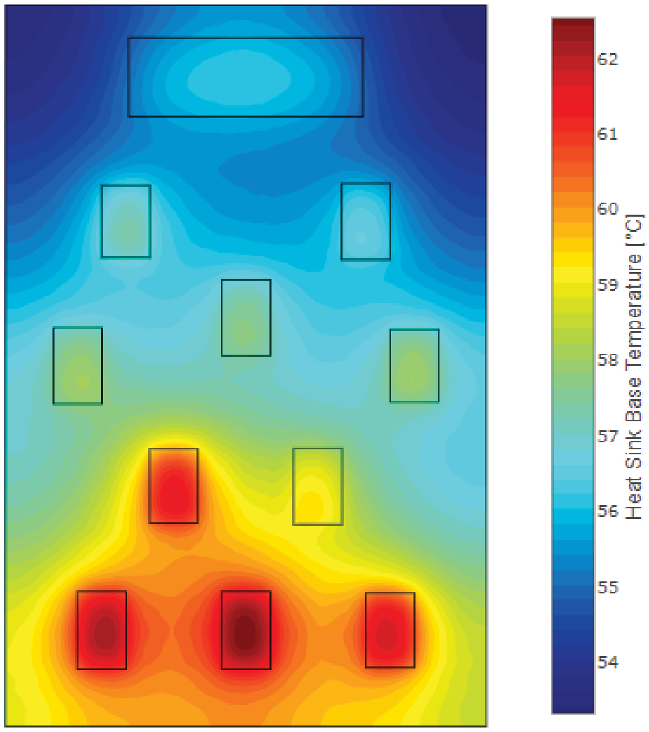

Figure 5.23: Heatsink simulation with fan.

Where the components temperature is shown in Table 5.28.

Table 5.28: Temperature of the components with forced cooling.

Power source	T_{avg} [°C]	T_{max} [°C]
Transformer	149	150
Totem MOSFET 1	128	128
Totem MOSFET 2	127	128
Totem Diode 1	122	122
Totem Diode 2	122	122
Half-bridge MOSFET 1	84	84.4
Half-bridge MOSFET 2	84.7	85.1
Half-bridge Diode 1	127	127
Half-bridge Diode 2	126	127
Half-bridge Diode 3	128	128
Half-bridge Diode 4	125	126

As shown in the table, the components temperature is now within the respective components maximum limits.

5.7 Final design

For the final design of the module, the HV system consisted of an AC/DC converter with Totem-pole PFC and a DC/DC Half-bridge converter. The LV circuit board was estimated to be 40 g to find an applicable size same as the heatsink [165].

Three fans were selected and mounted at one side of the heatsink in order to ensure that the wind speed is distributed equally over the heatsink. One fan was considered as well, however, it required too much space in the design. The heatsink is functioning as the roof to enclose the module. The diodes, transistors, and transformer are connected to the circuit board with isolating wires that are twisted together to mitigate the EMI that might appear. Furthermore, the components could be mounted closer to each other to minimzed the interference more.

Regarding the efficiency and power losses. The OBC has an efficiency of 92 % at 4 A, while the off-board charger obtains 94 %. To illustrate graphically how the final module could look like, the electric power components are mounted on a printed circuit board (PCB) and on the heatsink. The proposed module of the off-board charger is shown in Figure 5.24.

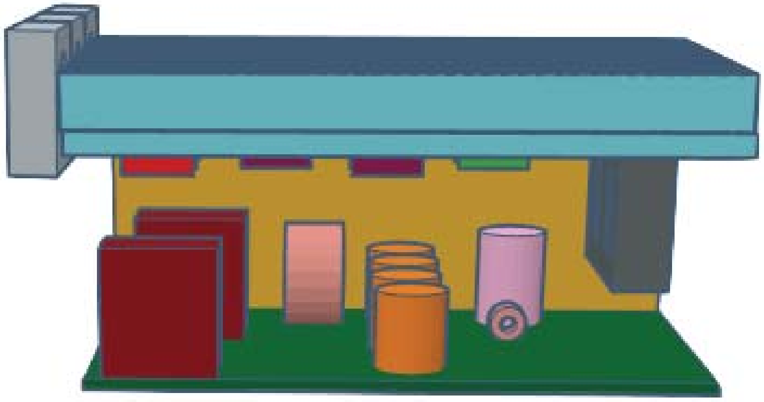

Figure 5.24: The proposed module of off-board charger.

The circuit diagram of the proposed off-board charger is shown in Appendix A in Figure A.2.

By including LV circuit board, 40 g, the 4 m cable with the desolate module from Mennekes, 1640 g, 3 connectors, 291 g, 3 fans, 21.78 g, heatsink 344 g, power electronics including the 2 EMI-filters 207 g, and enclosed walls of the module, estimated to be 257 g, gave a total weight of 280.78 g = 2.8 kg of the off-board charger. The module itself has a weight of 1160.78 g=1.16 kg.

Since both OBC and the charging cable from Mennekes are utilizing IP67 as ingress protection, it was assumed that this off-board charger is equipped with IP67 as well.

Compared to the weight of power electronics components in the OBC, the components in the off-board charger were 87 % reduced in weight. In relation to the cooling system, it was 59 % minimized in weight. The total weight of the off-board charger was 30 % reduced. While the volume of the module itself was 69 % smaller than the

OBC. The size comparison is shown in Figure 5.25.

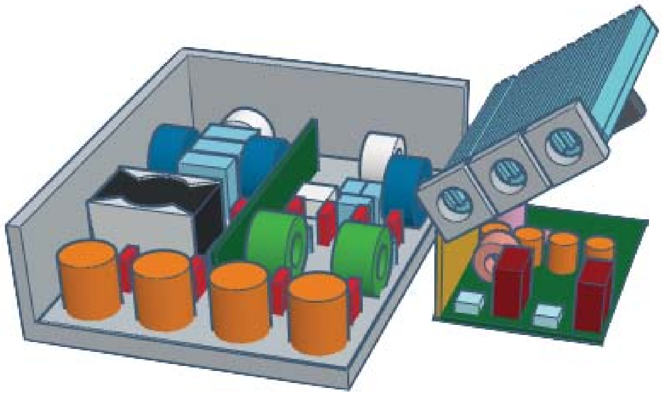

Figure 5.25: Comparison between OBC and the off-board charger module.

A charger with a 4 A input was more preferable to obtain the smallest possible size. The final design specification for this selected off-board charger are listed as:

- Power input: P_{in}= 978.26 W
- Power output: P_{out}= 923.68 W
- AC/DC switching frequency: f_{sw} = 150 kHz
- DC/DC switching frequency: f_{sw} = 200 kHz
- Total harmonic distortion: THD = 12.21 %
- Power factor: PF= 0.954
- Efficiency: η=94.42 %
- Total weight: 2.8 kg (1.64 kg cable + 1.16 kg module)
- Cable length: 4 m
- Estimated dimension (without enclosure): 16 x 10 x 6.4 cm
- Estimated volume (module): 1024 cm^3
- Power density = 923.68 W/2.8 kg
- Cooling system: Heatsink with 3 fans
- Ingress protection: IP67

5.8 Nozzle design

To deliver DC from the nozzle to the EVI of the vehicle, the design of the nozzle was needed to have a proper interface configuration. Since this charger was designed for the European market, it was likely to use a similar interface configuration arrangement that is represented in row two, type 2 for DC connectors shown in Table 4.9. Since the communication protocol between the HV battery and OBC existing today is utilizing CAN-bus, it was assumed to use CAN communication as protocol as well as for the off-board charger. This would simplify the communication between the charger and the HV battery. Thus, this type of connector has a total of four contacts: 2 power contacts (+DC and -DC) and two communications pins (CAN+ and CAN-). The pin configuration for the charger is shown in Figure 5.26.

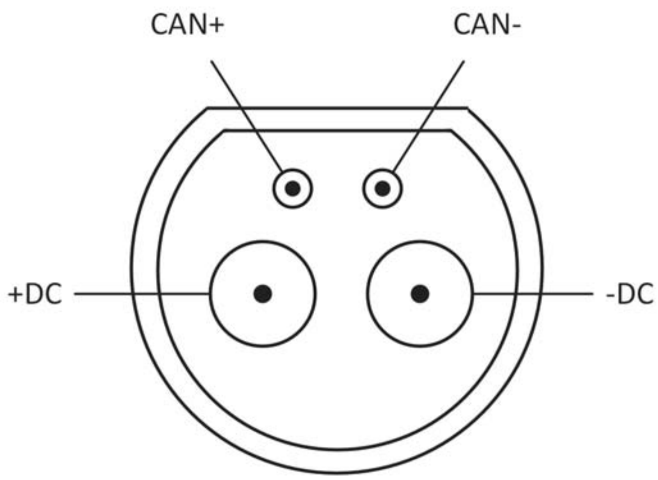

Figure 5.26: Feasible nozzle design connector with the pin configuration for the off-board charger.

A simplified schematic of how the new arrangement for how the final charger can be integrated with the vehicle is illustrated in Figure 5.27, where CAN communication is utilized.

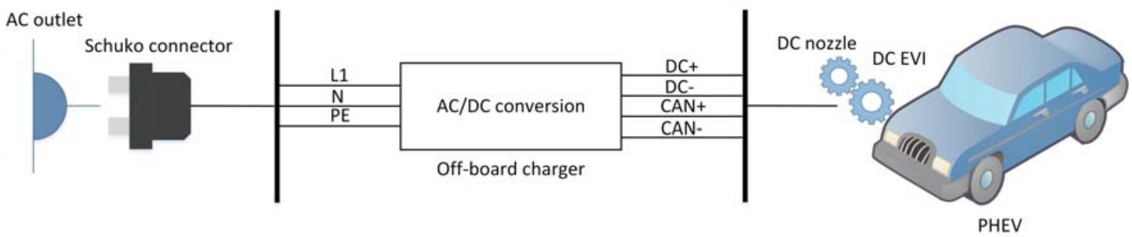

Figure 5.27: Data communication in the off-board charger integrated between a wall socket and a PHEV.

To summarize the working operation of the off-board charger: from the AC power outlet, the charger is connected with a schuko connector. The AC power is transferred along the cable to the conversion module where the AC is converted to DC. The DC power including communication data through, CAN+ and CAN-, are transmitted to the DC nozzle. The nozzle is connected to the EVI of PHEV, where the DC power charging the HV battery. This established communication line between the battery and the charger is vital since the charger needs to know when to start and abort the charging process. The CAN bus system is initiated as soon as the HV battery approves the established line. This is based on subsection 4.7.5.

6

Discussion

6.1 Electrical performance

In accordance with standard regulations and the desired target design specification, the off-board charger passes most of the parameters. For 4 A, the PF became 0.954 with an efficiency of 94.42 %. This efficiency was similar in comparison to the OBC. However, the THD became 12.21 % and exceeded the allowed limit. This was likely due to distortion in the input current, which indicated that PFC was not optimized and since the fact that filter was not implemented to the simulation. However, it was observed that THD is decreasing with a higher current, simultaneously gave a higher PF. Compared to the design specification of the OBC, a higher PF was obtained with 8 A input.

Since the HV battery was not simulated, the duty cycle was fixed. However, it might have affected the results for both simulation and calculations since the charging level of the battery might have required a varying duty cycle. This would likely have increased the power dissipation in the components with a duty cycle that is active during an extended time.

It was noticed that the output voltage is decreasing with higher current, which was unexpected since the components were designed for a constant voltage. However, this can be due to the selected IC PFC controller can only obtain a maximum output power of 1500 W. This implied that when the output power was approaching this limit, the voltage and current started to decrease. For the case with 4 A, it appeared to show reasonable output from all converters. This suggested that a different IC PFC was needed to be implemented for higher currents.

Since the simulation parts was not connected together, there might have been some deviation in the results due to an existing ripple that was generated from the AC/DC stage. However, this ripple is assumed to be removed from the DC/DC converter stage. The simulation results in DC/DC converter could also be improved by implementing an ideal diode bridge controller that improves the efficiency and mitigate the power dissipation.

In comparison to the OBC that has a power density of 1 kW/kg, the off-board charger reached a power density of 924 W/2.8 kg with 4 A input. Since it was proved that a higher current resulted in increased weight, the input current might need to be decreased in order to reduce the weight further. However, this would likely extend the charging time of the HV battery.

Since EMI levels were not investigated in this project, and the selected switching frequencies and their harmonics affected the EMI levels, it was not possible to foresee how many filters were required for the charger. To determine the number of filters, it is likely that a prototype needs to be built in order to actually measure and study the noise spectrum more accurately. By then, it would be possible to design a sufficient filter system for the charger.

Since the cost was not considered to be priority, the selection of the topologies towards the final charger might have been different. This would likely not change the size and weight significantly since these data are similar.

6.2 Heat and thermal losses

Calculations for some heat dissipating components were complicated and in certain cases difficult to make correct assumptions. One example of this could be how the heat within a transformer was being distributed. Another example can be how large safety margin is required in regard to the temperature inside the charging module compared to the ambient temperature.

The transformer's operating temperature at current levels 6 A and 8 A, were above the temperature limit for the core, and could therefore not calculate results for a heatsink size.

Transistors belongs to one of the most heat dissipating components, and the calculations were based on information from datasheets. However, since the shortage of time, the most optimal components might not have been found. Hence measurements on a prototype model will be necessary.

If LTspice offered more variety of components, $R_{DS(on)}$ could have been considered, since it was more favorable to have $R_{DS(on)}$ to be as low as possible to reduce conduction losses. However, it should be noted that a too low $R_{DS(on)}$ leads to higher switching losses.

It was necessary to have fans towards the heatsink to obtain an optimal cooling effect, which gave a 21 dB level in noise during operation. This noise level was low; therefore it would not be treated as a distraction object. However, it should be taken into consideration that a small fan generates higher noises than compared to a larger fan. Additionally, it should be highlighted that a fan with wider diameter, would transmit a higher amount of air. Furthermore, a survey of other external charger should be conducted to analyze what other cooling implementation are utilized, and in that case, if these cooling alternative are accordingly to international standards.

The heatsink was placed as a roof on the off-board charger module, for the heat to distribute better. However, since forced cooling was needed, the placement of the heatsink can be relocated as a wall instead. In that case, it could have been possible to shorten the wires between transistors/diodes and the circuit board. Moreover, since other cooling implementation was not considered, a deeper study is required to analyze what cooling implementation alternative could be utilized for external charging.

6.3 Weight and size

A comparison between the OBC, the size of the module from charging cable from Mennekes (blue rectangle) and the proposed off-board charger design size (red rectangle) is shown in Figure 6.1. Concerning the weight, the Mennekes cable had a total weight of 1.9 kg, while the off-board charger had a weight of 2.8 kg. That is corresponding to a 32 % weight reduction.

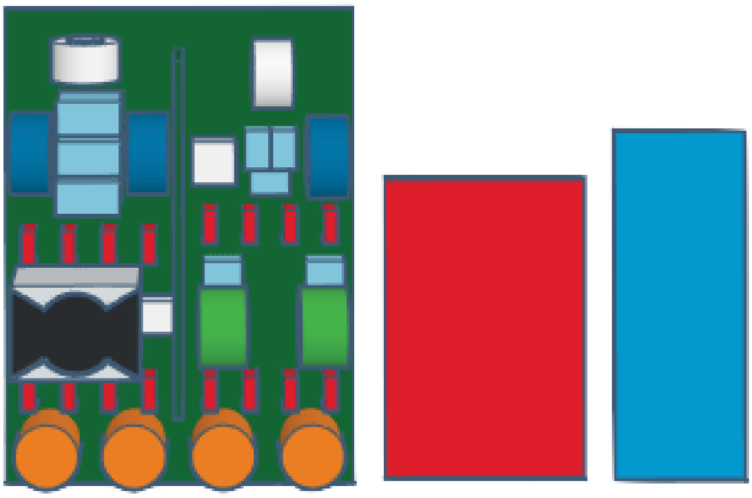

Figure 6.1: Comparison between size design. From left to right: OBC, off-board charger and module from Mennekes.

Regarding to their dimensions, they are listed as follows:

- OBC: 6.8 x 19.2 x 25.5 cm (3329.28 cm^3)
- Off-board charger module: 16 x 10 x 6.4 cm (1024 cm^3)
- Mennekes module: 5.2 x 24 x 10 cm (1248 cm^3)

From the list, it is observed that module for the off-board charger became larger in size compared to the reference design. However, the selected heatsink was "off the shelf", which required a customized heatsink design size close to the aimed size. To decrease the volume of the design further, a fan with higher wind speed could be implemented, thus it would presumably be that a smaller sized heatsink is required.

It was observed from the results that a higher input current supplied to charger increased the weight and volume of the power electronics components. Thus, by reducing the input current, to 1-2 A instead, would likely result in an even smaller design. However, this might extend the charging time and decreased the efficiency.

Another suggestion to reduce the size further of the module is to increase the switching frequency to 350 kHz for the DC/DC converter. This might have worked, but it would likely result in higher switching losses and larger distortion. Furthermore, it might be feasible to research if an inverter could only be implemented after the DC-link to charge the HV battery. This implies that galvanic insulation may not be required, and it would probably reduce, size, weight and losses significantly of the charger. However, further investigation regarding the safety without this isolation is desirable.

7

Conclusion

This research investigated if it was possible to relocate the OBC from a PHEV and redesign it into a compact AC/DC module for a portable off-board charger, in order to save space and weight inside the vehicle. With all the assumptions and estimations made within this project, it was concluded that is was feasible to design a 4 A off-board charger with having size and weight of 1024 cm^3 respectively 2.8 kg. This charger was 30 % respectively 69 % smaller in weight and size compared to the Geely OBC. Comparing only the module itself with the OBC, there is a weight reduction of 71 %. Thus, it was relatively close to the aimed charger from Mennekes in terms of size. With the selected topologies for the power electronic system, resulted in an efficiency of 94.42 %, a power factor of 0.954, and THD level of 12.1 %. This gave a maximized output power of 924 W.

The cooling system was 59 % lighter in weight compared to OBC, where both a heatsink and forced convection, in forms of fans, has been implemented to mitigate high heat levels below 150 °C and thereby avoiding damages on the power electronic components.

7.1 Future work

Concerning alternative cooling implementation, one future work could be to utilize the chassis of the vehicle itself as a cooling surface for the external charger. This would imply that it is not possible to have an active cooling system (fans or pump). Thus, a passive system would be appropriate to use during the charging process. The principal is to attach the module of the off-board charger to the vehicle, as close as possible to a cooling surface. A heat absorption area is collecting all heat dissipation and distribute it along cooling pipes with coolant to the cooling end. A suspension system could be used to press the cooling end against the surface to maximize the cooling effect. This charger would likely to have only one cable from the outlet since a cable between the module and the EVI means that the thermal dissipation needs to travel a long distance and that pipes would result in a larger cable. Depending on how effective this is, it may work for an external charger with a higher power level.

A small investigation of narrowed AC/DC and DC/DC converters was conducted. However, it would be interesting to do a larger review of different topologies to find a more optimal circuit. In that case, the cost could be taken into consideration.

Since the weight of the off-board charger is heavier than the Mennekes charging cable, due to it is designed for an input current between 4-8 A, an investigation is required to further analyze if the cable itself could be minimized. For an example, the cross-sectional area could be designed for a current level of 4 A. Another suggestion could be to reduce the length of the cable, as it may not be necessary to have a 4 m. In a need of a longer cable length, an extension cord could be attached. Hence, a lighter weight might be obtained. Furthermore, to decrease the number of components even further, the diodes and transistors included in the bridges could be replaced with IC-circuits to save more space and weight.

Furthermore, an investigation of material such as silicon carbide (SiC) and gallium nitride (GaN) to the switching devices is needed since the cooling can be reduced because of their higher efficiency.

The components should have been selected with more caution to ensure that the selected components in calculations and simulation are the same to obtain more accurate results. To reduce the switching on losses, a zero-voltage switching (ZVS) circuit could be implemented in LTspice for the Full- and Half-bridges. Regarding the thermal analysis, an advance software like COMSOL Multiphysics could be utilized instead for Heatsinkcalculator. This would likely give a higher accuracy since COMSOL offer more options and tools. Additionally, an investigation could be conducted if other types of heatsink could be implemented and how that would affect the thermal analysis result.

Another continuation of this project could be to construct a prototype of the proposed charger, to observe if it could be implemented into reality. Also, to measure the power losses from the prototype instead of using estimation calculations. Since the charger is outside the vehicle, it is vital that the enclosure is designed to be robust and impact resistance. For an instance, the charging cable from Mennekes is designed to resist a weight up to 500 kg.

A final future work suggestion could be to analyze how long the charging time would be with this charger, where a battery model could be simulated in LTspice. This model should be modeled to be equivalent to an HV battery for a PHEV. Alternatively, if the prototype is constructed, the charger could charge an authentic HV battery.

Bibliography

[1] International Energy Agency (2017), ”Global EV outlook 2017,” Figure (1,5), [Online]. Available: https://www.iea.org/publications/freepublications/publication/GlobalEVOutlook2017.pdf, (2018-01-22).

[2] Buchmann, I. (2017), Battery university, ”BU-1003: Electric Vehicle (EV),” Table (1), [Online]. Available: http://batteryuniversity.com/learn/article/electric_vehicle_ev, (2018-01-22).

[3] Monteiro, V., Gonçalves, H., Ferreira, J. C. and Afonso, J.L. (2012), ”Batteries Charging Systems for Electric and Plug-In Hybrid Electric Vehicles,”, University of Minho, Guimarães, Portugal [Online]. Available: https://repositorium.sdum.uminho.pt/bitstream/1822/21076/1/InTech_2012_BCS_EV_PHEV.pdf, (2018-01-22).

[4] Nowakowski, R. and King, B (2006), ” Choosing the optimum switching frequency of your DC/DC converter ” [Online]. Available: https://www.eetimes.com/document.asp?doc_id=1272335 (2018-03-29).

[5] Williams, D (2017). All About Circuits ”Understanding Total Harmonic Distortion (THD) in Power Systems,”, [Online]. Available: https://www.allaboutcircuits.com/technical-articles/understanding-thd-total-harmonic-distortion-in-power-systems/, (2018-01-25).

[6] Mohan, N., Undeland, T. M and Robbins W. P. ”Power Electronics: Converters, Applications, and Design 3rd Edition (2002), Wiley, USA ”, [Online]. Available: https://http://uni-site.ir/khuelec/wp-content/uploads/Mohan-Power-Electronics.pdf, (2018-01-25).

[7] Williams, D. (2016), ”Power Factor, THD, and Why Linear Power Supplies Fail to Meet Power Standards” [Online]. Available: https://www.allaboutcircuits.com/technical-articles/power-factor-thd-why-linear-power-supplies-fail-meet-electricity-standards (2018-01-29).

[8] Elsäkerhetsverket (2017), ”Elsäkerhetspocket - råd till dig som gör enklare elarbeten hemma.” [Electronic]. Värmland, Kristinehamn, Sweden (2018-04-29).

[9] Blomhäll, T. (2016), ”Elbilsskolan: Så fungerar laddaren i elbilar” [Online]. Available: http://www.mestmotor.se/recharge/artiklar/artiklar/20160927/elbilsskolan-sa-fungerar-laddaren-i-elbilar (2018-01-29).

[10] Chau, K.T. (2016), Energy Systems for Electric and Hybrid Vehicles, The Institution of Engineering and Technology [Electronic]. London, United Kingdom, 2016. (2018-02-02).

[11] Jonsson, R., ”LADDNING AV ELBILAR I BOSTADSRÄTTEN 1,0” HSB Riksförbund, 2016 [Online]. Available: https://www.hsb.se/globalassets/gemensamt-innehall/media/andra-trycksaker/laddning-av-elbilar-i-bostadsratten-10-20160430.pdf, (2018-01-22).

[12] Haghanipour, M., ”1.2. Snabbladdning?” Power Circle AB, Stockholm, Sweden [Online]. Available: http://emobility.se/startsida/laddstationsguiden/forberedelser/1-2-snabbladdning-eller-normalladdning/, (2018-01-22).

[13] Mossig, M. R. (2000), ”NF A14 Industrialppc 2000 IP67 PWM” Wien, Austria [Online]. Available: https://noctua.at/en/nf-a14-industrialppc-2000-ip67-pwm, (2018-01-22).

[14] Persson, S. H. (2018), ”Vanrar för att ladda bilen hemma”, Aftonbladet [Online]. Available: https://www.aftonbladet.se/bil/a/m60yX0/varnar-for-att-ladda-bilen-hemma (2018-03-18).

[15] J. Kristensson (2018), ”Nya krav ska soppta brandfarlig laddning”, Janurary 28. Available: https://www.nyteknik.se/ (2018-03-18).

[16] Ivanov, D., Moller, H. and Dew, J. (2017), ”Convenience of home charging compared to filling up with petrol”, Flipthefleet, [Online]. Available: http://flipthefleet.org/2017/convenience-home-charging-compared-filling-petrol-1-click-survey-10/ (2018-03-21).

[17] Kristensson, J. (2018), ”Så ska elsystemet klara elbilsrevolutionen”, Janurary 28. Available: https://www.nyteknik.se/ (2018-03-18).

[18] Plugin cars (2018), ”Compare Electric Cars and Plug-in Hybrids By Features, Price, Range”) [Online]. Available:http://www.plugincars.com/cars?field_isphev_value_many_to_one=electric+2B+gasoline (2018-02-09).

[19] Pan, L. and Zhang, C. (2016), ”An Integrated Multifunctional Bidirectional AC/DC and DC/DC Converter for Electric Vehicles Applications,”, China, June 2016 [Online]. Available: http://www.mdpi.com/1996-1073/9/7/493/htm (2018-04-03).

[20] Chau, K.T. (2016), ”Energy Systems for Electric and Hybrid Vehicles”, [Electronic image] (2018-04-14).

[21] Hirota, M., Baba, T., Zheng, X., et. al. (2011), ” Development of New AC/DC Converter for PHEVs and EVs”, SEI Technial [Electronic]. Available: http://global-sei.com/technology/tr/bn73/pdf/73-11.pdf (2018-02-18).

[22] Sridhar, A. R. P. A. (2009), ”Bidirectional AC-DC Converter for Vehicle-to- Grid (V2G) Applications”, Marquette University, [Online]. Available:https://epublications.marquette.edu/cgi/viewcontent.cgi?article=1333&context=theses_open (2018-02-29).

[23] Sridhar, A. R. P. A. (2009), ”Bidirectional AC-DC Converter for Vehicle-to- Grid (V2G) Applications”, Marquette University, [Electronic image]. Available:https://epublications.marquette.edu/cgi/viewcontent.cgi?article=1333&context=theses_open (2018-02-29).

[24] Williams, D. (2016), ”How the Boost PFC Converter Circuit Improves Power Quality ” [Online]. Available: https://www.allaboutcircuits.com/technical-articles/

how-the-boost-pfc-converter-circuit-improves-power-quality/ (2018-02-27).
[25] Williams, D. (2016), ” Design of Power Factor Correction Using FAN7527” [Online]. Available: http://www.onsemi.com/pub/Collateral/AN-4107.pdf.pdf (2018-03-03).
[26] Texas Instruments Incorporated (2016), ” UCC28180 Programmable Frequency, Continuous Conduction Mode (CCM), Boost Power Factor Correction (PFC) Controller” [Electronic]. Available: http://www.ti.com/lit/ds/symlink/ucc28180.pdf. (2018-03-03).
[27] Williams, D. (2016), ”How the Boost PFC Converter Circuit Improves Power Quality” [Electronic image] Available:https://www.allaboutcircuits.com/technical-articles/how-the-boost-pfc-converter-circuit-improves-power-quality/ (2018-03-16).
[28] Texas Instruments Incorporated (2018), ”98.5% Efficiency, 6.6-kW Totem-Pole PFC Reference Design for HEV/EV Onboard Charger” [Electronic]. Available:http://www.ti.com/lit/ug/tidue54/tidue54.pdf (2018-03-19).
[29] Chidley, A. (2018), ”Selecting DC-link capacitors in power converters” [Online]. Available:https://www.avnet.com/wps/portal/abacus/resources/engineers-insight/article/selecting-dc-link-capacitors-for-power-converters (2018-03-21).
[30] Erickson, R. W. (2007), ”DC-DC Power Converters”, University of Colorado [Online]. Available: http://www.eng.auburn.edu/~agrawvd/COURSE/READING/LOWP/Erikson_DC_2_DC.pdf (2018-02-23).
[31] Texas Instruments Incorporated (2014), ”Phase-Shifted Full Bridge DC/DC Power Converter Design Guide ”, [Online]. Available: http://www.ti.com/lit/ug/tidu248/tidu248.pdf (2018-02-20).
[32] Arya, P.S and Chithra, R. (2015), ”Phase Shifted Full Bridge DC-DC Converter”, International Research Journal of Engineering and Technology [Online]. Available: https://www.irjet.net/archives/V2/i4/Irjet-v2i4288.pdf (2018-02-20).
[33] Bourgeois, J. M. (1999), ”Circuit for power factor correction with regards to mains filtering” [Electronic]. Available:http://www.st.com/content/ccc/resource/technical/document/application_note/fc/ba/b1/89/1f/52/49/7e/CD00003915.pdf/files/CD00003915.pdf/jcr:content/translations/en.CD00003915.pdf (2018-03-12).
[34] Gautam, D. S., Musavi F., Edington, M. (2012), ”An Automotive Onboard 3.3-kW Battery Charger for PHEV Application”. Vol. 61, no. 8, 3468. IEEE publishing, transactions on vehicular technology. October 8, 2002 (2018-03-12).
[35] Jang, Y., Jovanović, M.M., Jang, Y. et. al. (2016), ”Implementation of 3.3-kW GaN-Based DC-DC Converter for EV On-Board Charger with Series Resonant Converter that Employs Combination of Variable-Frequency and Delay-Time Control”. IEEE publishing, February, 2006 (2018-03-12).
[36] Ngyen, V-L., TRAN-QUOC, T., Bacha, S (2013). ”Harmonic Distortion Mitigation for Electric Vehicle Fast Charging Systems” IEEE publishing, June, 2013 (2018-03-12).

[37] Kongsberg Automotive (2017), " EMC System and Component Test Plan for OBC", Gothenburg: EMC. (EMC report: Test Specification) (2018-02-19).

[38] Pan, L. and Zhang, C. (2016), "An Integrated Multifunctional Bidirectional AC/DC and DC/DC Converter for Electric Vehicles Applications", Beijing Institute of Technology, Beijing, China [Online]. Available:https://pdfs.semanticscholar.org/3845/9a7ad321a7d6d739f6bac7e55b1a2cc1072e.pdf, (2018-01-22).

[39] Mohan, N., Undeland, T. M and Robbins W. P.(2002), " Power Electronics: Converters, Applications, and Design 3rd Edition " [Electronic image]. Available: https://http://uni-site.ir/khuelec/wp-content/uploads/Mohan-Power-Electronics.pdf. (2018-03-21).

[40] Jayant Baliga, B. (2018), " What is the Difference Between MOSFET and IGBT", [Online]. Available: http://www.apogeeweb.net/article/66.html. (2018-03-20).

[41] Bausch, J. (2011). " MOSFET vs. IGBT.", [Online]. Available: https://www.electronicproducts.com/Analog_Mixed_Signal_ICs/Discrete_Power_Transistors/MOSFET_vs_IGBT.aspx (2018-03-21).

[42] Blake, C. and Bull, C. "IGBT or MOSFET: Choose Wisely" [Online]. International Rectifier. Available: https://www.infineon.com/dgdl/choosewisely.pdf?fileId=5546d462533600a40153574048b73edc. (2018-03-21).

[43] PNTpower (2015), " MOSFET or IGBT: To great power, comes great responsibilities " [Online]. Available: https://www.pntpower.com/mosfet-or-igbt-to-great-power-comes-great-responsibilities/. (2018-03-21).

[44] . Thornton, S. (2017), "MOSFETs: What is RDS(on)?" [Online]. Available: https://www.microcontrollertips.com/mosfets-what-is-rdson-faq/ (2018-03-29).

[45] Rahman, S.A. (2013), " CCM PFC Boost Converter Design " [Electronic]. Infineon Technologies publishing, North America. Available: https://www.mouser.com/pdfdocs/2-7.pdf (2018-03-21).

[46] Future Electronics, " What is an Ultrafast Rectifier? " [Online]. Available: http://www.futureelectronics.com/en/diodes/ultrafast-rectifiers.aspx. (2018-03-27).

[47] STMicroelectronics (2018), " Silicon Carbide Diodes " [Online]. Available: http://www.st.com/en/diodes-and-rectifiers/silicon-carbide-diodes.html?querycriteria=productId=SC489. (2018-03-27).

[48] Future Electronics, " What is an EMI Filter? " [Online]. Available: http://www.futureelectronics.com/en/filters/emi-filter.aspx (2018-03-29).

[49] Hesener, A. (2011), " Electromagnetic Interference (EMI) in Power Supplies " [Electronic]. Available: https://www.fairchildsemi.com/technical-articles/Electromagnetic-Interference-EMI-in-Power-Supplies.pdf (2018-03-20).

[50] Murata, " Differential and Common Mode Noise " [Online]. Available: https://www.murata.com/~/media/webrenewal/products/emc/emifil/knowhow/26to30.ashx (2018-03-29).

[51] Schaffner (2013), ”EMC/EMI Filter Design with RB Common-Mode Chokes ” [Electronic]. Available: https://www.schaffner.com/fileadmin/media/downloads/application_note/Schaffner_AN_RB_common_chockes.pdf (2018-03-29).

[52] Danilovic, M., Luo, F., Xue, L. et. al (2012), ”Size and weight dependence of the single stage input EMI filter on switching frequency for low voltage bus aircraft applications ” IEEE publishing, September, 2012 (2018-03-12).

[53] Bocock, G (2016), ” How to reduce size and increase performance in AC/DC power supply design” [Online]. Available:https://www.xppower.com/Portals/0/pdfs/BetterAC-DCDesign.pdf (2018-03-29).

[54] Gautam, D. S., Musavi F., Edington, M. (2012), ”An Automotive Onboard 3.3-kW Battery Charger for PHEV Application” [Electronic image]. Available: https://ieeexplore.ieee.org/stamp/stamp.jsp?tp=&arnumber=6043192 (2018-03-29).

[55] Azazi, H.Z., EL-Kholy, E.E., Mahmoud. S.A. and S.S.Shokralla (2010), ”Review of Passive and Active Circuits for Power Factor Correction in Single Phase, Low Power ACDC Converters” IEEE publishing, December 19-21, 2010 (2018-04-05).

[56] Oruganti, R. and Shrinivasan, R. (1997), ”Single phase power factor correction - A review ”, [Electronic] (2018-04-07).

[57] Guerra, M. (2015), ”What’s the Difference Between Passive and Active Power-Factor Correctors? ” [Online]. Available: http://www.electronicdesign.com/power/what-s-difference-between-passive-and-active-power-factor-correctors (2018-04-01).

[58] Starline, ”Neutral Ratings For Power Distribution Systems in the Data Center” [Online]. Available: http://cmbuck.com/wp-content/uploads/2014/12/Neutral-Ratings-for-power-busway-distribution.pdf, (2018-02-09).

[59] Guerra, M. (2015), ”What’s the Difference Between Passive and Active Power-Factor Correctors? ” [Online]. Available: http://www.electronicdesign.com/power/what-s-difference-between-passive-and-active-power-factor-correctors (2018-04-07).

[60] Rouse, M. (2005), ”PFC (power factor correction or power factor controller)” [Online]. Available: https://whatis.techtarget.com/definition/PFC-power-factor-correction-or-power-factor-controller. (2018-04-02).

[61] Linear Technology Corporation (1993), ”LT1248 - Power Factor Controller” [Electronic]. McCarthy Blvd., Milpitas, CA, USA. LT Publishing. Available: http://www.analog.com/media/en/technical-documentation/data-sheets/1248fd.pdf (2018-02-29).

[62] Texas Instruments Incorporated (2017), ”Power factor correct (PFC) basics and design considerations - 3.1 Power factor correction (PFC) topology comparison” [Video]. Available: https://training.ti.com/power-factor-correction-pfc-topology-comparison?cu=1134305 (2018-03-07).

[63] Loughlin, M. O' (2017), "Phase Management Raises Interleaved PFC Efficiency" Available: http://www.powerelectronics.com/power-management/phase-management-raises-interleaved-pfc-efficiency (2018-03-07).
[64] Dusmez, S (2017), "High volt interactive - Designing a 99% Efficient Totem Pole PFC with GaN" (2018-03-07).
[65] Rozenblat, L. (2013), "Design of CCM power factor correction boost converter" [Online] Available: Available: http://www.powerfactor.us/ccm-pfc-boost.html (2018-03-07).
[66] Schott, G. (2017), "Totem Pole PFC with GaN and SiC" [Electronic image]. Available: https://www.kivi.nl/uploads/media/59565ab464588/Guido-Schott.pdf (2018-03-15).
[67] NXP Semiconductors (2016), "Totem-Pole Bridgeless PFC Design Using MC56F82748" [Electronic]. Available: https://www.nxp.com/docs/en/reference-manual/DRM174.pdf (2018-03-19).
[68] Texas Instruments Incorporated (2018). "98.5% Efficiency, 6.6-kW Totem-Pole PFC Reference Design for HEV/EV Onboard Charger" [Electronic]. Available:http://www.ti.com/lit/ug/tidue54/tidue54.pdf (2018-03-29).
[69] Rahman, S.A., Stückler, F. and Siu, K. (2016), "PFC boost converter design guide " [Electronic]. Infineon Technologies publisher, Munich, Germany. Available: https://www.infineon.com/dgdl/Infineon-ApplicationNote_PFCCCMBoostConverterDesignGuide-AN-v02_00-EN.pdf?fileId=5546d4624a56eed8014a62c75a923b05 (2018-03-15).
[70] Texas Instruments Incorporated (2016), "1-kW, Compact, 97.5% Efficiency, Digital PFC for AC/DC PSUs With eMeter Reference Design " [Electronic]. TI publisher. Available: http://www.ti.com/lit/ug/tidubk8b/tidubk8b.pdf (2018-03-22).
[71] ON Semiconductor (2014), "Power factor correction (PFC) Handbook " 2014-04, Rev.5, [Online]. Available: http://www.onsemi.com/pub/Collateral/HBD853-D.PDF (2018-03-07).
[72] Schwalbe, U. and Schert, M. "Which is the best PFC stage for a 1kW application? -Comparison of different PFC stage topologies under an identical design philosophy", Ilmenau University of Technology, slides. (2018-03-07).
[73] Infineon Technologies, "CrCM PFC Boost Converter Design", 2013-01, v.1, [Online] Available: http://www.digikey.ie/en/pdf/i/infineon-technologies/crcm-pfc-boost-converter-design (2018-03-07).
[74] Schmenger, J., Endres, S., Zeltner, S. and März, M. (2014), "A 22 kW Onboard Charger for Automotive Applications Based on a Modular Design " IEEE publishing. (2018-04-05).
[75] Agarwal, T. (2015). " Why is a Full Wave Bridge Rectifier Better Than a Full Wave Center Tap Rectifier? And Their Differences" [Online]. Available: https://www.elprocus.com/full-wave-bridge-rectifier-versus-center-tapped-full-wave-rectifier/1 (2018-04-12).
[76] Andersson, C. (2011), "Design of a 2.5kW DC/DC Fullbridge Converter". Master's Theses, Department of Energy and Environment, Chalmers uni-

versity of technology, Västergötland, Gothenburg, Sweden [Online]. Available: http://publications.lib.chalmers.se/records/fulltext/173958/173958.pdf (2018-02-12).

[77] Mouser Electronics, ”Half-Bridge DC/DC Converter”, [Online]. Available: https://www.mouser.se/applications/power-supply-topology-half/ (2018-02-12).

[78] Shodhganga, ”DC/DC converter”. [Electronic] Shodhganga publishing ”. Available: http://shodhganga.inflibnet.ac.in/bitstream/10603/134450/14/14_chapter205.pdf.

[79] Simons, R.E. (2017), ”Estimating Internal Air Cooling Temperature Reduction in a Closed Box Utilizing Thermoelectrically Enhanced Heat Rejection ” [Online]. Available:https://www.electronics-cooling.com/2017/11/estimating-internal-air-cooling-temperature-reduction-in-a-closed-box-utilizin (2018-01-29).

[80] Simons, R.E. (2005), ”Electonics cooling - Estimating Temperatures in an Air-cooled Closed Box Electronics Enclosure,” [Online]. Available:https://www.electronics-cooling.com/2005/02/estimating-temperatures-in-an-air-cooled-closed-box-electronics-enclosure/ (2018-01-29).

[81] Juniper networks (2017), ”MX10003 Cooling System Description ” [Online]. Available:https://www.juniper.net/documentation/en_US/release-independent/junos/topics/concept/mx10003-cooling-system-description.html (2018-01-29).

[82] XP Power (2012), ”Thinking inside the box: Getting heat out of sealed enclosures ” [Online]. Available: https://www.ecnmag.com/article/2012/12/thinking-inside-box-getting-heat-out-sealed-enclosures (2018-01-29).

[83] Rarbach, B. (2011), ”Media information Vehicle inlets and connectors type 2 for AC and DC charging ” [Electronic]. MENNEKES Elektrotechnik [Electronic]. Available: http://www.mennekes.it/uploads/media/MENNEKES_Media_information_-_Charging_couplers_Type_2_for_AC_and_DC_charging.pdf (2018-03-15).

[84] Gannon, M. (2016).” What is ampacity?” [Online]. Available: https://www.wireandcabletips.com/what-is-ampacity/ (2018-03-01).

[85] Zeca, ”Cable reel for electric car” [Online]. Available: http://www.zeca.it/en/cable-reel-for-electric-cars/199/ (2018-03-01).

[86] Höckenström, A. (2016). ” Volvo, Charging systems for electrified vehicles – AC, DC, Wireless/automatic ”. (2018-03-03).

[87] Kongsberg Automotive (2017), ”CMA OBC - Charger Efficiency DPR Fulfillment, Power out deration ” (2018-03-19).

[88] Supplier of CEVT (2017), ”Supplier data: transformer status in B-sample (Prototype sample) ” (2018-04-17).

[89] Ding, C. (2017), ”MDS Report - Substances of assmblies and materials ” (2018-03-12). DXC technology publiciation (2018-04-17).

[90] Goswami, A. (2017), " Thermal Management of On-board Chargers in E-Vehicles" [Online]. Available: https://www.electronics-cooling.com/2017/08/thermal-management-board-chargers-e-vehicles/# (2018-02-14).
[91] Padt, D., (2018) "Mennekes at sales Export - eMobility" [Mail] www.mennekes.de (2018-02-25).
[92] Mennekes, "Charging cable mode 2 with charging connector type 2 " [Online]. Available: http://www.mennekes.it/Graphics/XPic1/00036589_0.pdf (2018-04-17).
[93] Allen, J. (2013), "Understanding The IP67 Rating For Waterproof Cables And Connectors" [Online]. Available: http://sourcetech411.com/2013/04/understanding-the-ip67-rating-for-waterproof-cables-and-connectors (2018-02-19).
[94] Thasreef, H.R., Ramesh, P., Aleyas, M.V. (2015), "PSIM model and power loss calculation of full bridge DC-DC converter used for renewable energy applications" Vol.4, August 2015 [Electronic]. (2018-03-29).
[95] Garcia, N (2005), " Determining Inductor Power Losses" [Electronic]. Available:http://inductors.ru/pdf/doc486_inductorlosses.pdf (2018-05-04).
[96] MŁOT, M., Korkosz, M., Grodzki, P. and Łukaniszn, M. (2014), "Analysis of the proximity and skin effects on copper loss in a stator core " [Onine]. Available: https://www.degruyter.com/downloadpdf/j/aee.2014.63.issue-2/aee-2014-0017/aee-2014-0017.pdf (2018-04-27).
[97] Kiran Daware (2016), "Transformer - Losses And Efficiency" [Online]. Available: https://www.electricaleasy.com/2014/04/transformer-losses-and-efficiency.html (2018-04-25).
[98] Snelling, E.C. (1969) Soft Ferrities - Properties and applications. Published by J.W Arrowsmith Ltd. Mullards Research Laboratories.
[99] Circuit Globe (2017), " Types of Losses in a Transformer " [Onine]. Available:https://circuitglobe.com/types-of-losses-in-transformer.html#IronLosses (2018-04-25).
[100] Dekker, M. (2014), "Chapter 10 AC Inductor Design" [Electronic].Available: https://coefs.uncc.edu/mnoras/files/2013/03/Transformer-and-Inductor-Design-Handbook_Chapter_10.pdf (2018-04-25).
[101] Björklund, P.M. (2014), "Theoretical Design of a Single Phase 2kW Power Supply with 1.5kV DC Output ". Uppsala University [Online]. Available:http://www.diva-portal.org/smash/get/diva2:793976/FULLTEXT02 (2018-04-26).
[102] Nofziger, (2008), "Average and RMS Values of a Periodic Waveform" [Electronic]. Available: https://wp.optics.arizona.edu/mnofziger/wp-content/uploads/sites/31/2016/08/AVG-and-RMS-Values-of-Periodic-Waveforms-2012.pdf (2018-04-29).
[103] Ferroxcube, "Exploded view of a planar transformer" [Electronic]. Available: http://web.eecs.utk.edu/~dcostine/ECE482/Spring2017/components/magnetics/Ferrox20Cube20Design.pdf (2018-04-29).
[104] Reinert, J., Brockmeyer, A., Doncker, Rik W. A. A. De (2001), "Calculation of Losses in Ferro- and Ferrimagnetic Materials Based on the Modified Steinmetz Equation" [Electronic]. VOL. 37, NO. 4, July/August 2001, IEEE publishing.

Available: https://ieeexplore-ieee-org.proxy.lib.chalmers.se/stamp/stamp.jsp?tp=&arnumber=936396 (2018-04-29).
[105] Minges, M. L. (1989), " Electronic Materials Handbook: Packaging, vol. 1. " [Electronic]. ASM International publishing (2018-04-28).
[106] Rao, T., Rymaszewski, E.J., Klopfenstein, A.G., (1997), " Microelectronics Packaging Handbook: Semiconductor Packaging " (2018-04-28).
[107] Ivey, B. (2012), " Tracking microcontroller power consumption" [Online]. Available: https://electronicsnews.com.au/tracking-microcontroller-power-consumption/ (2018-04-28).
[108] Orenchak, G.G.(2004), " Estimating Temperature Rise of Transformers" [Online]. Available: http://www.powerelectronics.com/content/estimating-temperature-rise-transformers (2018-04-28).
[109] Texas Instruments Incorporated (2016), " LC Filter Design " [Online]. Available: http://www.ti.com/lit/an/slaa701a/slaa701a.pdf (2018-04-28).
[110] Ekemezie, P.N. (2007), "Design Of A Power Factor Correction AC-DC Converter" [Electronic]. IEEE publishing, March, 2006 (2018-03-17).
[111] Mouser Electronic (2003), "Low Core Loss, High Current Toroid Inductors " [Electronic]. Available:https://www.mouser.se/datasheet/2/54/2001l_series-776025.pdf (2018-03-27).
[112] STMicroelectronics (2016), "STF10N60DM2" [Electronic]. Available:https://www.mouser.se/datasheet/2/389/stf10n60dm2-974253.pdf (2018-03-27).
[113] Power Integrations (2015), "QH08TZ600, QH08BZ600" [Electronic]. Available:https://www.mouser.se/datasheet/2/328/qh08tz600_qh08bz600-257613.pdf (2018-03-27).
[114] KMG series. "Miniature aluminum electrolytic capacitors" [Electronic]. Available:http://www.farnell.com/datasheets/2343590.pdf?_ga=2.212890845.853855569.1524598025-1819357601.1524598025 (2018-03-27).
[115] Zhu, M. (2016), "1.5 kW Totem-pole PFC Using 650V USCi SiC Cascodes" [Electronic]. Available:http://unitedsic.com/wp-content/uploads/2017/06/Totem-Pole-PFC-v2-AppNote-2017-06-23.pdf (2018-03-29).
[116] Cree (2016), "C3D03060F Silicon Carbide Schottky Diode" [Electronic]. Available:https://www.mouser.se/datasheet/2/90/3d03060f-838535.pdf (2018-03-27).
[117] The calculator site, " Weight To Volume Converter" [Online]. Available:https://www.thecalculatorsite.com/conversions/weighttovolume.php (2018-04-28).
[118] STMicroelectronic (2015), "STPSC406" [Electronic]. Available:https://eu.mouser.com/datasheet/2/389/stpsc406-956786.pdf (2018-04-02).
[119] STMicroelectronic (2009), "STPSC606" [Electronic]. Available:https://www.mouser.se/datasheet/2/389/stpsc606-956699.pdf (2018-04-02).
[120] Infineon Technologies (2009), "IDH08SG60C" [Electronic]. Available:https://www.mouser.se/datasheet/2/196/Infineon-IDH08SG60C-DS-v02_04-en-1131118.pdf (2018-04-02).
[121] Mouser Electronics (2009), "High Current Toroid Inductors " [Electronic]. Available:https://www.mouser.se/datasheet/2/54/300_series-776044.pdf (2018-04-02).

[122] Mouser Electronics (2011), ”High Temperature, High Current Toroid Inductors ” [Electronic]. Available:https://www.mouser.se/datasheet/2/54/300ht_series-776374.pdf (2018-04-02).
[123] STMicroelectronic (2011), ”STF11N60DM2” [Electronic]. Available:https://www.mouser.se/datasheet/2/389/stf11n60dm2-974280.pdf (2018-04-02).
[124] Fairchild Semiconductor (2011), ”FCPF13N60N/FCPF13N60NT” [Electronic]. Available:https://www.fairchildsemi.com/datasheets/FC/FCPF13N60NT.pdf (2018-04-02).
[125] Infineon Technologies (2012), ”IDH10SG60C” [Electronic]. Available:https://www.mouser.se/datasheet/2/196/IDH10SG60C_rev2.4-78863.pdf (2018-04-02).
[126] Power Intregrations (2015), ”QH12TZ600, QH12BZ600” [Electronic]. Available:https://www.mouser.se/datasheet/2/328/qh12tz600_qh12bz600-257615.pdf (2018-04-02).
[127] NICHICON CORPORATION, ”QALUMINUM ELECTROLYTIC CAPACITORS” [Electronic]. Available:https://www.mouser.se/datasheet/2/293/e-lls-876281.pdf (2018-04-02).
[128] Panasonic (2016), ”Aluminum Electrolytic Capacitors (Radial Lead Type)” [Electronic]. Available:https://www.mouser.se/datasheet/2/315/ABA0000C1026-947572.pdf (2018-04-02).
[129] Mouser Electronics (2009), ”High Temperature, High Current Toroid Inductors” [Electronic]. Available:https://www.mouser.se/datasheet/2/54/200ht_series-776003.pdf (2018-04-02).
[130] Mouser Electronics (2009), ”High Current Toroid Inductors” [Electronic]. Available:https://www.mouser.se/datasheet/2/54/300_series-776044.pdf (2018-04-02).
[131] Coilcraft (2006), ”Power Choke – L0451-AL” [Electronic]. Available:https://www.mouser.se/datasheet/2/597/l0451-463435.pdf (2018-04-02).
[132] NICHICON CORPORATION (2011), ”ALUMINUM ELECTROLYTIC CAPACITORS” [Electronic]. Available:https://www.mouser.se/datasheet/2/293/e-uas-883801.pdf (2018-04-02).
[133] NICHICON CORPORATION (2011), ”ALUMINUM ELECTROLYTIC CAPACITORS” [Electronic]. Available:https://www.mouser.se/datasheet/2/293/e-urz-879998.pdf (2018-04-02).
[134] Panasonic (2016), ”Aluminum Electrolytic Capacitors (Radial Lead Type)” [Electronic]. Available:https://eu.mouser.com/datasheet/2/315/ABA0000C1026-947572.pdf (2018-04-02).
[135] Würth Elektronik (2006), ”WE-HCI SMD Flat Wire High Current Inductor” [Electronic]. Available:https://eu.mouser.com/datasheet/2/445/7443551181-539491.pdf (2018-04-05).
[136] Bourns (2003), ”SRR1208 Series - Shielded High Power Inductors” [Electronic]. Available:https://eu.mouser.com/datasheet/2/54/rr1208-777886.pdf (2018-04-05).
[137] Borns (2003), ”SRU8045A Series - Shielded Power Inductors” [Electronic]. Available:https://eu.mouser.com/datasheet/2/54/ru8045a-964794.pdf (2018-04-05).

[138] TDK Corporation (2016), ”Film Capacitors - EMI Suppression Capacitors (MKP)” [Electronic]. Available:https://eu.mouser.com/datasheet/2/400/X2_B32922_926_H_J-746197.pdf (2018-04-05).

[139] TDK Corporation (2016), ”Film Capacitors - EMI Suppression Capacitors (MKP)” [Electronic]. Available:https://eu.mouser.com/datasheet/2/400/X2_B32922_926_H_J-746197.pdf (2018-04-05).

[140] Bourns (2003), ”SRU8045A Series - Shielded Power Inductors” [Electronic]. Available:https://eu.mouser.com/datasheet/2/54/ru8045a-964794.pdf (2018-04-05).

[141] Sumida, ”SType: CDRH10D48/AA” [Electronic]. Available:https://eu.mouser.com/datasheet/2/390/CDRH10D48A-523404.pdf (2018-04-05).

[142] Bourns (2003), ”SRP5030TA Series - Shielded Power Inductors” [Electronic]. Available:https://eu.mouser.com/datasheet/2/54/rp5030ta-765095.pdf (2018-04-05).

[143] Bourns (2003), ”R6004KNX” [Electronic]. Available:https://eu.mouser.com/datasheet/2/348/r6004knx-1139083.pdf (2018-04-05).

[144] Bourns (2003), ”MOSFET 600V Cool MOSFET P7 Power Transistor” [Electronic]. Available:https://www.mouser.se/datasheet/2/196/Infineon-IPAW60R600P7S-DS-v02_00-EN-1131048.pdf (2018-04-05).

[145] STMicroelectronic (2016), ”STF10N60DM2” [Electronic]. Available:https://www.mouser.se/datasheet/2/389/stf10n60dm2-974253.pdf (2018-04-05).

[146] STMicroelectronic (2012), ”IDH04SG60C” [Electronic]. Available:https://www.mouser.se/datasheet/2/196/IDH04SG60C_rev2.4%20-93545.pdf (2018-04-05).

[147] STMicroelectronic (2012), ”IDH05SG60C” [Electronic]. Available:https://www.mouser.se/datasheet/2/196/IDH05SG60C_rev2.4-93195.pdf (2018-04-05).

[148] STMicroelectronic (2012), ”IDH05SG60C” [Electronic]. Available:https://www.mouser.se/datasheet/2/196/IDH05SG60C_rev2.4-93195.pdf (2018-04-05).

[149] NICHICON CORPORATION (2011), ”Aluminum electrolytic capacitors” [Electronic]. Available:https://www.mouser.se/datasheet/2/293/e-uvy-1219509.pdf (2018-04-05).

[150] Panasonic (2016), ”Aluminum Electrolytic Capacitors (Radial Lead Type)” [Electronic]. Available:https://eu.mouser.com/datasheet/2/315/ABA0000C1218-1131230.pdf (2018-04-07).

[151] Würth Elektronik (2014), ”WE-RFI Ferrite SMD Inductor” [Electronic]. Available:https://www.mouser.se/datasheet/2/445/744762327A-466031.pdf (2018-04-07).

[152] Sun, B (2017), ” Control challenges in a totem-pole PFC” [Electronic]. Texas Instruments Incorporated publishing. Available:http://www.ti.com/lit/an/slyt718/slyt718.pdf (2018-05-01).

[153] Texas Instruments Incorporated (2018), ” High-Efficiency, 1.6-kW High-Density GaN-Based 1-MHz CrM Totem-Pole PFC Converter Reference Design” [Electronic]. Available:http://www.ti.com/lit/ug/tidudt3/tidudt3.pdf (2018-05-01).

[154] Graovac, D., Pürschel, M. and Kiep, A (2006), " MOSFET Power Losses Calculation Using the DataSheet Parameters " [Electronic].Available:http://application-notes.digchip.com/070/70-41484.pdf (2018-05-04).

[155] Wu, W. (2017), " 1.5kW digital totem pole PFC design for air-conditioner and performance comparison using IGBT and GaN " Nuremberg, Germany [Electronic]. (2018-05-04).

[156] Power Electronics (2017) "Power Electronics - MOSFET Power Losses " [YouTube]. Available:https://www.youtube.com/watch?v=KSOHwVoxpzg. (2018-05-18).

[157] Bodo's Power Systems (2015), " Advantages of the 1200 V SiC Schottky Diode with MPS Design " [Electronic].Available:https://www.infineon.com/dgdl/Infineon-Article_Advantages_of_the_1200V_SiC_Schottky_Diode_with_MPS_Design-ART-v01_00-EN.pdf?fileId=5546d46250cc1fdf0151674981861d76 (2018-05-04).

[158] Ferroxcube (2008), " ETD49/25/16 - ETD cores and accessories " [Electronic]. Available:http://c1170156.r56.cf3.rackcdn.com/UK_PMA_ETD49_25_16-3F3_DS.pdf (2018-05-04).

[159] ABL Components, " Heatsink, 0.6°C/W, 150 x 100 x 15mm, PCB Mount " [Online]. Available: https://uk.rs-online.com/web/p/heatsinks/9033080/ (2018-05-20).

[160] ABL Components, " Heatsink, 0.23°C/W, 200 x 200 x 15mm, PCB Mount " [Online]. Available: https://uk.rs-online.com/web/p/heatsinks/9033090/ (2018-05-20).

[161] Shield solutions, " Thermally Conductive, Electrically Insulating Materials " [Online]. Available: https://rfi-shielding.com/product/thermally-conductive-interface/ (2018-05-20).

[162] ABL Components, " 109AB" [Electronic]. Available:https://docs-emea.rs-online.com/webdocs/1473/0900766b81473572.pdf (2018-05-01).

[163] Heatsinkcalculator, "The importance of radiation in heat sink design" [Online]. Available: http://www.heatsinkcalculator.com/blog/the-importance-of-radiation-in-heat-sink-design/ (2018-05-20).

[164] DigiKey Electronics, " Delta Electronics ASB0312LA-CF00" [Online]. Available: https://www.digikey.com/product-detail/en/delta-electronics/ASB0312LA-CF00/603-1728-ND/3444174 (2018-05-20).

[165] Elevatorshop, " Eurolift, printed circuit board LONPBD2.Q for landing push MX" [Online]. Available: http://www.elevatorshop.de/en/eurolift-printed-circuit-board-lonpbd2.q-landing-push-mx.html (2018-05-30).

A

Appendix - Circuit diagrams

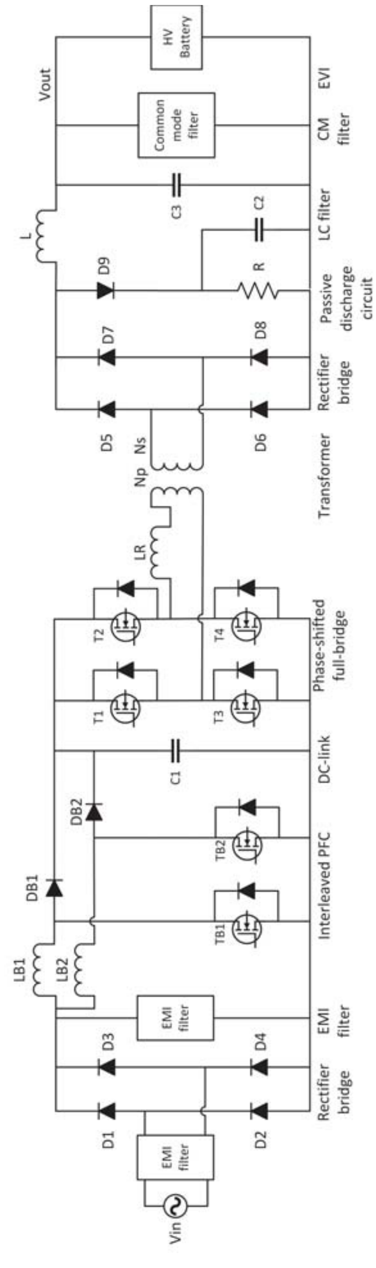

Figure A.1: Circuit diagram of the OBC Geely 8888003014 G BQ8AA from Geely Group.

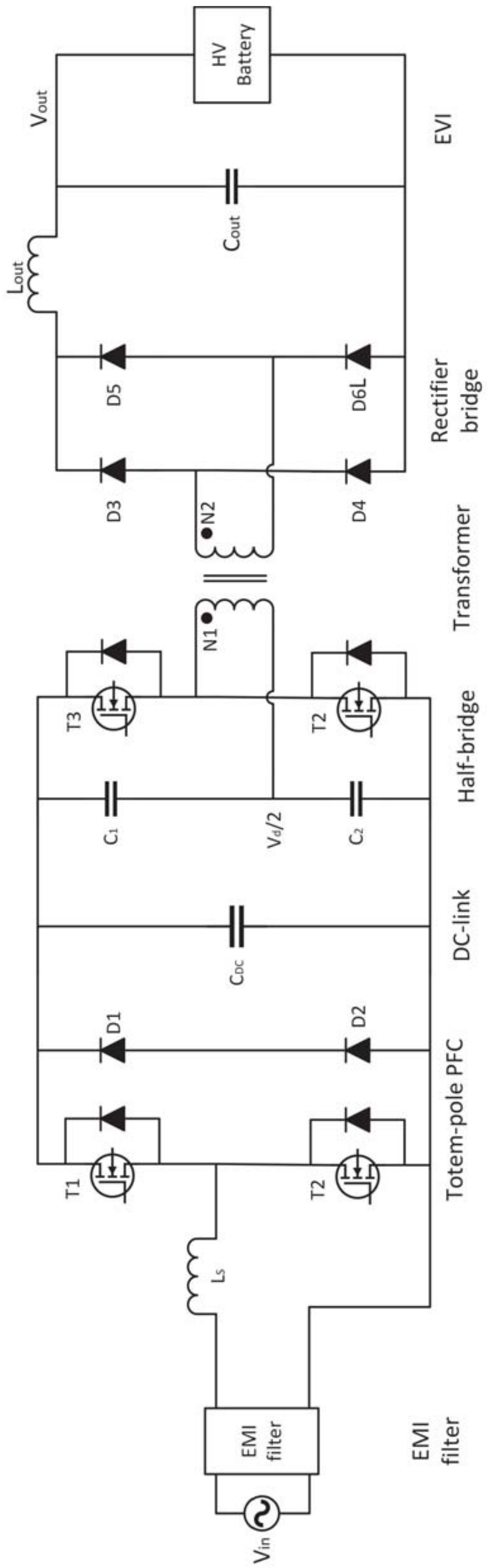

Figure A.2: Circuit diagram of the proposed off-board charger.

B

Appendix - Components, operation mode, topologies

Table B.1: OBC - list of the power electronic components.

Component	Model nr.	Amount	Temperature limit	Value
Capacitor	N/A	3	N/A	47 μF
Capacitor	N/A	3	N/A	33 μF
Capacitor	RIFE PME 271 Y	6	-40 to 100 °C	47 μF
Capacitor	B145	2	105 °C	100 μF
Capacitor	ENSH5M	4	105 °C	270 μF
Capacitor	B32924	3	110 °C, 125 °C	3.3 μF
Diode	apt10scd120b	2	-55 to 150 °C	N/A
Diode	40EPS08	4	-40 to 150 °C	N/A
Diode	N/A	4	150 °C	N/A
Fuses	bell30	2	N/A	N/A
MOSFET	FCH104N60F	2	-55 to 150 °C	N/A
Inductor	N/A	2	N/A	7,2 μH
Inductor	N/A	2	N/A	3.65; 3.68 mH
Inductor	N/A	1	N/A	188 μH
Inductor	N/A	2	N/A	388 μH
Thyristor	30TPS08	4	-40 to 125 °C	N/A
Temperature sensor	NTC N/A	8	N/A	N/A
Transformer	N/A	1	N/A	1.5 mH
Transformer	N/A	1	N/A	N/A
Varistor	N/A	2	N/A	N/A

Table B.2: Charging cable - list of the power electronic components.

Component	Model nr.	Amount	Temperature limit	Value
Capacitor	B41896	2	-55 to 125	680 μF
Capacitor	N/A	2	N/A	47 μF
Capacitor	N/A	2	-40 to 125 °C	N/A
EEPROM	25LC160	1	N/A	N/A
Fixed inductors	N/A	3	N/A	N/A
Fuse	T2AL	3	N/A	250V
IC chip	M430F247T	3	-40 to 105 °C	N/A
Voltage regulators	9L12A	1	N/A	N/A
Capacitor	N/A	2	105 °C	18 μF
Optocoupler	TCLT1003	1	-55 to 125 °C	N/A
Optocoupler	SFH6286-3V	2	N/A	N/A
PCB	B82720-S2301-N40	1	N/A	0.3 A, 250 V
Realy/switch	PCFN-112H2MG	3	N/A	N/A
Relay	G6DS-1A-H DC5	2	N/A	N/A
Inductor	N/A	2	N/A	N/A
Transformer	N/A	1	N/A	N/A
Varistor	N/A	8	N/A	N/A
Transformer	N/A	1	N/A	1,5 mH
Transformer	N/A	1	N/A	N/A
Varistor	4032K275 1610	2	-40 to 125 °C	N/A

Table B.3: Comparison between switching devices MOSFET and IGBT [41], [42], [43].

Switch device	MOSFET	IGBT
General info:	Voltage range of 250-1000 V if fsw is in the range 200-1000 kHz.	Voltage range of 250-1000 V, if fsw is 1-20kHz.
	<500 W output power.	>5 kW output power.
	Long duty cycle.	Low duty cycle.
	ZVS below 1000 W.	Operation at high junction temperature (>100 °C)
	Wide line or load variations.	Narrow or small line or load variations.
	Majority carrier device.	Minority carrier device.
Advantages:	Lower on-state losses, because of the transistors on-state resistance has 'no limit'.	Turn on and off rapidly.
	Operates at high frequencies, due to absence of minority carrier transports.	Generates large power pulses. Its pulse repetition frequency gets into the ultrasonic range.
	Perform fast switching applications with little turn-off losses.	Improved production techniques, hence lower cost.
	Higher commutation speed (at low voltages).	Low on-state losses and switching losses.
	Higher efficiency (at low voltages).	Higher voltage and current handling capability.
	Lower thermal impedance, hence better power dissipation.	Lower on-state voltage drops due to conductivity modulation.
	Elimination of the current tail.	
	Simple drive.	
	At low power, low losses.	
Disadvantages:	Transient time of electrons across the drift region.	Reduction in on-state voltage can cost the IGBT to experience slower switching speed at turn-off.
	The time required to charge/discharge the input gate and 'Miller' capacitances.	Large current tail, at turn-off until the recombination is complete.
	High conduction losses when operating at 13 A.	No body drain diode.
		Negative temperature coefficient, could lead to thermal runaways. Thus making it difficult efficiently achieve paralleling of devices.

Table B.4: Comparison of different operation modes such as CCM, DCM and CrM [71],[72],[73].

Operation mode	**CCM**	**CrM**	**DCM**
Switching frequency	Fixed	Variable	Fixed
Component stress: Switch	Average	High	High
Component stress: Diode	High	Low	Low
Component stress: Inductor	*Low losses, due to low current ripple. *Low EMI	*High losses, due to large current ripple. *High EMI. *Lower L value, which results in lower energy	High losses, due to large current ripple. *Lower L value, which results in lower energy.
Advantages	*Functioning at fixed frequency, which makes it easier to filter. *Reduced conduction losses. *Low di/dt, easier to remove EMI. *Cost better at higher power levels.	*Simple. *Low cost. *Small inductor. *Low energy. *Low cost for lower power levels. *Improving power density	*Fixed frequency. *Stabillity. *Small inductor. *Low energy. *High efficiency
Disadvantages	*Large inductor value. *High energy.	*Stage synchronisation not possible, due to variable frequency. *High RMS current	*High peak current levels, which leads to higher losses.

Table B.5: Comparison of different PFC topologies [62],[63][64],[65].

Topology (PFC)	**Classic Boost**	**Dual Boost Bridgeless**	**Totem-pole Bridgeless**	**Interleaved Boost**
Cost	Low	Medium	High	Medium
Power rating	1000 W	2000 W	1000 W	3000 W
Number of components	7	8	5	10
Advantages	*Low cost. *Few components. *Simple control. *Reduced conduction losses. *Smaller EMI-filter.	*High efficiency.	*Good efficiency. *Few components. *Inherent zero switching. *Reduced conduction losses. *Low EMI. *High efficiency.	*Good thermal design. *Small output current ripple. *Reduced EMI-filter volume. *Reduced conduction losses.
Disadvantages	*Low efficiency *Generates high-frequency noise *Increases switching losses	*Low utilization rate *Higher cost *high EMI/noise *high capacitor ripple	*With high common mode interference *High cost *Only possible with GaN or SiC	*Higher cost *Complex *High number of components

Table B.6: Total capacitance at the DC-link for both Boost-and Totem-pole PFC.

Current rate	**Boost PFC**	**Totem-pole PFC**
4 A	C_{bank} =180μF	C_{bank}=150μF
6 A	C_{bank}=270μF	C_{bank}=190μF
8 A	C_{bank}=323μF	C_{bank}=323μF

C

Appendix - LTspice simulation

Table C.1: Output result from LTspice simulation with Boost PFC.

	LTspice simulation		
Topology	4A	6A	8A
Boost PFC	V_{out}=400.58 V I_{out}=2.44 A	V_{out}= 364.90 V I_{out}=3.23 A	V_{out}=332.85 V I_{out}=3.83 A
Full-bridge	V_{out}=380.95 V I_{out}=2.563 A	V_{out}=349.78 V I_{out}=2.854 A	V_{out}=323.26 V I_{out}= 2.8507 A
Half-bridge	V_{out}=380.4 V I_{out}=2.577 A	V_{out}=347.71 V I_{out}=2.837 A	V_{out}=316.51 V I_{out}=2.799 A

Table C.2: Output result from LTspice simulation with Totem-pole PFC.

	LTspice simulation		
Topology	4A	6A	8A
Totem PFC	V_{out}=289.54 V I_{out}=1.7655 A	V_{out}=281.15 V I_{out}=2.515 A	V_{out}=288.52 V I_{out}=3.324 A
Full-bridge	V_{out} =288.08 V I_{out}=1.0198 A	V_{out}=275.08 V I_{out}=1.347 A	V_{out}=279.57 V I_{out}= 1.857 A
Half-bridge	V_{out}=282.3 V I_{out}=1.00 A	V_{out}=272.17 V I_{out}=1.3326 A	V_{out}=277.88 V I_{out}=1.8458 A

D

Appendix - Power losses

Components utilized for the calculations

Table D.1: Component selection for the different devices in Totem-pole, 4 A.

Device	**Number**
AC/DC + Totem	
Diode-bridge	STPSC406
MOSFET	STF10N60DM2
Inductor	2200LL-331-H-RC
DC-link	Aluminum electrolytic capacitor
DC/DC + Totem	
Transformer	EDA49/25/16
MOSFET	STF10N60DM2
Diode-bridge	C3D03060F

Comparison between two transformer cores

To make a comparison, another transformer core (B) called ETD34/17/11-3F3 with a core area of 97.1mm^2 was selected. This transformer includes the Litz wire CLI 200/30. By using the same mathematical equations steps, as for core (A), gave the results presented in Table D.2. The transformer core A and core B described in this table has an assumed ratio of 1:1.

From the comparison Table D.2 it can be seen that with the larger core area of 211mm^2 there will be less total losses and therefore a higher efficiency rate compared to the 97.1 mm^2 core area size.

Flux density comparison

The different power loss and efficiency at different input current 4 A, 6 A, 8 A from the AC/DC to DC/DC converter, is shown in Table D.3. This was calculated for B=0.15 T.

From Table D.3, it is seen that core A has lower losses and a stable efficiency independent on an increase in current from 4 A to 8 A. Core B are showing higher losses and decrease rapidly in efficiency when the current increases from 4 A to 8 A.

The different power loss and efficiency at different input current 4 A, 6 A, 8 A from the AC/DC to DC/DC converter, is presented in Table D.4. This was calculated for B=0.1 T.

From Table D.4, it is observed that core A has higher losses and a decrease in efficiency depending on an increase in current from 4 A to 8 A. Core B are showing slightly lower losses than core A and a decrease in efficiency when the current increases from 4 A to 8 A.

Table D.2: Comparison between the two core of transformers.

Parameters	**Transformer core A**	**Transformer core B**
A_{core}	211 mm^2	97.1 mm^2
Core diameter	16.39 mm	10.8 mm
N_1, N_2	14 turns	45 turns
B_m	0.15 T	0.15 T
Area Litz-wire datasheet	0.94 mm^2	0.24 mm^2
$A_{cu,max}$	1.997 mm^2	0.4689 mm^2
A_w	186.43 mm^2	93.775 mm^2
Volume	19.7 cm^3	6.39 cm^3
R_{wire}	0.0257 Ω	0.1425 Ω
R_{dc}	3.7075 Ω	29.01 Ω
P_M	1047 mW/cm^3	1047 mW/cm^3
P_w	6.942 W	54.315
P_{core}	3.999 W	1.09796 W
P_{loss}	10.941 W	55.413 W
η	98.8 %	94.2 %

Table D.3: Power loss and efficiency comparison, B=0.15 T.

Current	**Ptot_Core A**	**Ptot_Core B**
4A	10.941 W	55.413 W
6A	18.462 W	124.256 W
8A	28.733 W	212.494 W
	η Core A	η Core B
4A	98.8 %	94.2 %
6A	98.6 %	91.3 %
8A	98.3 %	88.9 %

Table D.4: Power loss and efficiency comparison, B=0.1 T.

Current	Ptot_Core A	Ptot_Core B
4A	17.15 W	12.61 W
6A	34.12 W	25.85 W
8A	57.3 W	43.90 W
	η Core A	η Core B
4A	98.1 %	98.6 %
6A	97.4 %	98.1 %
8A	96.7 %	97.5 %

Parameters for components

Table D.5: Totem + DC/DC half-bridge power losses.

Totem + DC/DC Half-bridge				
Parameters	**Units**	**4A**	**6A**	**8A**
Transistor:				
D		0.5	0.5	0.5
Vdc	[V]	200	200	200
time	[ns]	80	69	55.5
Pcond	[W]	2.778	4.754	10.609
Psw	[W]	3.809	4.754	4.966
Ploss	**[W]**	**6.588**	**11.875**	**15.575**
Output diode-bridge:				
Vdrop	[V]	1.8	2.8	2.8
Idc	[A]	2.964	4.424	5.716
Pcond	[W]	10.672	24.773	32.009
Ploss	**[W]**	**10.672**	**24.773**	**32.009**
Transformer:				
Ploss	**[W]**	**11.447**	**20.584**	**31.688**

Table D.6: Totem + DC/DC Full-bridge power losses.

Totem + DC/DC Full-bridge				
Parameters	**Units**	**4A**	**6A**	**8A**
Transistor:				
D		0.5	0.5	0.5
Vdc	[V]	400	400	400
time	[ns]	80	69.0	55.5
Pcond	[W]	2.778	7.121	10.609
Psw	[W]	7.619	9.508	9.932
Ploss	[W]	10.398	16.629	20.541
2*Ploss	**[W]**	**20.8**	**33.2**	**41.08**
Output diode-bridge:				
Vdrop	[V]	1.8	2.8	2.8
Idc	[A]	3.574	4.6896	5.9957
Pcond	[W]	12.866	26.262	33.576
Ploss	**[W]**	**12.866**	**26.262**	**33.576**
Transformer:				
Ploss	**[W]**	**19.589**	**30.842**	**47.875**

All power losses for capacitors and inductors are lower than 0.2 W, and therefore are not presented in the tables above.

Heat characteristics for different components

Table D.7: Device characteristics, 4 A, Totem + DC/DC.

Device	**Rth,jc**	**Tj,max**
AC/DC + Totem		
Diode-bridge	4.5	175
MOSFET	5	150
DC/DC		
Transformer	-	155
MOSFET	5	150
Diode-bridge	12	175

E

Appendix - Heatsink simulation

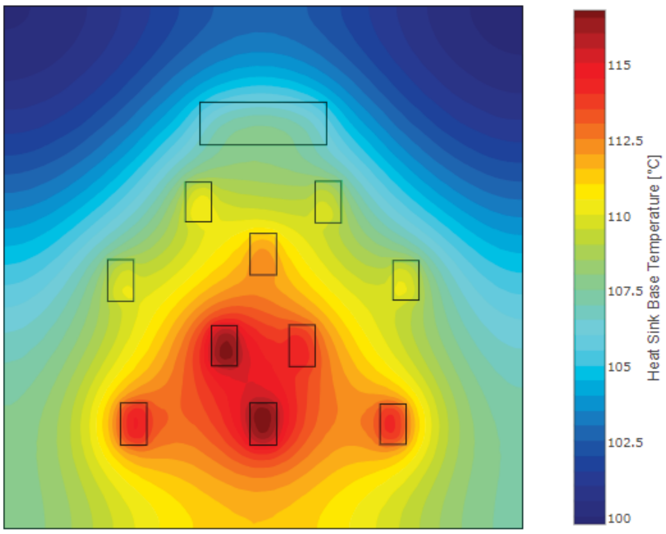

Figure E.1: Simulation of natural cooling on a larger heatsink size.

Table E.1: Temperature of the components for natural cooling with a larger heatsink size.

Power source	T_{avg} [°C]	T_{max} [°C]
Transformer	201	202
Totem MOSFET 1	182	182
Totem MOSFET 2	180	180
Totem Diode 1	177	177
Totem Diode 2	174	175
Half-bridge MOSFET 1	137	138
Half-bridge MOSFET 2	137	137
Half-bridge Diode 1	179	179
Half-bridge Diode 2	174	175
Half-bridge Diode 3	183	184
Half-bridge Diode 4	178	179